NASA Technical Memorandum 83698

Morphological Changes of Gamma Prime Precipitates in Nickel-Base Superalloy Single Crystals

Rebecca A. MacKay
Lewis Research Center
Cleveland, Ohio

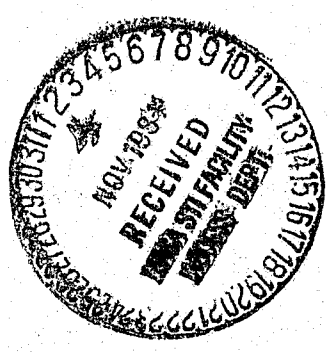

July 1984

NASA

ACKNOWLEDGMENTS

The author wishes to express her appreciation to:

The National Aeronautics and Space Administration for funding this work in part under NASA grant NSG-3246;

Professor L. J. Ebert for his contributions as thesis advisor;

Dr. C. S. Kortovich of TRW, Inc., for providing the single crystal material;

Dr. M. V. Nathal of the Lewis Research Center and Dr. D. D. Pearson of the United Technologies Research Center for many valuable discussions throughout the course of the work; and

Dr. H. R. Gray of the Lewis Research Center for his continued support and encouragement.

TABLE OF CONTENTS

	Page
INTRODUCTION	1
Strengthening Mechanisms	2
γ' Precipitate Morphology	6
Precipitate Coarsening	9
Theory	9
Experimental Observations	10
Effect of Volume Fraction	12
Influence of Misfit	14
Loss of Coherency	16
Effect of Stress on γ' Coarsening	21
Influence of Misfit: Summary	28
Statement of Purpose	30
MATERIAL AND EXPERIMENTAL PROCEDURES	32
Material	32
Mechanical Testing	34
Zero-Stress Aging Treatments	35
Specimen Preparation	35
Line Intercept Technique	37
Laue Back-Reflection X-Ray Technique	38
Misfit Measurement Procedure	39
Phase Extraction	40
RESULTS	42
Microstructure of Single Crystals	42
In situ Lattice Mismatch	47
High Temperature X-Ray Diffraction	48
Creep Properties	53
γ' Shape Changes During Creep	57

Page

Quantitative Analysis..... 63

Tensile Properties..... 72

Zero-Stress Aging..... 74

Effect of Initial Microstructure..... 77

Third Phase Precipitation..... 85
Identification..... 85
Microstructural Effects..... 86
Lower Mo-Containing Alloy..... 88

DISCUSSION..... 90

In situ Lattice Mismatch..... 90

High Temperature X-Ray Diffraction..... 93

Creep Properties..... 96

Morphological Changes of γ' During Creep..... 98

Tensile Behavior..... 106

Zero-Stress Aging Behavior..... 109

Initial Microstructural Effects..... 110

Third Phase Precipitation..... 115

CONCLUSIONS..... 118

REFERENCES..... 121

TABLES..... 133

FIGURES..... 142

INTRODUCTION

Nickel-base superalloys comprise a broad range of compositions which are utilized in a number of applications, including aircraft gas turbine engines. These commercial alloys frequently are complex multicomponent systems consisting of as many as a dozen elements. A considerable amount of research has been directed toward developing turbine blade materials capable of operating at increasingly higher temperatures, which would improve the performance and efficiency of the turbine engine. Continued improvements in the strength and metal temperature capability of turbine blade materials have been made possible in part by unidirectional solidification. This technique produces a columnar grain structure oriented such that its strong direction is parallel to the major stress axis of the blade. This columnar grain structure reduces the weakening influence of transverse grain boundaries. More recently, single crystal superalloys have been identified as an attractive approach for increasing allowable gas turbine blade temperatures by completely eliminating grain boundaries.

Nickel-base superalloys obtain much of their superior high temperature strength from the precipitation of γ'. The γ' phase is an intermetallic compound which has an ordered face-centered

cubic (FCC) structure ($L1_2$-type) based on Ni_3Al. The γ' phase precipitates coherently in the γ matrix, a nickel-rich FCC solid solution. In addition, other phases can precipitate in nickel-base superalloys. For example, various types of carbides are frequently present in carbon-containing alloys. These common classes of carbides are designated as MC, $M_{23}C_6$, and M_6C, where M represents the various carbide-forming elements, such as chromium (Cr), titanium (Ti), tantalum (Ta), molybdenum (Mo), and tungsten (W). In addition, high levels of niobium (Nb), Ta, Ti (1-3), and Mo (4-7) can result in the formation of a body-centered tetragonal (BCT) phase, γ'', which has a DO_{22}-type structure. Furthermore, a supersaturation of elements in the γ matrix can cause the formation of minor phases, such as σ, μ, δ, or Laves. These latter topologically close packed phases can be detrimental to high temperature properties, although this depends on the amount and the morphology of the third phase (3, 8).

Strengthening Mechanisms

The strength of nickel-base superalloys is largely dependent upon a number of factors which can be controlled to some degree by alloy composition and heat treatment. This section will serve as a brief review of the strengthening mechanisms of the γ matrix, as well as the ways in which the strength of a two phase γ-γ' alloy can be affected. In particular, strengthening will be related to solid solution hardening of γ and γ', anti-phase boundary (APB)

and fault hardening, diffusivity in γ and γ', γ-γ' modulus mismatch, coherency strains, and γ' volume fraction and particle size.

Most of the alloying elements in nickel-base superalloys partition, or segregate, to some extent between both the matrix and the precipitate (9-11). As a result, both phases are highly alloyed. Elements which can impart effective solid solution hardening to γ include Al, W, Mo, and Cr (1). Solid solution hardening of γ is related in part to the difference in atomic diameter between the solute atoms and Ni (12, 13). An additional strengthening effect may result from the lowering of stacking fault energy (1), which would make cross slip more difficult in γ.

It has also been proposed that modulus differences between the solute additions and the Ni matrix may increase solid solution hardening because of the difficulty in forcing a dislocation through hard and soft regions in the matrix (14). Furthermore, in concentrated solid solutions, the alloying elements are more likely to cluster and exhibit short-range ordering, which would cause an increase in the flow stress of the alloy (14). It has been suggested that short-range ordering exists in nickel-base alloys having a high Cr content (15), as well as in concentrated Ni-Mo alloys (16, 17). In the range of high temperature creep, which is above 0.6 of the melting point, T_m, elements such as Mo and W strengthen γ by limiting diffusion; these slow diffusing refractory elements also limit the diffusion of other elements (1, 11).

Several of the same basic factors contribute to hardening of the γ' phase. For example, solid solution hardening of γ' is enhanced by Ti, Nb, and Ta at elevated temperatures (1). These refractory elements should help to retard creep because of their slow diffusive nature. In a two-phase γ-γ' alloy, one of the major factors believed to contribute to strengthening is APB energy (14, 18). This energy is associated with the boundary (APB) which is created across the slip plane by a leading dislocation as it shears through the ordered precipitate; neighboring atoms become out of phase with their equilibrium sequence until a trailing dislocation restores the proper arrangement. This APB energy may serve to impede the movement of dislocations. Although there are few data available, APB energy does appear to be markedly affected by alloy content (14, 19, 20). In addition, it has been proposed that γ-γ' modulus mismatch should contribute to alloy strengthening (21). However, it is difficult to estimate the overall effect of modulus mismatch in superalloys, because of the lack of modulus data on alloyed γ and γ'.

Coherency strains have been recognized as an important strengthening mechanism in superalloys under certain conditions (1, 14). Early studies on nickel-base alloys found that significant increases in hardness and stress rupture properties were correlated to the disregistry between the γ and γ' lattices and the resultant coherency strains (22, 23). A subsequent investigation (24) was conducted to isolate the importance of coherency strains

and their effects on aged hardness and tensile properties. Ternary additions to Ni-Al alloys provided a range of γ-γ' mismatch, while the effects of APB energy and solid solution hardening of γ' were monitored simultaneously. It was found that age hardening could be enhanced by high coherency strains. However, it was pointed out that coherency strains may provide additional strengthening under conditions of non-diffusional creep (< 0.6 T_m), whereas low coherency strains would be desired at higher temperatures, in order to minimize γ-γ' surface energy and maximize phase stability (24).

In addition, the effectiveness of γ' strengthening is dependent not only on the volume percent of the precipitate, but on its size and distribution as well. For example, an increase in the γ' volume fraction from 14 to 60 pct. has been shown to improve the creep strength by as much as a factor of four in commercial superalloys (1). A maximum in creep resistance has been observed to occur at approximately 60 volume pct. in Ni-Cr-Al alloys (25). It is also well established that the interparticle spacing should be small (26) in order to achieve effective strengthening; to attain a fine spacing, the γ' particle size must be small. Improved tensile and creep properties were obtained in directionally solidified Mar-M200 when solution treatments dissolved the coarse γ' and γ-γ' eutectic constituents and produced a fine, uniform dispersion of γ' (27, 28). Additional quantitative data on a similar alloy demonstrated that the increase in volume percent of fine γ'

from 30 to 45 pct., which was produced by raising the solution temperature, resulted in a three-fold increase in creep life (29). The attainment of long creep life is related to the ability to develop a uniform dispersion of fine γ', which maximizes the amount of γ-γ' interfacial area (25). Such property improvements are consistent with increased particle-dislocation interactions which might be expected to occur as the volume fraction of fine γ' is increased and the interparticle spacing is decreased (29).

A fine dispersion of γ' has been identified as an important strengthening feature in superalloys. However, the γ' morphology produced by solidification and subsequent heat treatment can change under various conditions during service. The remainder of this chapter will attempt to describe how the γ' precipitate morphology is related to misfit, how the precipitate can change during aging as well as under an applied stress at elevated temperatures, and how such morphological changes can influence properties.

γ' Precipitate Morphology

Studies of a number of alloy systems have shown that the γ' precipitate can assume different morphologies. Early investigations related the observed morphologies to the mismatch in lattice parameters between the γ and γ' phases (30). The lattice mismatch results in elastic coherency strains. The magnitude of these strains is determined by the unconstrained γ-γ' lattice mismatch,

δ, which is given by (31, 32):

$$\delta = \frac{(a_{\gamma'} - a_{\gamma})}{(a_{\gamma'} + a_{\gamma})/2} \qquad [1]$$

where $a_{\gamma'}$ and a_{γ} are the lattice parameters of the γ' and γ phases, respectively. If the lattice parameters are measured in situ, the unconstrained mismatch can only be determined after allowing coherency loss to occur. In this case, the lattice parameters of each phase remain independent of each other. Frequently, experimental determinations of δ are difficult, and the constrained mismatch, ε, is measured in situ for fully coherent precipitates. In an alloy with coherent precipitates, the lattices of each phase are prevented from expanding to the same extent as if they were separate phases. Thus, lattice parameter and mismatch measurements obtained from coherent precipitates would not be equal to those obtained in the unconstrained state. The constrained misfit, ε, has been related to the unconstrained mismatch, δ (33, 34); typically $\varepsilon = (2/3)\delta$ (35, 36).

As an element is added to a γ-γ' alloy, it is usually not distributed equally between the two phases, but instead partitions preferentially to one of them. As a result, alloy additions can influence the magnitude of the γ and γ' lattice parameters, thereby producing a change in mismatch. Aluminum and titanium preferentially partition to the γ' phase (10). The Ti:Al ratio has been shown to have a strong effect on the γ-γ' mismatch (10,

11, 37, 38) but has affected the γ' volume fraction as well (11, 37). The Ti:Al ratio also has been correlated with the APB energy of γ' (14, 19, 39-41). It is clear that changes in alloy chemistry may produce variations in lattice mismatch, although other important parameters may be affected as well. Thus, it is sometimes difficult to separate the specific effects of a particular element.

Molybdenum and chromium partition strongly to the γ matrix (10, 11, 42), and Mo provides a large increase in the γ lattice parameter. In Ti-free alloys, Mo can dissolve extensively in γ', although the substitution of Ti for Al significantly reduces the solubility of Mo and Cr in γ'. It has been demonstrated that Mo has virtually no effect on the Al and Ti contents of γ' (11). Thus, it appears that Mo is an element which can be used effectively to alter the γ-γ' mismatch without influencing the γ' composition and APB energy (36) in Ti-bearing alloys.

In a variety of nickel-base superalloys, the γ' particles have been observed to change from spheres to cubes and ultimately to rods or plates as the lattice mismatch increased (11, 30, 43-48). Although there were differences between alloys, spherical precipitates generally were observed when the magnitude of the misfit ranged from 0.0 to 0.3 pct. The cubic shape developed for mismatch values greater than 0.3 pct. (47). It appears that the cubic shape occurs as a result of elastic modulus anisotropy; the cubic shape minimizes the elastic coherency strain at (001) γ-γ'

interfaces (30, 37, 43, 45). Thus, the equilibrium particle shape is determined by an appropriate balance between surface energy and strain energy (43). Other investigators (49) have cautioned against the use of γ' morphology as a means of estimating the lattice misfit. Correlations between particle morphology and misfit are correct only if precipitates of comparable sizes are considered, because particle shape can change in an alloy with a given misfit during precipitate growth (37, 43, 48, 49).

Precipitate Coarsening

Theory

A theory of volume diffusion-controlled coarsening, or Ostwald ripening, was developed independently by Lifshitz and Slyozov (50) and by Wagner (51), following the work of Greenwood (52). Coarsening processes occur because a distribution of particle sizes exists, and the solubility of the precipitates in the matrix is a function of the size of the precipitate. When small particles of a phase are dispersed throughout a continuous matrix, the Gibbs free energy of the system can be reduced if the number of particles in the system decreases while their average size increases. Thus, a situation of competitive growth occurs in which the larger particles grow at the expense of the smaller ones, and the volume fraction of the precipitate remains essentially constant. The driving force for such precipitate growth is the reduction in the total surface energy, or interfacial energy, of the system. The

rate of coarsening is governed by the rate at which solute is transferred in the matrix from the shrinking particles to the growing particles.

The theory predicts that the average particle radius, $\bar{r}$, should increase with time t according to the following equation (53):

$$\bar{r}^3 - \bar{r}_o^3 = kt \qquad [2]$$

where $\bar{r}_o$ is the average particle radius at the onset of coarsening. The rate constant, k, is given by (53):

$$k = \frac{2 \gamma_i D C_e V_m^2}{\rho_c^2 RT} \qquad [3]$$

where γ_i is the precipitate-matrix interfacial energy, D is the diffusion coefficient of the solute, C_e is the concentration of solute in equilibrium with a particle of infinite size, V_m is the molar volume of the precipitate, ρ_c is a constant related to the distribution of particle sizes, R is the universal gas constant, and T is the absolute temperature. The theory predicts that the particle size distribution is such that the maximum particle size is equal to 1.5 $\bar{r}$.

Experimental Observations

The coarsening behavior of γ' has been studied most extensively in the Ni-Al system (43, 53-55). The particle growth data for the nickel-base alloys containing ~6 wt. pct. Al was plotted

for cube shaped γ' as $(\bar{a}/2)$ versus $t^{1/3}$, where $\bar{a}$ is the average length of a γ' cube edge. The linear slope of these data yielded the coarsening rate, k. The observed coarsening behavior of γ' in Ni-Al alloys was in excellent agreement with the Lifshitz-Slyozov-Wagner (LSW) theory.

The LSW theory has been equally successful in describing the coarsening behavior of Ni-Ti (53, 56) and Ni-Si (53, 57) alloys. However, in the Ni-Si alloy after 16 hours of aging at 775^{o}C, a departure from the $t^{1/3}$ kinetics was observed. This deviation from linearity was associated with the loss of coherency of the γ' particles, as indicated by the formation of hexagonal networks of interfacial dislocations (57).

Additional fundamental data can be obtained from particle coarsening theory, if the concentration changes during coarsening can be measured precisely (53, 58). Specifically, experimental values of γ_i and D can be determined directly by the methods described by Ardell. The values of D obtained for Ni-Al and Ni-Ti alloys (53) agreed fairly well with the extrapolated values obtained independently from standard high temperature diffusion experiments (59). The experimental values of γ_i in these same alloys were believed to be satisfactory, based on theoretical considerations (53, 54).

The distribution of particle sizes obtained by experiment, however, did not coincide closely with the predictions of the LSW theory; this seems to be the major discrepancy between coarsening

theory and experimental observations. Specifically, the experimental distributions are much broader than the theoretical distributions, and the actual cut-off value is larger than 1.5 $\bar{r}$. The magnitude of the deviation from the theoretical cut-off values seemed to be related to the degree of lattice misfit (56, 57) and to the volume fraction of particles in the alloy system.

Effect of Volume Fraction

The LSW theory was developed assuming a random distribution of particles in which the average spacing was much larger than the average precipitate size. Therefore, this coarsening theory is strictly applicable when the precipitate volume fraction is small and approaches zero. As the volume fraction increases, the mean interparticle spacing decreases, the diffusion distances become shorter, and intuitively, the precipitate coarsening rates may be expected to increase. Thus, an attempt was made (60) to modify the LSW theory in order to account for the effect of volume fraction.

This modified LSW theory (MLSW) gives a broader particle size distribution, which corresponds more closely to the observed experimental results. The basic $t^{1/3}$ coarsening behavior remains unaffected by the MLSW theory; however the coarsening rate k is predicted to have a strong volume fraction dependence. Although the MLSW theory appears to account for the coarsening of precipitates in Cu-Co alloys (61), the kinetics of γ' coarsening in a variety of Ni-base alloys (62-66) were found to be independent of

volume fraction. Thus, it was concluded that the original LSW theory was capable of qualitatively describing volume diffusion-controlled coarsening in systems containing as much as 60 volume pct. precipitate (62).

An alternative approach, which considers impingements, or "encounters," of growing particles, was provided recently (67). Such impingements have been found to be problematic at volume fractions as low as 27 pct. (62, 68) and would occur as particle boundaries expand outward and approach those of other particles. A rapid diffusion interaction is suggested to transpire, causing the two particles to coalesce (67). Coalescence of neighboring particles will occur much more rapidly than particle growth by volume diffusion, which occurs over large distances equal to many particle diameters. Other investigators (48, 69, 70) have recognized the possible influence of impingements on precipitate morphology. It has been suggested that precipitate morphology is as much influenced by the overlap of diffusion fields, which would cause particle impingement and irregular shaped particles, as by any associated strain effects.

The overall effect of coalescence is to increase the growth rate of the precipitate and broaden the particle size distribution (67) predicted by the LSW theory. The theory described above is called the Lifshitz-Slyozov encounter modified theory (LSEM), and thus far, accurate distribution functions have been obtained with it for small volume fractions between 15 and 30 pct. (48). In

addition, another theoretical study has derived a kinetic equation for Ostwald ripening which takes into account the effect of precipitate volume fraction (68).

Influence of Misfit

There is some evidence that the coarsening rate k of γ' in nickel-base alloys is also affected by alloying additions. Changes in composition would alter k in Equation [3] by directly affecting C_e, D, or γ_i. Specifically, Co and Mo each appear to retard growth of γ' (48, 65, 71), whereas Cr appears to increase the coarsening rate (67, 72). According to three independent investigations (22, 37, 73), the rate of γ' coarsening may decrease with increasing Ti:Al ratio. This latter observation is in contradiction with Decker (1, 2), who concludes on the basis of Fell's work (74), that higher Ti:Al ratios increase the coarsening rate.

Differences in coherency strains and mismatch also can accompany changes in composition because of partitioning factors. Decker (1, 2) acknowledges the possible influences of C_e and D on coarsening rate k. He also appears to conclude, from a limited number of studies, that increasing the lattice misfit increases k. However, a review of the results of a number of independent investigations in which the γ-γ' mismatch and γ' coarsening rates were measured did not reveal any consensus. The results of these investigations can be divided into three categories. Alloys with a higher lattice mismatch exhibited either:

a) higher γ' coarsening rates (48, 74);

b) lower γ' coarsening rates (22, 37, 63, 71, 73); or

c) no effect on γ' coarsening (45, 63)

in comparison to alloys of a similar, but slightly different, composition. Thus, a significant body of data exists which contradicts the generally accepted ideas of Decker (1, 2) and others (14, 25, 49).

There are three possible conclusions which can be drawn from the above literature review (75). First, if misfit were to have any effect, it would appear to have a tendency to decrease the rate of γ' coarsening. Secondly, it is possible that the effect of misfit is being overshadowed by changes in other parameters, such as D and C_e, which can also be produced by the same compositional variations used to change the misfit. The third possibility is that the surface energy, which is the actual driving force for coarsening, does not contain the elastic coherency strain term. The last conclusion requires a more extensive explanation which is given below.

As indicated previously, the driving force for coarsening is the reduction in the total surface energy, or interfacial energy, of the system. Nicholson (76) divides the interfacial energy γ_i into two components: the elastic strain energy term and the "chemical" component. The elastic strain energy is dependent upon the total volume fraction of the precipitate and the lattice misfit;

it is independent of particle size. It is clear that this component remains constant during the coarsening process. However, the chemical component is proportional to the surface area per unit volume, and this is the driving force for particle coarsening. Thus, the elastic coherency strains, and hence misfit, should not affect the coarsening process directly (76, 77). However, alloys with a large misfit might be expected to acquire interfacial dislocations, and the precipitates would lose coherency with the matrix (35). If this does occur, then the rate of coarsening may be expected to increase because of an additional driving force, which is a surface area quantity associated with the misfit dislocations at the precipitate-matrix interface (76, 77). This additional term is sometimes called the structural component, γ_S (76). The loss of coherency of an array of γ' particles in Nimonic 80A was found to increase the coarsening rate (76).

Loss of Coherency

The loss of coherency between a growing precipitate and a matrix of similar crystallographic structure is associated usually with the development of interfacial dislocations (35, 78). A feature of γ' coarsening in nickel-base alloys is the apparent resistance of the precipitates to lose coherency, since γ' has been observed to grow to several microns in diameter and still remain coherent (47). However, the breakdown of coherency does occur, and dislocations have been observed at the γ-γ' interfaces

in many nickel-base alloys after aging treatments (31, 35, 57, 79-83).

The interfacial dislocations form three-dimensional hexagonal networks consisting of a/2 <110> type dislocations (80). These dislocations also are called misfit dislocations, because they relieve the coherency strain energy resulting from the mismatch in lattice parameter between the precipitate and matrix. For the most efficient relief of misfit, the interfacial dislocations are of edge character with their Burgers vector in the plane of the interface, and the extra half-plane extends into the plane with the smaller lattice spacing. The spacing, d, of the dislocations then is given by the Brooks formula (84):

$$d = \frac{|b|}{\delta} \qquad [4]$$

where $|b|$ is the magnitude of the Burgers vector and δ is the misfit which was described in Equation [1]. This entire three-dimensional arrangement of dislocations is sessile and cannot be built up by pure glide alone; dislocation climb must occur for the hexagonal array to develop (80). However, for a particular precipitate, the misfit dislocations may be of a mixed character, or have their Burgers vector inclined to the interface. In this case, $|b|$ would be interpreted as the resolved edge component of the dislocation and would be smaller in magnitude than that for pure edge dislocations (35, 85).

The important questions become when and how does this loss of

coherency occur; a number of criteria have been developed to consider this question. The energy criteria described below are all based on the particle radius being of a critical size which is inversely related to the misfit. For example, Friedel (86) has made a simple energy balance between the elastic strain energy of a particle before coherency loss and the subsequent increase in specific interfacial energy. For a spherical particle, the loss of coherency occurs when:

$$r > (4\ \gamma_s\ /\delta^2\ G) \qquad [5]$$

where r is the particle radius, γ_s is the "structural" component of the interfacial energy associated with the misfit dislocations at the interface, δ is the unconstrained lattice misfit, and G is the shear modulus of the matrix. This criterion can be applied to other particle shapes.

Brooks (84) has suggested a simple geometrical approach to an energy criterion in which the critical radius is related to the length of interface required to build up a mismatch equal to the Burgers vector of an interfacial dislocation:

$$r > (b/2\delta) \qquad [6]$$

Another more sophisticated energy criterion (87) predicts that there are two critical radii: r_{crit}, below which a precipitate cannot support a dislocation loop at its interface; and r*, below which it is still energetically favorable for a coherent precipi-

tate to grow at the expense of an incoherent one, because the latter is in a metastable state. The relations for the values of these radii are:

$$r_{crit} = [b/16 \pi \epsilon (1-\nu)][\ln (8 r_{crit}/b) + (3-2\nu)/4(1-\nu)] \quad [7]$$

$$r^* = [b/8 \pi \epsilon (1-\nu)] [\ln (8r^*/b) - 1 + (3-2\nu)/4(1-\nu)] \quad [8]$$

where ϵ is the constrained misfit and ν is Poisson's ratio.

These energy criteria are necessary but are not sufficient conditions for coherency loss of a growing precipitate. In order for coherency loss to occur, dislocations either must be nucleated at the interface or must be attracted there from some other source in the crystal. There are two ways in which the nucleation of misfit dislocations might occur. The first way is called prismatic punching. In this process, two dislocation loops of equal and opposite sign are nucleated; one loop remains at the interface and the other is repelled by the particle. Prismatic punching appears to have been suggested first by Brooks (84) and has been examined for a number of particle morphologies by Weatherly (88).

For the punching mechanism, both an energy criterion and a stress criterion must be satisfied (35). The stress criterion is based on the maximum shear stress which develops at the interface of an isotropic precipitate; it is a function only of misfit and elastic moduli and not of the particle size. Thus, only certain precipitates with a misfit greater than a critical amount, ϵ^T_{crit}, can lose coherency by punching. As long as the misfit of any

alloy exceeds the critical quantity, there should be no nucleation barrier for the punching mechanism. The stress in the matrix rises periodically to the theoretical shear stress as the particle grows, and each time this occurs, a loop should be formed.

Values have been calculated for the critical misfit which depends on particle shape and temperature. For spherical γ' particles at 930°C, the magnitude of the critical misfit is approximately 1.4 pct. (35, 88). A misfit greater than this value is very unlikely in nickel-base alloys, so punching of dislocation loops generally is not expected for γ' particles. Thus far, there is no experimental evidence of prismatic punching in Nimonic 80A (35) or in binary Ni-Al (89) or Ni-Si (79) alloys. However, prismatic punching is observed frequently when there is a sudden increase in the surface stress of a particle, such as during the quenching of an alloy which has two phases with different thermal expansion coefficients (76, 90).

Another way in which to lose coherency by the nucleation of dislocation loops is by the collapse of clusters of vacancies or interstitials (91). Except in irradiated materials, this process is most likely to occur when precipitates have a positive misfit with the matrix (76) and are of a composition which deviates from stoichiometry (35). There is some experimental evidence for the loss of coherency by this mechanism in θ' particles of an Al-Cu alloy (35).

The most likely method of coherency loss in nickel-base alloys

appears to occur by absorption or capture of the matrix dislocations (35). Dislocations would have to be attracted to the particle-matrix interface and then undergo climb to produce the hexagonal arrays of dislocations which are necessary to accomodate misfit. This process is somewhat similar to the theoretical model proposed by Brown et al. (87); there will be an attractive interaction between the elastic strain field of the precipitate and the strain field of the matrix dislocation only when the γ' size exceeds r_{crit} in Equation [7].

The loss of coherency of γ' is a slow process because of the lack of matrix dislocations available. Thus, the rate controlling process for the capture mechanism is the supply of dislocations to the interface; this would depend strongly on the initial dislocation density and on any plastic deformation resulting from creep or mechanical fatigue. The capture mechanism could have considerable implications on the thermal stability of γ' in nickel-base alloys at elevated temperatures. For example, the γ' precipitates which had lost coherency in a slip band region were observed to coarsen at a faster rate than the γ' particles in an undeformed section of a Nimonic 80 specimen (76).

Effect of Stress on γ' Coarsening

Changes in the morphology of γ' have been observed in commercial nickel-base alloys which were subjected to external stresses at elevated temperatures (9, 25, 92-97). The γ' phase

instabilities in these polycrystalline materials had a deleterious effect on the creep properties, because the interparticle spacing increased as the γ' particles agglomerated into stringer-like configurations. An increase in the interparticle spacing allows dislocation by-passing to occur, and this was thought to result in an early onset of tertiary creep and failure (94, 96, 97). Thus, coarsening of the γ' precipitate during creep was believed to weaken the material.

A study was conducted on Ni-Cr-Al alloys which had low γ' volume fractions between 12 and 16 pct. (98). The Cr and Al contents were varied to produce alloys with δ values ranging from -0.23 to +0.38 pct. Creep tests were performed at 700°C, and it was found that the longest rupture life and minimum in creep rate occurred in the alloy which had a lattice mismatch closest to 0.00 pct. The results of this study, coupled with the microstructural observations of coarsening during creep (9, 25, 92-95) and the ideas of many workers (1, 2, 14, 25), seem to have led to the conclusion that zero mismatch results in the maximum stability of the γ' structure under stress, and therefore produces the best creep properties. Therefore, optimum creep resistance at high temperatures ($> 0.6\ T_m$) was associated with zero mismatch, in conjunction with sufficient solid solution strength and a fine dispersion and high volume fraction of γ' (25). It was appreciated, however, that strengthening from coherency strains could be important for nickel-base alloys at low temperatures ($< 0.6\ T_m$) (24).

In later studies, the influence of the sense of applied uniaxial stress on the morphology of γ' precipitates was examined in Udimet 700 single crystals (99, 100). This nickel-base superalloy contains 35 volume pct. of coherent γ', and is reported to have a small positive misfit of 0.02 pct. Prior to testing, the alloy consisted of γ' cubes aligned along cubic directions in the γ matrix. When a tensile stress of 155 MPa was applied to an [001]-oriented crystal at 955^{o}C, platelets of γ' formed perpendicular to the stress axis. A compressive stress applied to an [001]-oriented crystal resulted in rods that were aligned parallel to the stress axis. However, examination of the micrographs in references 99 and 100 reveals that the plates and rods were neither very extensive nor continuous. In addition, the kinetics of these morphological changes were not considered. It was concluded (100) on the basis of these experimental results and those discussed previously (25, 98) that the alloy composition should be adjusted to minimize modulus mismatch, in addition to minimizing lattice mismatch.

In a subsequent study, the effects of stress coarsening of γ' on the tensile yield behavior of Udimet 700 single crystals were investigated (101). To accomplish this, [001]-oriented single crystals with platelet, rod, and cuboidal γ' morphologies were obtained by annealing the crystals under an applied tensile stress, an applied compressive stress, and zero stress conditions, respectively. Crystals with these three different γ' morphologies

were tensile tested between ambient temperature and 982°C. It was found that the yield strengths of the crystals having the same morphology remained relatively constant up to 760°C. The yield strengths decreased sharply above 760°C, and this drop-off was independent of γ' morphology. Thus, stress coarsening did not adversely affect yield strength or ductility. In fact, a slight improvement in low temperature yield strength was realized with the stress coarsened microstructures; this was related in part to the hexagonal networks of dislocations which developed at the γ-γ' interfaces. Thus, it was concluded that the elimination of γ' coarsening may not be necessary, if yield strength is the primary concern. However, since the yield strengths of these crystals of various γ' morphologies did decrease abruptly at the same temperature, the advantage of high temperature strengthening by stress coarsened structures was not anticipated.

Other studies of superalloy single crystals have indicated that tertiary creep was initiated as a result of gradual directional coarsening of γ' which occurred during steady-state creep at 850°C (32, 102, 103). In this nickel-base alloy, the lattice mismatch at 850°C was estimated at about -0.4 pct. by measuring the effective distance between parallel dislocations in the interfacial networks (31) and by the use of Equation [4]. The γ' cubes had coarsened into platelets which were oriented parallel to the applied stress (102). The authors also supported the idea that zero misfit was necessary for optimum creep resistance, because

they claimed that even a slight deviation from zero would assist mobile dislocations in deformation by climb (32).

More recent studies (81, 82) on single crystals of a Ni-Al-Mo-Ta composition have demonstrated that directional coarsening of γ' precipitates significantly enhances high temperature creep properties in the [001] orientation. This single crystal alloy possesses a large negative misfit, $\delta = -0.78$ pct., at room temperature. The application of a tensile stress during creep at 1038^{o}C promoted directional coarsening of γ' with broad faces of precipitate plates oriented perpendicular to the stress axis. The γ-γ' lamellae which developed were more finely spaced and more extensive laterally in comparison to the γ' stringers observed in previous studies. However, the directional coarsening behavior exhibited by this model Ni-Al-Mo-Ta alloy was comparable to that observed in a more conventional single crystal superalloy, NASAIR 100, which has a significantly smaller negative misfit at room temperature of -0.3 pct (104, 105).

In conventional nickel-base superalloys at high temperatures and low stresses, the operative creep mechanism is reported to be particle by-passing by combined glide and climb processes (31, 32, 106). Thus, the finely-spaced lamellar structure in Ni-Al-Mo-Ta single crystals provided a beneficial structure for creep resistance of [001]-oriented crystals, because circumvention of the γ' phase by dislocation climb would be eliminated (81, 82). By preventing the dominant creep mechanism from occurring at high tem-

peratures, significant creep deformation can proceed only by the more sluggish process of shearing of the γ' phase. Particle shearing involves complex dislocation motions, including diffusive slip of superlattice dislocation pairs. It was proposed (82) that diffusive slip in γ' could be influenced by solute segregation, which would increase the dislocation drag stress. In this particular alloy, solute drag should increase as Mo saturation is approached; this effect may have accounted for the creep strength maximum which occurred in a similar Mo-containing alloy (107).

In addition, it was postulated (81, 82) that shearing of the γ' phase was retarded inherently by this lamellar structure because of the dense misfit dislocation networks present at the γ-γ' interfaces. Thus, part of the observed reduction in creep rate at 1038 and 899^{o}C was attributed to the formation of fine and continuous γ' platelets, commonly called γ' rafts. At low temperatures around 760^{o}C, the formation of fine-scale Mo-rich precipitates in the γ matrix appeared to contribute to improved creep properties (82), by providing further impedance to dislocation motion in the matrix.

The influence of an applied uniaxial stress on the morphology of coherent precipitates during coarsening has been predicted (108), using the theory of elastic inclusions and inhomogeneities (109, 110). The elastic energy associated with a particle shape change was calculated as a function of applied stress, lattice mismatch, and modulus mismatch between the precipitate and the

matrix. The precipitate volume fraction was assumed to be sufficiently low so that elastic interactions between particles were neglected. In addition, the precipitate and matrix were assumed to be elastically isotropic. Three morphological shapes of precipitates were considered in this determination: spheres, plates perpendicular to the applied stress axis, and needles parallel to the applied stress axis.

The calculations determined in the above mentioned study were used to construct a map which predicted the precipitate shape of lowest elastic energy for a certain set of conditions. Comparison of the map to the γ' shape changes observed in various nickel-base superalloy single crystals (81, 100, 102, 104, 105, 111) shows relatively good agreement between theory and experiment. However, the ratio of the precipitate modulus to the matrix modulus, E_p/E_m, is very influential in predicting the regime for a specific precipitate morphology, yet the modulus ratio is rarely known precisely. Pineau suggests that a reasonable estimate of this modulus parameter is 0.80 (108), based on elevated temperature data of Ni_3Al (112) and pure Ni (113). This value has proven to be substantially different from the actual E_p/E_m determined in a Ni-Al binary alloy (111) and has placed the alloy in a different morphology regime as a result. Thus, use of this plot appears limited without precise values of matrix and precipitate moduli for each alloy under consideration. Misfit measurements at the testing temperature also appear to be necessary, as has been sug-

gested elsewhere (82, 104). Finally, plates parallel to the applied stress axis have been observed experimentally (102, 104); theoretical predictions should incorporate such a precipitate shape and orientation.

Influence of Misfit: Summary

The influence of misfit on properties still remains unclear; a large mismatch in lattice parameter may be beneficial for some alloys under certain testing conditions and detrimental for others. This lack of agreement could stem in part from the difficulty of measuring γ-γ' misfit, since different techniques performed on the same composition have yielded different values of misfit, in terms of both magnitude and sign (24, 49). Variations in lattice parameter can occur from local changes in chemical composition and from constraints of coherency. In situ lattice misfit must be obtained after the precipitates have lost coherency (49), and this could be another source of the discrepancies found in the literature. In addition, the misfit obtained for the material at the service temperature is really the pertinent parameter (82, 104), since differences in coefficients of thermal expansion for γ and γ' (24, 36) lead to a temperature dependence of the γ-γ' mismatch. It is also possible that, within the same alloy, a certain value of misfit could be beneficial at one temperature and detrimental at another; this would depend on the operative deformation mechanisms and coarsening characteristics.

The γ' stringers observed after prolonged creep (92-95, 98) were obvious departures from the accepted periodic morphology of γ' dispersions. Thus, morphological changes were viewed with concern, and this prompted many proposals (25, 98-100) for eliminating γ' stringers through alloy design. However, there was only a small number of studies in which the misfit was varied in a series of nickel-base alloys and was correlated to creep properties. Only two studies (98, 114) showed that an increase in mismatch decreased the rupture life. It appears that if directional coarsening occurs slowly and the interparticle spacing increases simultaneously, then having a high misfit may be detrimental to properties. This would more likely occur in alloys with lower γ' volume fractions, because the distances for diffusion would be greater.

On the other hand, a number of studies (22, 37, 38, 73, 115) on nickel-base alloys have shown that an increase in misfit resulted in a higher creep life. Of course, additional complications can arise in such correlations, because compositional variations can change other material properties, such as γ and γ' hardening, APB energy, and diffusivity. It is possible that these effects could also contribute to property improvements. However, it has been demonstrated that a high mismatch alloy can exhibit greatly improved creep properties (81, 82), if directional coarsening remains fine and continuous and occurs in the testing temperature regime where climb would normally be the dominant defor-

mation mechanism. Finely-spaced γ-γ' lamellae are more likely to develop in high volume fraction alloys around 60 volume pct.

These results indicate that directional coarsening can exert a strong influence on the mechanical properties of nickel-base superalloys. However, the need for further understanding in this area is apparent. Investigations concerning the development of γ' morphologies under a given set of testing conditions, as well as the influence of various γ' morphologies on the mechanical properties, would appear to be of considerable interest. Although the improvement in creep strength achieved as a result of γ' rafting has been reported and the reasons for such improvements have been proposed (81, 82), the kinetics of the directional coarsening process have not been evaluated (47). In addition, almost no information is available on the factors which would influence rafting kinetics.

Statement of Purpose

The purpose of this study was to examine the kinetics of the formation and subsequent development of directional coarsening of the γ' precipitate in nickel-base superalloy single crystals. The Ni-Al-Mo-Ta alloy was studied primarily under tensile creep conditions, and its composition was very similar to that of Pearson and co-workers (81, 82). In the present investigation, the dimensions of the γ and γ' phases were related to creep time and creep strain in an attempt to trace the changing morphology under various

stress levels at 982 and 1038^{o}C. In addition, the influences of initial microstructure, as well as slight compositional variations, were related to rafting development and creep properties.

MATERIAL AND EXPERIMENTAL PROCEDURES

Material

Single crystals of a Ni-Al-Mo-Ta composition were produced by directional solidification using the withdrawal process.* The 1.25 cm diameter single crystal bars were heat treated in an argon atmosphere in the following sequence: 1277°C for four hours, 1288°C for two hours, 1299°C for two hours, and 1313°C for 100 hours in an effort to produce chemical homogeneity. The heat treated bars then were forced-air quenched to ambient temperature.

Single crystals of a second heat of Ni-Al-Mo-Ta were cast and heat treated in the same manner as the first composition. This second alloy was chosen to examine the effects of a slightly lower Mo content on the creep properties and resultant microstructure. The remainder of the experimental procedures described in this chapter were performed on the higher Mo-containing alloy, unless otherwise noted. The compositions of the alloys were determined by bulk wet chemistry and by microprobe; the results of the chemical analyses are given in Table I.

The microprobe was also utilized to examine the degree of

---

* Produced by TRW Metals - Turbine Components Division, Minerva, Ohio.

chemical homogeneity in the Ni-Al-Mo-Ta material achieved after the 100-hour heat treatment. To accomplish this, the as-cast and homogenized specimens were prepared metallographically, as will be described below, and microhardness indenter marks were placed on the prepared surfaces to delineate the areas to be examined. A 325 μm-long line scan was traversed across a dendrite arm in the as-cast material, and the Ni, Al, Mo, and Ta levels were determined at 40 μm intervals along this line. The homogenized material was analyzed as follows: 40 μm intervals were examined along each of three line scans which were 900 μm long. These three lines were 100 μm apart, so that a 200 by 900 μm area was analyzed on the specimen. Since the average primary dendrite arm spacing was measured to be 440 μm, the area analyzed by the microprobe after homogenization would have included several dendrites in the as-cast condition.

Tensile creep specimens with the configuration shown in Figure 1 were machined by precision grinding from the heat treated and air quenched bars. A limited number of machined specimens of both compositions were re-solutionized above the γ' solvus at 1313^{o}C for five minutes prior to creep testing in order to refine the γ' size. These latter specimens were rapidly quenched in oil from the homogenization temperature to ambient temperature. The quench of these specimens was much more severe than that of the other specimens, not only because of the quenching medium, but also because of the smaller section size. In addition, a few machined

test bars were aged at 982^{o}C for 115 hours to coarsen the γ' precipitates prior to creep testing.

Mechanical Testing

Constant load tensile creep tests were performed in air between 927 and 1038^{o}C on single crystal specimens having orientations within 10^{o} of the [001]. Two Pt/Pt-13 Rh thermocouples were attached at the ends of the specimen gage length to ensure that the testing temperature was maintained within ± 2^{o}C. Extensometer knife edges were placed in circumferential v-notches located at each end of the specimen gage length. Creep extensions were measured automatically with the extensometers and were recorded continuously as a function of time with linear variable differential transformers (LVDT's) and strip chart recorders. All creep measurements obtained were calculated directly from the strip charts upon which extension versus time were plotted for each test. The following data were obtained: strain at the onset of steady-state creep, ϵ_s; time to onset of steady-state creep, t_s; steady-state creep rate, $\dot{\epsilon}_s$; strain at the onset of tertiary creep, ϵ_t; time to tertiary creep, t_t; and time to failure, t_f.

Although some tests were run to failure, most creep tests were interrupted prior to failure at various times. Each interrupted test specimen was rapidly cooled to ambient temperature under load in an effort to preserve the dislocation substructures formed during creep, as well as to prevent further γ' coarsening.

Tensile tests also were performed on the single crystals between 927 and 1038°C and at strain rates of 1.1×10^{-4} sec^{-1} in order to characterize the material more fully. The specimen geometry, as well as the extensometry, was the same as that utilized for tensile creep testing. Engineering stress-strain data were obtained from two strip charts which ran simultaneously: one strip chart plotted load versus crosshead extension; and the other plotted specimen extension versus time.

Zero-Stress Aging Treatments

Specimens were aged under zero stress in order to compare the γ' coarsening rates to the kinetics of directional coarsening of γ' under creep testing conditions. One cm-thick sections of the air quenched, homogenized bars were aged at 982°C for 15, 115, 260, 452, 740, and 1025 hours and at 1038°C for 45, 115, 257, 500, 743, and 1030 hours. Each specimen was forced-air quenched after aging.

Specimen Preparation

Upon completion of testing, specimens were sectioned on a slow-speed saw along directions which were parallel as well as perpendicular to the applied stress axis. In addition, the as-cast, homogenized, and aged single crystals were sliced perpendicular to the [001] growth direction. Specimens were mounted in bakelite, and rough grinding was performed on 600-grit SiC paper. Mechanical polishing was continued on 3, 1, and 0.5 μm diamond and on

0.05 μm alumina; both mediums were on cloth-covered wheels. The polished surfaces were etched in a solution of 33 parts nitric acid, 33 parts distilled water, 33 parts acetic acid, and 1 part hydrofluoric acid. These prepared specimens then were examined by means of optical microscopy and scanning electron microscopy (SEM).

Thin foils of selected creep tested specimens and specimens aged under zero-stress were prepared for examination by transmission electron microscopy (TEM). Disks from the creep tested specimens were sliced parallel as well as perpendicular to the applied stress axis of the specimen. Disks from the aged samples were sliced normal to the [001] growth direction of the single crystals. Electro-discharge machining was performed on these sliced disks to produce wafers, 0.32 cm in diameter, which would fit properly into the double-tilt specimen holder for the electron microscope. The wafers after slicing were about 0.25 mm thick and were ground down further on 600-grit paper to a thickness of about 0.18 mm. Subsequently, the wafers were thinned electrolytically using a Struers twin-jet polisher with a solution of 45 pct. monobutyl ether, 45 pct. acetic acid, and 10 pct. perchloric acid at $0^{o}C$. Electropolishing was performed using a voltage of about 12 v. and a current of about 20 ma. The foils were examined in a Phillips EM 400 electron microscope at a 120 KV accelerating potential.

Line Intercept Technique

In order to analyze in a quantitative manner the changing morphology of the γ' phase, a line intercept technique was utilized in conjunction with the plotter of a Hewlett Packard 9835A computer. SEM photomicrographs containing the phases to be measured were placed on the plotter. A digitizing sight was used to mark the beginning and end of each phase, as the sight was traversed along a straight line across the micrograph. For this procedure, micrographs taken of longitudinal sections, parallel to the applied stress axis, were utilized. To obtain the raft length dimension, line scans were traversed in a direction perpendicular to the stress axis on the longitudinal micrographs. To obtain the raft thickness dimension and the interlamellar spacing, the line scans were traversed parallel to the stress axis, and the edge-to-edge distances of the γ' and γ phases, respectively, were determined.

A simple program was written to digitize the data for each line scan and to obtain means and standard deviations for the measurements. The volume fraction of the γ' phase was also determined using this line intercept technique. For each specimen, between 150 and 250 γ' particles or rafts were measured. Line intercepts containing the δ phase were avoided when quantitative measurements of the rafts were made.

Laue Back-Reflection X-ray Technique

The initial orientations of the single crystal bars, as well as the final orientations of selected specimens after mechanical testing, were determined by the Laue back-reflection X-ray technique. Transverse sections of the homogenized bars were prepared by the standard metallographic techniques described earlier. For the tested specimens, the grip end of each specimen half was used to obtain the initial orientation of the crystal, whereas the gage section yielded the final orientation of each crystal after mechanical testing.

The fracture surface of each failed specimen to be examined by the Laue technique was sliced off on a slow-speed saw. For the specimens which were interrupted during creep testing, the gage sections were sliced in half in a direction normal to the applied stress. The entire specimen half was mounted in epoxy. Then each grip end and gage cross section was rough ground on 600-grit SiC paper and mechanically polished with 0.3 and 0.05 μm alumina.

The polished surfaces were etched in a solution of 30 pct. concentrated hydrochloric acid and 70 pct. hydrogen peroxide (30 vol. pct.) after each step of the polishing sequence in order to remove any cold-worked material produced during polishing. This procedure permitted a sharp diffraction pattern to be obtained. The polished specimens were placed in a fixture designed to align the specimen axis parallel to the X-ray beam. Laue patterns were taken, and the initial orientations of all the single crystals and

the final orientations of selected specimens were determined.

Misfit Measurement Procedure

The in situ lattice mismatch between the γ and γ' phases was determined by X-ray diffraction (using Cu K_α radiation) for the Ni-Al-Mo-Ta alloy at ambient and elevated temperatures. The material utilized for this measurement was homogenized under the conditions described in the first section and then was aged at 1080°C for four hours and then at 870°C for sixteen hours, which simulates a typical coating cycle for turbine blades. The aged single crystals were aligned in a goniometer, and [012] and [001]-oriented slices were cut. These slices were prepared by the metallographic procedures described earlier. Diffractometer scans were performed at room temperature along the $(024)_{\gamma,\gamma'}$, $(012)_{\gamma'}$, and $(004)_{\gamma,\gamma'}$ peaks. The values for the lattice parameters of the γ and γ' phases were obtained from the positions of the peaks along the 2θ axis. In addition, an attempt was made to scan along the $(011)_{BCT}$ peak at room temperature in order to estimate the lattice parameters of the BCT (DO_{22}) Ni_3Mo precipitate.

For the high temperature X-ray diffractometer (HTXRD) studies, an [001]-oriented sample was aligned in the diffractometer and heated in a nitrogen atmosphere. The specimen was heated to 38°C and then subsequently heated up to 927°C in increments of 55°C. However, between 648 and 816°C, the specimen was heated in increments of 28°C to estimate the lattice parameters of the

BCT (DO_{22}) phase precipitates in this temperature range. After each increment, the temperature was stabilized for 120 seconds before the diffractometer scan of the desired peak was obtained. To determine the peak positions more accurately, the goniometer was run at 1/2° of 2θ/60 seconds; normal practice is 2° of 2θ/60 seconds. The lattice constants were determined then from the peak positions along the 2θ axis.

Phase Extraction

Phase extraction was performed to identify the interdendritic phase which was present in the as-cast material. This phase formed during solidification but was put back into solution upon subsequent heat treatment. In addition, phase extraction was utilized to identify another phase which precipitated during zero-stress aging treatments as well as during creep testing at 927°C and above. The extractions were performed according to standard procedures (10, 116, 117) on a sample in the as-cast condition, on a specimen which had been aged for 45 hours at 1038°C, and on a 598-hour life specimen which had been creep tested at 1038°C and 147 MPa. Each sample was sand blasted, cleaned in methanol, and weighed prior to the extraction. A platinum wire was spot welded to each sample which then was immersed in an electrolyte consisting of 10 pct. hydrochloric acid (by volume) and 1 pct. tartaric acid (by weight) in methanol. A platinum mesh was placed around the immersed sample and acted as a cathode during the elec-

trolytic process. All extractions were performed for three hours at room temperature and at a current density of 75 ma/cm^2.

The third phase was separated by anodic dissolution of the γ and γ' phases. After extraction, the electrolyte was poured through pre-weighed filters of 0.2 μm pore size. The weight pct. of the third phase was taken to be the weight of the residue on the filter divided by the total weight loss of the sample. The extracted residues were analyzed by the Debye-Scherrer X-ray method, using Cu K_α radiation with a nickel filter, as well as with diffractometer scans. The resultant d-spacings of the extracted residues from the as-cast material were compared to those for α-Mo. The resultant d-spacings of the aged and creep tested specimens were compared to those presented in the literature for the NiMo δ (118) and NiW δ (119) phases. Chemical analyses of the residues were also obtained from emission spectroscopy.

RESULTS

Microstructure of Single Crystals

The Ni-Al-Mo-Ta single crystal alloy contained several phases in the as-cast condition. As shown in Figure 2, its structure mainly consisted of the γ' precipitate in a matrix of γ, a nickel-rich solid solution. The γ' phase has been preferentially etched in Figure 2 and is depicted as the dark, irregular-shaped precipitate in this photomicrograph.

The interdendritic regions of this alloy in the as-cast condition were interspersed additionally with small amounts of a eutectic phase. Examples of this phase are shown in the optical micrographs in Figures 3a and 3b and in the SEM micrograph in Figure 3c. Energy Dispersive Analysis of X-rays (EDAX) was performed on this interdendritic phase *in situ*, as well as on areas of the γ-γ' matrix which did not contain this phase. Comparison of the peak intensities of the EDAX computer outputs showed that this interdendritic phase was Mo-rich. These results were confirmed by the analyses of extracted residue of this phase by the Debye-Scherrer X-ray method, as well as by diffractometer scans. The resultant d-spacings corresponded to those for α-Mo.

Subsequent heat treatment of the as-cast material removed most

of the microsegregation, eliminated the α-Mo eutectic, and refined the γ' dispersion in the γ matrix. The single crystal bars were heat treated in the following sequence: 1277°C for four hours; 1288°C for two hours; 1299°C for two hours; and 1313°C for 100 hours. The material was given this step-sequence so that the heavier elements, such as Mo, could diffuse sufficiently before the homogenization temperature of 1313°C was reached. Areas rich in Mo could otherwise undergo incipient melting at anomalously low temperatures, since residual microsegregation of Mo leads to the formation of the low melting point eutectic phase.

The total homogenization time necessary to reduce the amount of microsegregation to one pct. of its original value was estimated by the following equation (81, 120):

$$t = \frac{\lambda^2 \ln \delta}{4 \pi^2 D} = \frac{0.12 \lambda^2}{D} \qquad [9]$$

where λ, the primary dendrite arm spacing, = 0.044 cm;

δ, residual microsegregation, = 0.01; and

D, diffusivity of Mo in Ni, = 0.85 exp (- 64400/RT) cm^2/sec.

On the basis of Equation [9], 56 hours at 1313°C should have been sufficient to reduce the amount of microsegregation to one pct. However, visual examination of a specimen which was heat treated for 62 hours at 1313°C indicated that some segregation was still present; the dendrite arms were diffuse in appearance

but nonetheless identifiable. Thus, a 100-hour homogenization time at 1313^{o}C was chosen in an effort to achieve as homogeneous a structure as possible in a reasonable time frame. This homogenization time may be considered excessive, in comparison to commercial heat treatments, but it was desirable to remove local changes in chemical composition to ensure that a homogeneous γ' size and distribution, as well as accurate lattice parameter measurements, would be obtained. Faster solidification rates would reduce the dendritic arm spacings and required homogenization times.

To demonstrate the degree of chemical homogeneity achieved after the 100-hour heat treatment, the Ni, Al, Mo, and Ta levels in the as-cast and homogenized specimens were determined as a function of distance by the microprobe. The specimen areas examined in the as-cast and homogenized conditions are delineated by the microhardness indenter marks in Figures 4 and 5, respectively. The element levels in the as-cast material were determined at 40 μm intervals along a straight line which started at the single indenter mark on the left in Figure 4. This line was chosen so that an interdendritic region containing α-Mo would be analyzed. The line scan began in a dendrite core, crossed in an interdendritic region, traversed across another dendrite arm, and ended with the last point in an interdendritic region. The element levels at each 40 μm interval along this line are shown in weight pct. in Figure 6. The analysis showed that the interdendritic

areas were richer in Mo and lower in Ni. Elemental segregation during solidification was responsible for the formation of the α-Mo eutectic. The Al and Ta levels did not vary with distance to the same extent as Mo and Ni, but may have followed the same general trends as Ni.

The levels of Ni, Al, Mo, and Ta in the homogenized material were determined as follows: 40μm intervals were examined along each of three lines which were 900 μm long. These three lines were 100 μm apart, so that a 200 by 900 μm area was analyzed on the specimen. The first line scan was traversed between the indenter marks in Figure 5, and each successive scan was continued along a line that was 100 μm below. This area was chosen because it contained the greatest amount of segregation observed in the heat treated specimens. It is obvious from the micrograph in Figure 5 that most of the microsegregation had been removed after homogenization. The microprobe results are plotted in Figure 7 and clearly show that little variation in element levels can be discerned as a function of distance. Comparison of Figures 6 and 7 illustrates that the differences between elemental segregation in the as-cast and homogenized specimens were quite dramatic.

Solute segregation in the as-cast material not only promoted the formation of the α-Mo eutectic but also affected the size of the γ' precipitate (29). Scanning electron microscopy showed clearly that the γ' size was dependent upon the location within the dendritic structure. Figure 8 illustrates the change in γ'

size which exists at the interface between the dendrite core and the interdendritic region. The smaller γ' particles were located in the interdendritic regions rather than in the dendrite cores, which is the opposite of that observed in many other nickel-base superalloys (27, 121-124). The considerable differences in local solute composition (27) resulted in γ' size variations because the γ' solvus temperature varied within the dendritic structure. In this alloy, Mo depressed the γ' solvus in the interdendritic regions. Thus, on cooling from the homogenization temperature, precipitation of the γ' particles began first and coarsened more (125) in the dendritic cores.

Homogenization of this material removed elemental segregation, thereby eliminating the α-Mo eutectic and refining the γ' dispersion. An example of the homogenized microstructure is given in Figure 9. The microstructure contained cuboidal γ' particles which were 0.33 μm across. Although there appeared to be a normal distribution of particle sizes, the variable precipitate size and morphology which were observed in the as-cast condition had been eliminated by the homogenization treatment. Figure 10 is a TEM micrograph of the homogenized microstructure. At this higher magnification, it is clear that the γ matrix has a mottled appearance from the ultrafine γ', as well as the γ'' Ni_3Mo phase (82, 126), both of which formed upon cooling from the homogenization temperature. The latter precipitate has a BCT symmetry and a DO_{22}-type structure.

In situ Lattice Mismatch

An estimate of the mismatch in lattice parameter between the γ and γ' phases was determined by X-ray diffraction (using Cu K_α radiation) for bulk single crystal specimens of the Ni-Al-Mo-Ta alloy at ambient temperature. The values of 2θ, a, and δ are summarized in Table II for all of the diffractometer scans performed at room temperature. The in situ lattice misfit was calculated through the use of Equation [1].

In the first attempt, the single crystal utilized for this measurement was in the homogenized and air-quenched condition. Several diffractometer scans were performed on [012]-oriented slices of single crystals along the $(024)_{\gamma,\gamma'}$ peaks. A typical example of one of these diffractometer scans is shown in Figure 11. Although it appeared that the γ' $K_{\alpha 1}$ and γ peaks were separated, the γ peak was not prominent, and thus it was difficult to obtain an accurate value of $2\theta_\gamma$. Furthermore, the γ' $K_{\alpha 1,\alpha 2}$ doublet was not resolved clearly, which provided an indication that the measurement could be improved. The in situ misfit between γ and γ' was estimated at -0.52 pct. for the homogenized and air quenched sample at ambient temperature.

In another attempt, [012]-oriented slices were homogenized, air quenched, and then aged at 1080°C for four hours and at 870°C for sixteen hours. This aging treatment simulates a typical coating cycle for turbine blades and had a tremendous influence on the subsequent diffractometer scan along the

$(024)_{\gamma,\gamma'}$ peaks, which are illustrated in Figure 12. The γ,γ' $K_{\alpha 1}$ and γ' $K_{\alpha 2}$ peaks were clearly separated and very well defined, thereby enabling accurate values of 2θ to be obtained. The lattice parameters of γ and γ' were determined, and the *in situ* misfit of the homogenized and aged alloy was calculated at about -0.80 pct. at room temperature.

It should be noted here that, on the basis of the diffractometer scan of the (024) peak alone, the γ' peaks could possibly be interchanged with the γ peak, since the lattice parameters were so close in value. To determine if the peaks in Figure 12 were chosen correctly, and hence to confirm the negative sign of the misfit, a diffractometer scan was performed on the same aged sample but along the $(012)_{\gamma'}$ peak. This peak was chosen because the superlattice reflection would be allowed, whereas the fundamental γ reflection would be disallowed. The diffractometer scan of the $(012)_{\gamma'}$ peak is illustrated in Figure 13. As may be seen by comparing the values in Table II, the resultant lattice parameter corresponded to that for the γ' peak. Thus, the γ and γ' peaks were chosen correctly for the (024) diffractometer scan.

High Temperature X-Ray Diffraction

It was desirable to obtain misfit measurements as a function of temperature, and in particular, at the creep testing temperatures utilized in the present study. It was noted in the literature (23, 36) that misfit could be expected to change with in-

creasing temperature, primarily because of changes in thermal expansion between γ and γ'. Unfortunately, it was not possible to scan through the appropriate angles of 2θ for the $(024)_{\gamma,\gamma'}$ peaks with the present equipment for X-ray diffraction at elevated temperatures. However, the appropriate angles of 2θ could be obtained for the $(004)_{\gamma,\gamma'}$ peaks. Thus, a specimen was oriented parallel to [001] and prepared as before. Diffractometer scans were obtained at room temperature for the $(004)_{\gamma,\gamma'}$ peaks. The lattice constants were determined in situ and the unconstrained misfit was calculated. The values of these room temperature parameters are also listed in Table II.

Since these lattice parameters and mismatch values were reproducible for the (024) and (004) peaks at ambient temperature, high temperature X-ray diffraction (HTXRD) was performed. The results of the HTXRD study are summarized in Table III. The lattice parameters of the γ and γ' phases and the estimates for lattice misfit are also plotted as a function of temperature in Figures 14 and 15, respectively. With the exception of the range between 600 and 800^{o}C, the lattice parameter data of each phase followed a smooth curve from room temperature up to 927^{o}C. Furthermore, the lattice parameters of the γ and γ' phases increased with respect to temperature in about the same manner, since the γ and γ' data in Figure 14 followed approximately parallel lines. The lattice mismatch remained relatively constant from ambient temperature up to about 590^{o}C. However, at temperatures above 800^{o}C,

the difference between the lattice parameters increased somewhat, and as shown in Figure 15, this was accompanied by a slight increase in the magnitude of the misfit.

In the temperature range between 600 and 800°C, the lattice parameters and misfit deviated considerably from the overall behavior. Although both values decreased, it was apparent that the lattice parameter of the matrix was reduced more than that of γ' in this temperature regime. In response to this effect, the lattice mismatch was decreased substantially in magnitude from 0.79 to 0.55 in this temperature range, as illustrated in Figure 15. The temperature regime which was associated with these departures in lattice parameters in the present study overlapped with the precipitation of a Mo-rich DO_{22}-type phase, as was revealed recently by differential thermal expansion studies (82).

Although there appears to be no general method of describing the temperature dependence of lattice parameter data, a polynomial expression is sometimes used (127). Thus, the lattice parameter and mismatch data from 18 to 600°C and 800 to 927°C were fit to the following empirical equations by multiple regression techniques with the temperature data in centered form (128):

$$a_\gamma = 3.6140 + 3.2537 \times 10^{-5} T + 2.1037 \times 10^{-8} T^2 \qquad [10]$$

$$a_{\gamma'} = 3.5860 + 3.3807 \times 10^{-5} T + 1.7970 \times 10^{-8} T^2 \qquad [11]$$

$$\delta = -0.7782 + 4.1877 \times 10^{-5} T - 8.0005 \times 10^{-8} T^2 \qquad [12]$$

where T is temperature in ^{o}C. The predicted values of a and δ, as determined by the above equations, also are shown in Figures 14 and 15 and are represented by the solid lines. These equations fit the experimental data well, as may be seen qualitatively in Figures 14 and 15. Oxidation of the sample surface decreased the peak intensity to such a degree above 950^{o}C that the lattice constants and mismatch could not be determined directly at two of the creep testing temperatures utilized in the present study. Thus, Equations [10]-[12] were also used to extrapolate the data to slightly more elevated temperatures. Table IV contains the lattice parameters and lattice misfit, as predicted by Equations [10]-[12], at several temperatures including 982 and 1038^{o}C. The values of a and δ in the creep testing temperature regime appear to be reasonable.

As indicated previously, HTXRD performed on [001]-oriented slices revealed the existence of what appeared to be another phase. An extra peak with a discernable intensity was observed in a narrow temperature range, which coincided with that of the precipitation of the BCT (DO_{22}) Ni_3Mo (82). In the present study, it was noted that the $(004)_{\gamma}$ peak at 704.4^{o}C broadened considerably with respect to the $(004)_{\gamma}$ peaks obtained at lower temperatures. This broadened peak occurred because of the precipitation of this Mo-rich phase which had its $(008)_{BCT}$ peak position very close to that of the $(004)_{\gamma}$ peak. At 760^{o}C, the $(008)_{BCT}$ peak had shifted to a lower angle of 2θ such that it

had separated clearly from the $(004)_\gamma$ peak. At this temperature, the d-spacing of this phase was 0.916 Å, which was consistent with that reported for the BCT (DO_{22}) Ni_3Cb in Alloy 718 (129). Assuming a slight distortion in the BCT phase, such that c/a ~ 2.04 (129), the values of a and c were estimated at 3.59 and 7.33 Å, respectively, for Ni_3Mo in the present study. At 815.6°C, the γ phase exhibited a sharper (004) peak, and the extra peak from the Mo-rich phase was absent.

An extra peak from the BCT Ni_3Mo phase was not observed near the $(004)_\gamma$ peaks between 18 and 648°C. However, evidence of the Ni_3Mo phase at room temperature was provided by differently oriented single crystal slices. For example, an [012]-oriented sample was scanned along the $(011)_{BCT}$ peak at room temperature. A broad peak of very low intensity was discernable, and a d-spacing of 3.217 Å was estimated. Again assuming c/a ~ 2.04, a and c were measured at 3.58 and 7.31 Å, respectively, for Ni_3Mo at ambient temperature.

In an attempt to identify this phase more positively at elevated temperatures, diffractometer studies on an [001]-oriented sample were conducted at intervals of 28°C between 648 and 816°C. The lattice parameters that were obtained for the Ni_3Mo phase are listed in Table V. The studies indicated that the $(008)_{BCT}$ peak was starting to emerge at 676.7°C, although it was of such a low intensity that it was difficult to measure accurately. However, BCT peaks were observed and measured from 704.4 to 760°C.

In order to be certain that the $(008)_{BCT}$ and $(004)_{\gamma}$ peaks were being measured, and not the $K_{\alpha 1}$ and $K_{\alpha 2}$ peaks of the γ phase, another diffractometer scan was performed at 704°C. An $(003)_{\gamma}$, peak was obtained at a lower value of 2θ, because the fundamental γ reflection would be disallowed. Three peaks emerged from this diffractometer scan, and these corresponded to the $(003)_{\gamma}$, $K_{\alpha 1}$ and $K_{\alpha 2}$ peaks and the $(006)_{BCT}$ peak. Thus, the $K_{\alpha 1}$-$K_{\alpha 2}$ doublet of the γ phase could not be resolved even at elevated temperatures. At 787.8°C, the $(008)_{BCT}$ peak was absent, because this temperature was above the solvus of the Ni_3Mo phase (130).

Creep Properties

The homogenized Ni-Al-Mo-Ta single crystals were creep tested under several stress levels at 927, 982, and 1038°C. The typical creep curves for the specimens run to failure under these conditions are illustrated in Figures 16-18. Throughout this temperature regime, the creep curves exhibited stages of primary, steady-state, and tertiary creep, although the amount of primary creep was limited. The primary creep rate decreased continuously and was followed by a rapid transition into steady-state creep. The slope of the linear portion of the steady-state creep region was defined as the steady-state creep rate, $\dot{\varepsilon}_s$. The transition into tertiary creep appeared to be gradual at 927°C and became more abrupt as the testing temperature was increased up to 1038°C. The times and strains to the onset of steady-state

creep (t_s, ϵ_s) and to the onset of tertiary creep (t_t, ϵ_t) were obtained at the points in which the linear slope of the steady-state creep regime began to deviate from the remainder of the creep curve.

The creep rupture properties were characterized in terms of the stress and temperature dependence of the steady-state creep rate, $\dot{\epsilon}_s$, and the rupture life, t_f. The steady-state creep rate can be described by the following phenomenological equation:

$$\dot{\epsilon}_s = A \sigma^n \exp(-Q/RT) \quad [13]$$

where A and n are constants, Q is the apparent activation energy for creep, R is the universal gas constant, and T is the creep testing temperature in ^{o}K. The linear behavior of the double logarithmic plot of steady-state creep rate versus applied stress is illustrated in Figure 19 for the single crystals tested at 927, 982, and 1038^{o}C. Based on the limited stress ranges used, the values of the slope, n, were estimated at 8.7 for 927^{o}C, 9.2 for 982^{o}C, and 10.9 for 1038^{o}C. Although these values were slightly different, it was determined that the values of the stress exponent n were statistically equivalent throughout this temperature regime. Since the value of n was independent of temperature, then the apparent activation energy of creep was independent of stress. Thus, Q could be estimated by multiple regression techniques using the creep data at 927, 982, and 1038^{o}C. The coefficients, n and Q, of the regression equation were obtained and were found to be

equal to 10.0 and 475 ± 109 kJ/mol, respectively.

In addition, the stress and temperature dependence of the creep rupture lives was found to be described accurately by the following equation:

$$t_f = A \ \sigma^p \ \exp \ (-Q/RT) \qquad [14]$$

which is of the same form as Equation [13]. The linear behavior of the log t_f versus log σ data is illustrated in Figure 20 in the temperature regime between 927 and 1038°C. The values of the slopes, p, for these data were equal to -6.7 at 927°C, -7.5 at 982°C, and -8.1 at 1038°C. The confidence intervals around these slopes were obtained, and it was determined that the values of p were statistically equivalent. Since p was independent of stress, Q could be estimated by multiple regression techniques. The coefficients, p and Q, of the regression equation were determined to be 7.6 and 500 ± 67 kJ/mol, respectively.

The creep rupture life was inversely related to the steady-state creep rate by the Monkman-Grant expression (131):

$$t_f = A \ \dot{\epsilon}_s^{-m} \qquad [15]$$

The strain rate exponent, m, in this alloy was determined to be 0.77. This means that the rupture life does not vary as greatly with stress as does the steady-state creep rate. Therefore, the slope, p, of the log t_f versus log σ data was slightly lower in magnitude than the value of n.

A further attempt was made to describe the temperature and stress dependence of the various stages of creep. For example, the relationship between the time to the onset of steady-state creep, t_s, and the applied stress is illustrated in Figure 21. This figure shows that the transition into steady-state creep occurred earlier, in terms of absolute time, as the stress level was increased at a constant testing temperature. The onset of secondary creep also occurred sooner as the testing temperature was increased at a constant stress level. As shown in Figure 22, a similar behavior exists for the time to the onset of tertiary creep, t_t, with respect to the applied stress. For example, as the stress was increased at a constant temperature or as the temperature was increased at a constant stress, the time to the onset of tertiary creep was decreased. Comparison of Figures 21 and 22 with Figure 20 shows that the stress dependence of both t_s and t_t was similar to the stress dependence for the rupture life.

In addition, the fraction of the life spent in the primary plus steady-state creep regimes was related to the applied stress level. Figure 23 illustrates the stress dependence of the ratio of the time to the onset of tertiary creep, t_t, to the rupture life, t_f, for the temperature regime between 927 and 1038^{o}C. Although there appeared to be more scatter in these data, a general decrease occurred in the fraction of the life spent in primary plus secondary creep as the stress level was increased. This behavior was consistent with that depicted in Figures 21 and 22.

γ' Shape Changes During Creep

As shown in Figure 9, the heat treated material, prior to testing, had a conventional superalloy microstructure consisting of γ' cubes in a matrix of γ. However, when a uniaxial tensile stress was applied to an [001]-oriented single crystal, the γ' particles linked up to form platelets which had their broad faces perpendicular to the applied stress axis. The orientation of a γ' platelet within an [001]-oriented crystal is shown schematically in Figure 24. The microstructural changes which occurred in the Ni-Al-Mo-Ta alloy during creep under several conditions of temperature and stress will be considered in detail below.

A typical creep curve of the Ni-Al-Mo-Ta single crystals tested at 982^{o}C and 234 MPa is depicted in Figure 25. The times to the onset of steady state creep, t_s, and to the onset of tertiary creep, t_t, are indicated by the arrows in the figure. The open circles on the creep curve correspond to the specific times at which different specimens were taken out of the tests for examination. The corresponding microstructures of each of these specimens from the interrupted tests are shown in Figure 26. These scanning electron micrographs illustrate the development of directional coarsening of the γ' phase from a cuboidal to a plate-like morphology during creep. The micrographs in Figure 26 were taken from specimens that were sectioned parallel to the applied stress, such that the stress axis was vertical. The needle-like phase present in these micrographs is the NiMo δ phase; it formed

because of a supersaturation of molybdenum in this heat. The identification of this third phase, as well as the influence of this phase on the morphological changes of γ' and on the resultant creep properties, will be considered in a later section.

As may be seen in Figure 25, the crystal was in primary creep after five hours under a stress of 234 MPa at 982^{o}C. The corresponding microstructure in Figure 26a shows that some of the γ' particles had started to link together, although many were still individual cubes. The single crystal made the transition from primary into steady-state creep after 15 hours. The corresponding microstructure in Figure 26b shows that many more particles had joined into platelets. After 50 hours, the crystal was well into steady-state creep, and the γ' rafts continued to develop under stress, as is illustrated by the increased lateral extension of the rafts. In fact, at this time, the rafts extended completely across the area depicted in the micrograph in Figure 26d, and were about as fully developed as possible. That is, the rafts were continuous and interconnected, rather than being in the form of discrete particles or platelets. This γ' morphology did not change further with increased time of stress annealing from this point, up through the onset of tertiary creep. For example, the microstructure obtained from a specimen whose test was interrupted at 99.8 hours, which was after the onset of tertiary creep, indicates that both the length and thickness dimensions of the rafts were not significantly different from those after 50 hours.

Although the thickness of the rafts appeared to remain relatively constant throughout the creep test, the rafts in the failed condition had become more coarsely spaced, as shown in Figure 26g. The microstructure of the failed specimen in Figure 26g was representative of that away from the necked region; the uniform elongation of this specimen at failure was estimated at 5.5 pct. The microstructures of all the failed specimens were characterized along the entire gage length, that is, from the fracture surface to the fillet radius. Since the single crystal material had deformed to a greater extent within the necked region, thicker rafts developed in that region, as will be described later. The microstructures which will be presented for all of the failed specimens, unless otherwise noted, are representative of those within the uniform gage section, rather than in the necked region.

Specimens were also tested at 982^{o}C under a lower stress level of 186 MPa; a typical creep curve obtained under these conditions is illustrated in Figure 27. The creep specimens were taken out of the tests at various times; the corresponding micrographs of these specimens are shown in Figure 28. The changes in the microstructural features at 982^{o}C and 187 MPa were somewhat similar to those at 982^{o}C and 234 MPa, although the morphological changes in specimens tested at the lower stress level occurred at a slower rate.

As shown in Figure 28a, many of the γ' particles started to link together after 15 hours of testing at 982^{o}C and 186 MPa.

The γ' rafts had become more extensive laterally with increased time of stress annealing through the primary creep region. It is discernable certainly in the specimen tested for 199 hours that the rafts had become about as extensive as they were going to be under these conditions. Although there were specimen-to-specimen differences, the rafts did not appear to thicken with time, even in the failed condition. The one exception to this is the microstructure shown in Figure 28g, which was obtained by interrupting the creep test after 600 hours. The microstructure of this latter specimen did appear to be slightly coarser. However, because the microstructure of the failed specimen showed no thickening after additional deformation, it seems likely that specimen-to-specimen variations were responsible for the slightly coarsened structure in Figure 28g.

Specimens also were tested at a more elevated temperature in order to determine if the morphological changes of γ' and the rates of formation of the rafts were significantly different from those observed at 982^{o}C. A creep curve of the Ni-Al-Mo-Ta single crystals tested at 1038^{o}C and 179 MPa is illustrated in Figure 29. This combination of temperature and stress produced essentially the same creep properties as those which resulted from the tests at 982^{o}C and 234 MPa. This was fortuitous because it provided a good basis of comparison for examining the microstructural changes produced under two sets of conditions which resulted in equivalent creep lives and steady-state creep rates.

The micrographs obtained from the specimens whose tests were interrupted at various times during creep at 1038°C and 179 MPa are shown in Figure 30. As illustrated in Figure 29, the single crystal was in primary creep after five hours under stress. The corresponding microstructure in Figure 30a shows that most of the cuboids had started to link together, although vertical bridges of γ, which separate the γ' particles, were still present. The crystal made the transition into steady-state creep after 15 hours. The corresponding micrograph in Figure 30b shows that the rafts had become quite extensive in the lateral direction by this time. The platelets still had cusps of γ remaining between the original cuboids; however, many of the vertical bridges of γ that were present at five hours were absent after 15 hours of creep testing.

The crystal was well into steady-state creep after 50 hours, and the rafts continued to develop under stress. As may be seen in Figure 30c, most of the rafts extended from one end of the micrograph across to the other. The γ' morphology did not change further with increased time of creep testing, at least up to the onset of tertiary creep. This is illustrated by comparison of Figures 30c and d, the latter of which depicts the microstructure of a specimen whose test was interrupted just prior to the onset of tertiary creep.

Although the thickness of the rafts remained constant for the various specimens interrupted during creep under these conditions, the rafts in the failed specimen had become more coarsely spaced.

The microstructure of the failed specimen in the uniform gage section is shown in Figure 30e; in addition, the microstructure of the failed specimen within the necked region, directly in back of the fracture surface, is depicted in Figure 30f. Comparison of these two microstructures shows that the γ' rafts had coarsened further in the necked region. The overall development of the rafts at 1038^{o}C and 179 MPa was very similar to that which occurred at 982^{o}C and 234 MPa, although the rate at which the morphological changes took place was more rapid at the higher temperature.

Finally, specimens were tested at 1038^{o}C and 147 MPa for comparison to the morphological changes of γ' which occurred at the lowest applied stress at 982^{o}C. The typical creep curve obtained at 1038^{o}C and 147 MPa is shown in Figure 31, and the corresponding SEM micrographs of the specimens whose tests were interrupted during creep under these conditions are given in Figure 32.

As indicated in Figures 32 a-c, the γ' cuboids started to link together within the first fifteen hours of the test, and the γ' rafts continued to develop in the lateral direction up to 100 hours of creep testing. The transition into steady-state creep was obtained after 100 hours of testing and the γ' rafts seemed to have stabilized in both the length and thickness dimensions by this time. Thus, the changes in the microstructural features at 1038^{o}C and 147 MPa appear to be very similar to those which were

observed at the lower stress level at 982°C.

In addition, specimens were tested at three stress levels at 927°C, although no tests were interrupted during creep at this temperature. The microstructures of these specimens in the failed condition were examined and are shown in Figure 33. All of these specimens at this lower temperature had undergone directional coarsening of the γ' phase. The microstructure of the single crystal which exhibited the shortest creep life of 217 hours is shown in Figure 33a; the rafts in the uniform cross section appear to have cusps of γ remaining between many of the γ' particles which have linked together. The microstructure of the specimen with the longest life of 2850.4 hours is shown in Figures 33c and d; the rafts in the uniform cross section in Figure 33c were similar to those formed in the 535.7 hour-life specimen in Figure 33b. The rafts were coarser in the necked region near the fracture surface than in the uniform cross section. An example of the magnitude of this difference in raft thickness may be seen by comparing the microstructure in Figure 33c to that within the necked region in Figure 33d.

Quantitative Analysis

In order to quantify this changing morphology during creep at 982 and 1038°C, measurements of γ' raft length, γ' raft thickness, and interlamellar, or γ spacing, were obtained from the SEM photos of tested specimens. These dimensions of the γ and γ'

phases were measured by a line intercept technique used in conjunction with a computer. Line intercepts containing the δ phase were avoided, however, when quantitative measurements of the rafts were made.

The mean raft dimensions are plotted as a function of time in Figures 34-37 for each creep testing condition. Each data point in these figures represents between 150 and 250 measured γ' particles or rafts for each specimen tested. The lines delineated in these figures were obtained by standard least squares regression techniques. The times to the onset of steady-state creep, t_s, and to the onset of tertiary creep, t_t, also are indicated in these figures for comparison to the creep curves. The γ' volume fraction was measured in volume pct. to be 65.4 ± 1.5 at 927°C, 57.8 ± 0.7 at 982°C, and 61.3 ± 1.0 at 1038°C. Thus, the volume fraction was approximately constant at 60 percent in the temperature range of the interrupted creep tests. Furthermore, the volume fraction of γ' remained constant throughout the creep tests as a function of time; a typical example of this is shown in Figure 38 for the specimens tested at 982°C and 234 MPa.

The formation of the rafts began during primary creep for all of the testing conditions examined, as evidenced by the positive slope of the raft length data in Figures 34-37. Figure 34 illustrates that the mean raft length increased linearly with time up to almost 50 hours of creep testing at 982°C and 234 MPa. After 50 hours, the crystal was well into steady-state creep, and the

values of the raft lengths reached a plateau and remained constant thereafter. This plateau occurred when the microstructure consisted of continuous, interconnected γ' lamellae which extended from one end of the micrographs across to the other, as shown in Figures 26d-g.

The mean raft length in the failed specimen tested at 982^{o}C and 234 MPa was measured as having a slightly higher value than those of the specimens whose tests were interrupted in the latter part of second-stage creep. However, an increase in raft length was not a general trend that was measured in other specimens run to failure during creep under other conditions. As a result, the line for the mean raft length in Figure 34 was not drawn with an upswing to connect the data point at 120 hours. As will be discussed below, this higher value may be just the result of the considerably thickened plates in the failed condition, which would allow a longer intercept length to be measured.

In contrast to the raft length, the mean raft thickness remained constant at about 0.33 μm up through the onset of tertiary creep, as is illustrated in Figure 34. Linear regression indicated that the slope through these data points was not statistically different from zero. However, the single crystal in the failed condition had undergone a substantial increase in the total amount of strain during tertiary creep, and the rafts in the failed condition had coarsened considerably. As may be noted in Figure 34, this increase in thickness was abrupt, because the

specimen whose test was interrupted after tertiary creep had begun showed no increase in raft thickness. The interlamellar spacing, or thickness of the γ phase, also is plotted as a function of time in Figure 34, and these data displayed the same general behavior as the raft thickness versus time data.

The mean raft dimensions for the specimens tested at 982^{o}C and 186 MPa are plotted versus time in Figure 35. The behavior is similar to that displayed by the data at 234 MPa; the raft length increased linearly with time during first-stage creep. However, further increases in raft length were reduced substantially after 50 hours of testing, and the values of the raft lengths stabilized at 1.03 μm at about the onset of steady-state creep. In contrast to that which occurred at 982^{o}C and 234 MPa, both the raft thickness and interlamellar spacing remained constant throughout the creep curve, even in the failed condition. As shown in Figure 35, comparison of the raft length and thickness measurements for the failed specimen shows that both of these measurements showed similar trends; neither of these dimensions in the failed condition increased over those which were obtained for specimens whose tests were interrupted during steady-state creep.

Figure 36 shows as a function of time the quantitative results of the γ-γ' shape changes in the specimens tested at 1038^{o}C and 179 MPa. The directional coarsening behavior was very similar to that which was exhibited at 982^{o}C and 234 MPa. The raft lengths increased linearly with time up to about the onset of steady-state

creep. However, the rafting rate, which is indicated by the positive slope of the mean raft length data, was more rapid at 1038°C than that at 982°C; this result was anticipated by comparison of the photomicrographs in Figures 26 and 30. A plateau region was attained in mean raft length shortly after the transition was made into steady-state creep. Again a higher value in raft length was measured in the failed specimen, but the plateau was maintained at 1.17 μm for reasons which will be discussed in detail later. Both the thickness and interlamellar spacings were constant from the start of the test up through the onset of tertiary creep; however, in the failed condition, a substantial increase in these dimensions was measured.

Finally, the mean raft dimensions of the specimens creep tested at 1038°C and 141 MPa are plotted as a function of time in Figure 37. The raft lengths continued to increase with time past the onset of steady-state creep, but by 100 hours, the raft lengths had stabilized at a constant value. The thickness and interlamellar spacing both remained constant throughout the creep test, even in the failed condition.

The actual rafting rates which were obtained for the single crystals tested under the various stress levels at 982 and 1038°C are summarized in Table VI. The rafting rates were determined by the positive slopes of the mean raft length versus time data, shown previously in Figures 34-37. High correlation coefficients resulted from the simple linear relationship between raft length l

and time t. In addition, statistical relations were obtained for l^2 and t, l^2d and t, and $l^2\bar{d}$ and t, where d is the raft thickness of each specimen whose test was interrupted during creep and $\bar{d}$ is the mean of the raft thickness measurements obtained for the creep testing condition. These relations were utilized to express the rates of directional coarsening in terms of the volume of the rafts, rather than the length of the rafts. However, the latter regression equations did not improve the fit of the empirical data. As a result, the simple linear model of l versus t was used to describe the rafting behavior.

As indicated in Table VI, the rafting rate (a) increased as the temperature was raised to 1038°C and (b) increased as the stress level was raised at a given testing temperature. This is also depicted graphically in Figure 39, where the rafting rates at both temperatures are plotted against the applied stress levels. The slopes of the data in Figure 39 differed as a function of stress at 982 and 1038°C; however, the slopes were based on a limited number of data points. As a result, the apparent activation energy for rafting was estimated at the 179 MPa stress level using an Arrhenius relation analogous to that in Equation [13], and was found to be equal to 381 kJ/mol.

When it was determined that the slope of the raft length data with time in Figures 34-37 was not different from zero, the mean of the data was estimated, and a plateau region resulted. The time to the onset of the plateau in mean raft length is plotted as

a function of stress in Figure 40. As with the stress dependencies described previously for creep properties t_s and t_t, the time to the onset of the plateau in mean raft length decreased with increasing stress. In addition, the plateau in mean raft length was attained in less time during creep at 1038°C than at 982°C over the stress range utilized in the present study.

The influence of stress and temperature on the rafting behavior will be compared in more detail. The effect of applied stress on the slope of the mean raft length is illustrated in Figure 41 for the data at 982°C. The rafting kinetics from the beginning of the creep test to the onset of the plateau was about one and a half times faster at 234 MPa than at 186 MPa. As a result, the fully developed rafts in the plateau region formed sooner for the specimens at the higher stress level. As shown in Figure 42, a similar behavior was exhibited at 1038°C, although the difference in rafting rates was even more substantial at this higher temperature; the increase in raft length was nearly four times faster at 179 MPa than at 147 MPa.

Another way in which to examine the rafting kinetics data is to normalize the creep time based on the fraction of the total creep life. Figure 43 plots the mean raft length versus the fraction of the creep life, t/t_f, for the specimens tested under the two stress levels at 982°C. These two stress levels led to almost an order of magnitude difference in the rupture lives at this temperature. The graph in Figure 43 illustrates that the

specimens at the lower stress reached the plateau within the first fifteen pct. of the total creep life, whereas the specimens at the higher stress level attained the fully developed rafts after about half of the life had expired. However at 1038^{o}C, the difference in applied stress led to rupture lives which were a factor of 5 apart. When the difference in creep life was normalized as shown in Figure 44, the disparity in rafting rates between stress levels was reduced somewhat, and the specimens at these two stresses reached the plateau at similar fractions of their total creep lives.

The effect of temperature on rafting kinetics is illustrated in Figure 45. The mean raft length is plotted as a function of the creep time for the specimens tested at 982 and 1038^{o}C under the highest stress levels at each temperature. These two conditions of temperature and stress produced equivalent creep lives of about 120 hours, as well as equivalent steady-state creep rates. Comparison of the data in Figure 45 shows that the kinetics of rafting at 1038^{o}C were about three times faster than the kinetics at 982^{o}C for equivalent deformation rates. However, temperature seemed to have less of an effect on the rafting kinetics present at the lower stresses. Figure 46 illustrates that although the rupture lives were 598 and 831 hours at 1038 and 982^{o}C, respectively; the rafting rate was only about one and a half times faster at the more elevated temperature.

The relationship between the mean raft length and the creep

strain for the specimens tested at 982°C is presented in Figure 47, which illustrates that the behavior is similar for the data at both 186 and 234 MPa. The lines in the mean raft length versus creep strain plots were drawn using the predicted length values obtained from linear regression of the data in Figures 34-37 and the values of strain from creep curves in Figures 25, 27, 29, and 31.

Figure 47 shows that the raft length increased with increasing creep strain up to a plateau, however these data did not follow a linear relationship as did the raft length versus time data. Instead, the curvature in Figure 47 was related to the continually decreasing creep rate in the primary creep stage. The specimens at 234 MPa on average underwent more creep strain for a given raft length. When the rafts were fully formed, a plateau in raft length occurred at a creep strain of about 0.80 pct. at 186 MPa and 0.92 pct. at 234 MPa. However, the effect of time under creep is not indicated in this graph. Thus, the time that it took to attain a certain amount of creep strain was very different for the specimens tested at the two stress levels. For example, 50 hours were needed at 234 MPa in order to reach the plateau in mean raft length, whereas 130 hours were needed to reach the plateau at 186 MPa.

Figure 48 shows the relationship between the mean raft length and creep strain for the specimens tested at 1038°C. The specimens at 179 MPa exhibited the fastest rafting rate, and Figure 48

shows that the specimens underwent a relatively large amount of creep strain before the plateau in mean raft length was attained. In contrast, the specimens at 147 MPa underwent small increments of creep strain as the raft length increased up to the plateau.

Tensile Properties

Tensile tests were performed on the single crystals at strain rates of 1.1×10^{-4} sec^{-1} and temperatures of 927, 982, and 1038°C. Typical examples of the engineering stress-strain curves are illustrated in Figure 49. The microstructures of specimens which had been run to failure during tensile testing at 982 and 1038°C are shown in Figures 50a and b, respectively. It is apparent in Figure 50a that vertical bridges of γ separated many of the γ' particles after tensile testing at 982°C, so that directional coarsening was not well developed under these testing conditions. This specimen had a final elongation after testing of 17.2 pct. Directional coarsening was more developed after tensile testing at 1038°C; however, as shown in Figure 50b, the γ' platelets did not extend completely across the micrograph.

An experiment was performed to determine if accumulated strain would be sufficient to cause thickening of the γ' plates, similar to that which was observed after tertiary creep at the higher stress levels, but without allowing much time for diffusion to occur. To accomplish this, a specimen was creep tested at 982°C and 234 MPa; this test was interrupted after 50 hours of creep, so

that the microstructure of the specimen consisted of fully developed and finely-spaced rafts, similar to that in Figure 26d. The raft dimensions of this specimen corresponded to that within the plateau region in mean raft length in Figure 34. This pre-rafted specimen was then tensile tested to failure at a temperature of $982^{o}C$ and a strain rate of 1.1×10^{-4} sec^{-1}. The stress-strain curve for this pre-rafted specimen is compared in Figure 51 to that of the as-solutioned specimen, which was shown previously in Figure 49. Both of these specimens were tested under the same conditions of temperature and strain rate. The pre-rafted specimen exhibited a lower ultimate tensile strength (UTS) than the as-solutioned specimen, although both specimens had more comparable 0.2 pct. yield strengths (YS), because of the shapes of the curves. The pre-rafted specimen had a slightly lower amount of total elongation, 12.2 pct., as compared to 17.2 pct. for the as-solutioned specimen.

The values of UTS and 0.2 pct. YS are plotted as a function of temperature in Figure 52 for all of the tensile tested specimens, including the pre-rafted specimen, the latter of which is indicated by the solid symbols in the figure. The UTS and 0.2 pct. YS decreased in a similar manner as the temperature was increased from 927 to $1038^{o}C$.

Figure 53 shows a typical example of the microstructure of the pre-rafted plus tensile tested specimen. The microstructure obtained from the uniform gage section is depicted in Figure 53a; it

shows that the failed specimen had continuous and interconnected rafts which had not coarsened during tensile testing. The rafts which were directly behind the fracture surface also had not coarsened, as shown in Figure 53b. The dimensions of the γ and γ' phases of the pre-rafted plus tensile tested specimen were measured and are indicated by the solid symbols in Figure 54; superimposed on these data are the raft dimensions for the specimens which were interrupted at various times during creep at 982^{o}C and 234 MPa. The data show that the raft dimensions after pre-rafting for 50 hours of creep, plus tensile testing to failure, were essentially the same as those after 50 hours of creep.

Zero-Stress Aging

Specimens were aged under zero stress in order to compare the γ' coarsening rates to the kinetics of directional coarsening of γ' under creep testing conditions. The mean γ' particle size, $\bar{a}$, was measured as a function of time up to about 1030 hours of aging at 982 and 1038^{o}C. The results are depicted graphically in Figures 55 and 56, where $(\bar{a}/2)^3$ has been plotted as a function of time, in order to conform with the theoretical growth equations (53-55) presented earlier for γ' particles in nickel-base alloys. Each data point in Figures 55 and 56 represents between 150 and 250 measured γ' particles for each aged specimen.

As may be seen in Figure 55, the γ' particles underwent rapid coarsening at 982^{o}C even without an applied load. The mean γ'

size, $\bar{a}$, increased from 0.33 μm in the homogenized condition up to a plateau which occurred within 15 hours of aging at 982°C. The mean particle size in the plateau region remained constant at 0.44 μm up through 1025 hours of aging. However, the behavior of the aging data at 1038°C appeared to be different from that observed at 982°C. As shown in Figure 56, the $(\bar{a}/2)^3$ versus time data at 1038°C exhibited a positive slope over the time span from 0 to 500 hours of aging. The rate constant k, or γ' coarsening rate, was obtained from the positive slope in Figure 56 and was found by standard regression techniques to be 3.76×10^{-5} $\mu m^3/hr$. This linear slope was followed by a plateau in γ' particle size of 0.56 μm.

As indicated in Table VII, the γ' coarsening rate at 1038°C in the present study was more than an order of magnitude lower than the value of k extrapolated from the 775°C data of Ni-Al (43) binary alloys, as well as in more conventional superalloy compositions, such as Udimet 700 (64) and NASAIR 100 (75). In addition, it should be noted that the γ' coarsening rate for zero stress aging of the Ni-Al-Mo-Ta alloy at 1038°C was orders of magnitude lower than the kinetics of directional coarsening which occurred during creep at the same temperature. For example, the rate at which γ' directionally coarsened was 1.76×10^{-2} $\mu m^3/hr$ at 179 MPa and 6.67×10^{-3} $\mu m^3/hr$ at 147 MPa. For comparative purposes, the directional γ' coarsening rates expressed above are in the same units as the unstressed coarsening rates. Since the

γ' coarsening rate for aging is defined as the rate at which the volume of an average γ' particle increases with respect to time, the stressed γ' coarsening rate was expressed as the increase in the volume of an average γ' plate as a function of time. The volume of the γ' plates was approximated for each interrupted creep specimen by multiplying the raft thickness by the square of the raft length. Of course, for both stressed and unstressed aging, as the γ' particles or platelets increase in size, the total number of individual particles or platelets decreases, such that the total γ' volume fraction remains constant. As was shown earlier in Figure 38, the γ' volume fraction was constant during creep as the γ' plates increased in length.

The γ' precipitates and misfit dislocation networks of a specimen which was aged for 114.9 hours at 982^{o}C are shown in Figure 57. This aged specimen had a γ' size which was on the plateau of the $(\bar{a}/2)^3$ versus time data shown in Figure 55. The misfit dislocations were arranged in regular arrays around the γ' precipitates, which is indicative of the three-dimensional hexagonal networks of a/2 <110> edge dislocations observed previously in the γ-γ' interfaces of other nickel-base alloys (32, 57, 80, 93, 101, 132) after long-time high temperature exposures.

Figure 58 shows the microstructure of a specimen aged for 45 hours at 1038^{o}C. The size of the precipitate had not stabilized after 45 hours of aging, since the mean particle size for this specimen was on the positive slope of the $(\bar{a}/2)^3$ versus time

data in Figure 56. However, as evidenced by the rather complete hexagonal dislocation networks at the γ-γ' interfaces shown in Figure 58, the γ' cubes had lost coherency with the matrix. There are also dislocations in the γ phase in Figure 58 which appear to connect the misfit dislocation networks which surround one γ' particle with the networks which surround a neighboring particle.

Effect of Initial Microstructure

To examine the effect of starting microstructure on subsequent raft formation, three different γ' sizes were produced in the single crystals prior to creep testing by the following methods:

(a) forced-air quenching from the homogenization temperature,

(b) forced-air quenching from the homogenization temperature plus aging at 982^{o}C for 115 hours, and

(c) oil quenching from the homogenization temperature.

The forced-air quenched bars in (a) were considered to be the baseline condition, since the majority of the single crystals were heat treated and quenched in this manner. The raft dimensions of the air quenched bars have been described previously as a function of time during creep. The three different microstructures which were produced prior to creep testing are shown in Figure 59.

The forced-air quenched single crystals in Figure 59a had a mean γ' size of 0.33 μm. Misfit dislocations were present in this condition in the γ-γ' interfaces, although they were not arranged into regular arrays. The γ' cuboids had begun to coarsen and lose

coherency during the quench from the homogenization temperature. The microstructure of the single crystals which were aged for 115 hours at 982^{o}C is shown in Figure 59b; it consisted of γ' particles which had coarsened from the baseline size of 0.33 μm to a size of 0.44 μm. In addition, three-dimensional hexagonal networks of misfit dislocations were present in the γ-γ' interfaces. Oil quenching refined the γ' size to 0.15 μm, and reduced the interparticle spacing, as indicated in Figure 59c. The γ' cuboids appeared to be aligned more along cube directions than the other starting microstructures. Misfit dislocations were absent in the oil quenched condition; however, δ fringes were observed at the coherent (001) γ-γ' interfaces. These fringes are the result of the tetragonal distortion of the γ matrix at the interfaces because of the difference in lattice parameter between the two phases (89).

The initial microstructures produced prior to creep testing had a significant effect on the subsequent creep properties. The creep curves obtained from testing these specimens with the different microstructures noted above at 982^{o}C and 234 MPa are shown in Figure 60; the creep rupture lives and steady-state creep rates of these specimens have been listed in Table VIII, as well, for comparison purposes. The aged specimen had a creep life which was equal to approximately half of the life of the baseline specimen. Oil quenching increased the life from the baseline of 120 to 189.1 hours, and reduced the steady-state creep rate by a factor

of two.

In addition, the short time creep curves have been considered to examine the way in which the single crystals deformed initially as a result of their starting microstructures. The initial portions of the creep curves in Figure 60 have been enlarged to show the appropriate details for the first 15 hours of creep at 982^{o}C and 234 MPa and are illustrated in Figure 61. The aged and air quenched single crystals had similarly shaped creep curves at the shorter creep times. These specimens exhibited a continually decreasing slope through the primary creep stage, which was followed by a rather rapid transition into steady-state creep. The aged material made the transition into second-stage creep after nine hours, whereas the air quenched single crystal was into steady-state creep by 15 hours. The similarly shaped creep curves of the aged and baseline single crystals can be correlated with their similar starting microstructures, both of which consisted of γ' particles with misfit dislocations present in the γ-γ' interfaces.

It should also be noted that the dislocation structure in the air quenched specimen after five hours of creep testing was even more similar to that in the aged crystals prior to testing. As shown in Figure 62, the misfit dislocations in the air quenched specimen were arranged in regular arrays around the γ' precipitates after five hours of testing. Comparison of Figures 59a and 62 indicates that the misfit dislocations which formed after the short-time creep exposure were more completely developed than

those which were present prior to testing in the air quenched condition. Figure 62 also shows that the interfacial dislocation networks were developed in the air quenched specimens before the rafts were formed, which was also the situation for the aged crystals in Figure 59b.

Figure 61 shows that the short time creep curve of the oil quenched single crystal was S-shaped, in contrast to the creep curves of the specimens in the other starting conditions. Initially, the creep rate of the oil quenched specimen was low, similar to that of an incubation period. This was followed, however, by a rapid primary creep rate which tapered off relatively quickly, as the accumulated creep strain approached 0.6 pct. The crystal made the transition into steady-state creep after about 30 hours of testing at 982^{o}C and 234 MPa. The differently shaped creep curve for the oil quenched condition seemed to be related to its significantly different starting microstructure, since its γ' size was less than half of that in the other initial conditions and no misfit dislocations were present prior to testing.

The development of directional coarsening in both the aged and oil quenched specimens was examined to some degree during creep at 982^{o}C and 234 MPa. The differences in the γ-γ' microstructures between these starting conditions persisted throughout the creep tests. Typical examples of the SEM micrographs obtained for the aged specimens are shown in Figure 63 as a function of time during creep. After 15 hours of creep, the aged single crystal was well

into the steady-state creep regime, but as evident in Figure 63a, directional coarsening was not fully developed in the lateral direction; vertical bridges of γ were still present. After 50 hours, the aged specimen had made the transition into tertiary creep, and the corresponding microstructure in Figure 63b shows that the thick rafts did extend at this time from one end of the micrograph across to the other. The microstructure of the failed condition specimen in Figure 63c was similar to that after 50 hours, although it appeared to have coarsened further.

An attempt was made to quantify the changing morphology during creep at 982^{o}C and 234 MPa for the pre-aged specimens. SEM photos, such as those in Figure 63, were used to obtain measurements of γ' raft length, γ' raft thickness, and interlamellar spacing in a manner similar to that utilized for the baseline, air quenched material. The mean raft dimensions for the pre-aged specimens are plotted as a function of time during creep in Figure 64; their raft dimensions are indicated by the solid symbols in the figure. Superimposed on these data are the raft dimensions for the baseline single crystals, which were shown previously in Figure 34. The raft dimensions of the baseline single crystals are represented by the open symbols in Figure 64. In addition, the times to the onset of steady-state creep, t_s, and to the onset of tertiary creep, t_t, are indicated for comparison to the creep curve for the aged specimen, which was shown previously in Figure 60.

The data for the aged plus creep tested specimens in Figure 64 shows that the raft length versus time curve was offset but parallel to that for the baseline material. The kinetics for rafting were estimated by the positive slope of the mean raft length data. So, although the γ' particles had coarsened and had extensive misfit dislocation networks after 115 hours of aging at 982^{o}C, the kinetics of rafting for the pre-aged crystals were equal to that for the baseline material. The plateau in raft length occurred when the rafts were fully developed and extended from one end of the micrograph to the other. This was similar to that which was observed in the baseline material, although the onset of the plateau for the pre-aged specimens occurred during tertiary creep. The rafts were thicker in the pre-aged specimens; this raft thickness appeared to remain equal to the initial γ' size, although the rafts did coarsen further after the onset of tertiary creep. The interlamellar spacing appeared to follow a similar behavior as a function of time as the raft thickness data.

The differences between the rafting development of the oil and air quenched crystals can be dramatically illustrated by comparing the micrographs of these specimens with their short time creep curves, as demonstrated in Figures 65 and 66. The morphological changes which occurred after a creep strain of 0.003, which corresponded to a time of 1.5 hours for the oil quenched specimen and five hours for the air quenched specimen, are shown in Figure 65. It is apparent in Figure 65 that the rafting kinetics were more

rapid in the oil quenched material, since after only 1.5 hours, the length of the platelets which had formed appeared to be at least twice that of the original γ' size. A large number of γ' rafts seemed to have a high aspect ratio, although vertical bridges of γ still separated some cubes and small platelets. The lamellae which had begun to form were more regular and parallel to each other, apparently because the γ' particles prior to testing tended to be more aligned along cube directions in the oil quenched condition. However, many of the γ' particles in the air quenched specimen were still in the form of individual cuboids after five hours of testing; this structure had not directionally coarsened to any great extent. Thus, comparison of these micrographs shows that the rafts were more fully developed in the oil quenched specimens in one-third of the exposure time under the same testing conditions.

Figure 66 compares the microstructures of the oil quenched crystal and the air quenched crystal after a constant creep time of five hours. The oil quenched crystal had fully developed rafts after this short creep exposure; this specimen also underwent a higher amount of creep strain in the same amount of time. These micrographs in Figure 66 illustrate quite a substantial difference in the rafting rates between the oil and air quenched crystals.

The raft dimensions of the oil quenched specimens were measured as a function of time to substantiate the above mentioned microstructural observations, and are indicated by the solid

symbols in Figure 67. The baseline, air quenched data have been superimposed for comparison purposes and are indicated by the open symbols in Figure 67. The slopes of the mean raft length data show that the rafting rate of the oil quenched crystals was at least ten times faster than that of the baseline condition. Furthermore, the plateau in mean raft length for the oil quenched crystals was attained prior to the onset of steady-state creep. Specifically, the onset of the plateau appears to be at about 5 hours, whereas the air quenched single crystals had a plateau which occurred after 50 hours of creep. The thickness of the γ-γ' lamellae remained constant at the starting γ' size of 0.15 μm. As a result, the lamellae were considerably finer than those in the air quenched material, even in the failed condition after 189.1 hours.

Specimens were also oil quenched and tested in creep at 1038^{o}C, in order to determine if the benefits of having a finer γ' size could also be achieved at more elevated temperatures. It was found that similar property improvements were attained at 1038^{o}C and 179 MPa when the microstructure was refined prior to testing. For example, the creep life increased from 116.3 hours in the baseline material to 187.9 hours in the oil quenched condition; and the steady-state creep rate was reduced by a factor of four in the oil quenched material. The fine spacing of the γ-γ' lamellae also was maintained after long-time testing at this more elevated temperature. Figure 68 shows the finely-spaced rafts

which were present after 263 hours of testing at 1038°C and 147 MPa.

Third Phase Precipitation

Identification

After creep testing and zero-stress aging of the homogenized single crystal specimens, a needle-like third phase precipitated in the temperature range between 927 and 1038°C. This phase was present even after short exposure times; examples of this phase within the rafted microstructures have been shown previously in Figures 26, 28, 30, and 32. EDAX was performed on this phase *in situ*, as well as on areas of the γ-γ' lamellae which did not contain this phase after long-time creep testing. Comparison of the peak intensities of the EDAX computer outputs showed that this third phase was Mo-rich.

Phase extraction techniques were performed in an effort to obtain a more definitive identification of this third phase. In this procedure, the γ and γ' phases were dissolved preferentially in an electrochemical cell, leaving the third phase precipitates to be collected and subsequently analyzed. As shown in Figure 69, the third phase was often needle-like in appearance, although sometimes the phase was in the form of irregular or plate-shaped particles. The collected residue of the third phase was analyzed by emission spectroscopy; its composition was determined to be 65.9 wt. pct. Mo and 33.5 wt. pct. Ni. Trace amounts of Ta (0.5

wt. pct.) and Al (0.1 wt. pct.) were also detected.

The extracted residues were also analyzed by X-ray methods, and the resultant d-spacings were compared to those for the $Ni_{47}Mo_{53}$ δ phase (118) and the NiW δ phase (119). The X-ray data for the extracted residues in the present study could not distinguish unambiguously the orthorhombic δ phase from the tetragonal σ phase. This was not a surprising result, because other investigators (118, 119, 133-135) have had similar difficulties in discriminating an apparent σ or μ phase from a true δ phase. However, based on the phase diagram of the Ni-Al-Mo system (136-138), $Ni_{47}Mo_{53}$ δ was the most probable identification of this third phase.

Further confirmation of the identification of the δ phase was provided by the emission spectroscopy analysis of the extracted residue. The composition determined by this technique was very close in weight percent to that reported for the $Ni_{47}Mo_{53}$ δ phase (135), which ideally should be 64.8 wt. pct. Mo and 35.2 wt. pct. Ni. Using the density of δ (118) and the density of the Ni-Al-Mo-Ta alloy as determined by a regression technique (139), the weight fraction of δ phase, obtained from phase extraction, was converted to volume fraction and was estimated at 0.75 pct. However, quantitative metallography indicated that the volume fraction of δ was closer to 2.0 pct.

Microstructural Effects

The δ phase had caused some undesirable microstructural fea-

tures. For example, envelopes of γ' surrounded the δ precipitates, and these envelopes became more prominent as the time of the creep exposure increased. Figure 70 illustrates the extent of such an envelope which formed in a specimen with an 831-hour life after testing at 982^{o}C and 186 MPa. The δ needles with surrounding envelopes of γ' caused interruptions in the finely-spaced γ-γ' lamellae. Examples of the extent of these discontinuities within the γ-γ' lamellar structure are shown in Figure 71. The microstructural changes caused by δ appeared to be more pronounced in the oil quenched material, because the thickness of the γ' envelopes which encapsulated the δ needles was much greater than the thickness of the γ-γ' lamellae. This may be seen by comparing Figure 71a, which is representative of the oil quenched microstructure after testing at 982^{o}C and 234 MPa, with Figure 71b, which shows the microstructure of the air quenched material after testing under the same conditions.

Furthermore, the presence of the δ phase appeared to promote more irregular, less perfect lamellae. Generally, the δ phase precipitated homogeneously throughout the microstructure, because there was little microsegregation after heat treatment. However, one localized area was noted in a creep tested specimen in which the δ needles were nonexistent. The rafts which developed in this area without δ were more perfectly formed. The difference in the perfection of the rafts, within and outside of areas containing the δ phase, may be seen by comparing Figures 32b and 72. Both of

these microstructures were obtained from the same specimen after 50 hours of creep testing at 1038°C and 147 MPa.

Lower Mo-Containing Alloy

A Ni-Al-Mo-Ta single crystal alloy with a slightly lower Mo content was examined to determine the creep properties of a similar alloy which did not contain δ. The composition of this second heat of material is given in Table I; the Mo level in this second alloy was only 0.73 wt. pct. lower than that in Alloy 1. There were also small differences in the Al and Ta contents in Alloy 2. Significant improvements in creep life and steady-state creep rate were attained in the lower Mo-containing alloy when tested under the same conditions of 982°C and 234 MPa. As shown in Figure 73 and Table VIII, the creep life tripled in the air quenched crystals when the Mo content was reduced from 14.6 to 13.9 wt. pct.

The microstructure of the failed single crystal of the lower Mo-containing alloy showed that virtually no δ was present after 355.9 hours of creep testing at 982°C. Thus, the alloy was saturated, or very close to being saturated with Mo, but without being supersaturated, as was the case in the 14.6 wt. pct. Mo alloy. Figure 74 shows the highest density of δ observed in any one specimen area within the 13.9 wt. pct. alloy; comparison of this microstructure with that of the higher Mo-containing alloy in Figure 71b shows the significant difference in volume fraction of the δ phase, as a result of slight compositional variations.

The increase in creep life, which was realized when the single

crystals were oil quenched to refine the γ' size, was even more dramatic in the lower Mo-containing alloy than it was in Alloy 1. This is demonstrated clearly in Figure 73. For example, in the 14.6 wt. pct. Mo alloy, the life increased from 120 hours to 189.1 hours when an oil quench was performed prior to testing; the steady-state creep rate decreased correspondingly by a factor of two. However, in the 13.9 wt. pct. alloy, the life of the single crystal increased from 355.9 to 704.7 hours when the specimen was oil quenched; the steady-state creep rate decreased by a factor of over three. Thus, making slight compositional modifications improved the creep life of the baseline, air quenched material by a factor of three. However, refining the initial γ' size from 0.33 to 0.15 μm with an oil quench from the homogenization temperature, in addition to lowering the Mo content, increased the creep life by a factor of six.

DISCUSSION

In situ Lattice Mismatch

The value obtained for the in situ lattice misfit was affected significantly by aging the bulk single crystal specimen, which is consistent with the observations in reference 23. There are several possibilities which could account for the increase in the magnitude of mismatch brought about by aging at 1080°C for four hours and at 870°C for sixteen hours. First of all, the aging treatment may have caused the alloy to approach the equilibrium γ' volume fraction and equilibrium γ' composition. However, studies on nickel-base superalloys have indicated that this equilibrium volume fraction is achieved rapidly during heat treatment (140); the γ' volume fraction and the compositions of the γ and γ' phases remain essentially constant (11, 42, 64, 71) as a function of aging time. Certainly it is observed in Figure 9 that a high γ' volume fraction has been precipitated after homogenization only. The influence of the equilibrium volume fraction cannot be ruled out entirely, but it seems unlikely that this represents the main contribution toward the change in mismatch parameter after aging.

It is apparent in Table II that it was the value of $2\theta_\gamma$, and hence the lattice parameter of the γ matrix, which changed signif-

icantly after the aging treatment. Based on this observation, it seemed possible that this change was produced by additional DO_{22}-type Ni_3Mo precipitates, which formed in the matrix upon cooling from the aging temperature, as well as by needles of NiMo δ, which precipitated during the aging treatment. However, if the lattice parameter of the matrix was to have changed as a result of the precipitation of these Mo-rich phases, then a_γ would be expected to decrease as the matrix becomes more depleted of Mo to form these additional phases. Since a_γ actually increased after aging, it is very unlikely that the formation of the third phases was responsible.

The difference in lattice parameter and in situ misfit measured after aging is best explained by elastic coherency strain considerations. Figure 59a shows that the homogenized and air quenched single crystals of the Ni-Al-Mo-Ta alloy had some interfacial dislocations present, although these dislocations were not arranged into dense, hexagonal networks. Thus, the precipitates in this latter condition had begun to lose coherency with the matrix, but the γ-γ' interfaces were still constrained to some degree. As a result, the γ and γ' phases prevented each other from expanding in the same amount as they would have if they were separate phases. On the other hand, it has been demonstrated (81, 82) that this aging treatment resulted in γ' coarsening, as well as the formation of dense networks of misfit dislocations in the γ-γ' interfaces. These aged single crystals consisted of γ' which

had completely lost coherency with the matrix, and thus the precipitates and matrix were in an unconstrained state.

Therefore, it appears that the constrained misfit, ϵ, was actually being obtained in the misfit determinations for the homogenized single crystals; whereas the unconstrained misfit, δ, was being measured in the homogenized plus aged single crystals. As indicated earlier, the constrained misfit is related to the unconstrained misfit in the following manner (35, 36): $\epsilon \sim (2/3)\delta$. In the present study, the measured value of the misfit in the homogenized crystals (-0.52 pct.) was less than the average value of the misfit in the aged crystals (-0.80 pct.) by a factor of 2/3, which is in excellent agreement with the theoretical considerations. This result seems to lend further support to the idea that the increase in in situ lattice misfit was observed after aging, because the precipitates had lost coherency with the matrix.

Thus, the lattice parameter and mismatch measurements were not affected by coherency strains in the aged single crystals. These results are consistent with another study (49) which concludes that the true value of misfit can only be determined in situ when coherency constraints are negligible. Such constraints could be removed after precipitate coherency loss, as in the present study, or these constraints could be minimized if measurements by TEM techniques (49) were obtained at distances far from the γ-γ' interfaces. Unless otherwise noted, the remaining discussion will consider the unconstrained mismatch only.

In addition, it should be noted that the γ peak in Figure 12 does contain both the $K_{\alpha 1}$ and $K_{\alpha 2}$ peaks; however, the γ $K_{\alpha 2}$ peak was not distinguishable in part because of its low intensity. The position of the γ $K_{\alpha 2}$ peak may be a contributing factor as to why the γ peak does not return to a background intensity before the intensity starts to increase for the γ' $K_{\alpha 1}$ peak at higher values of 2θ. Furthermore, the sign for the misfit for this alloy could have been rationalized on the basis of Figure 12 alone. The peak with the highest intensity would most likely represent that of γ', because this phase had a higher volume fraction. This rationalization was indeed consistent with the additional data obtained from the $(012)_{\gamma'}$ peak.

High Temperature X-Ray Diffraction

The γ and γ' lattice parameters increased with increasing temperature because of thermal expansion. The thermal expansion of each individual phase is a function of the composition as well as the type of bonding present in that phase (36). The thermal expansion coefficient of the γ' phase generally has been found to be lower than that of the γ phase (36, 141), presumably because the former is an ordered phase. It has been suggested (36, 142) that the high strength atomic bonds within ordered, intermetallic compounds of stoichiometric composition would tend to resist expansion as the temperature is increased.

In the present alloy, the γ and γ' lattice parameters in-

creased with temperature in about the same manner from 18 to 593°C, and as a result, the thermal expansion coefficients and lattice mismatch were constant up to 593°C. However, above 815°C, the lattice parameter of the matrix increased more with respect to temperature than did that of the γ' phase. Thus, the magnitude of the misfit was observed to increase slightly. This temperature dependence of the unconstrained mismatch is consistent with that of other nickel-base superalloys (36, 75), which have a negative misfit where $a_\gamma > a_{\gamma'}$. The present alloy has a large negative mismatch because of the high Mo content which partitions primarily to the γ matrix. Thus, the constant mismatch at lower temperatures may be related to the high Mo content of the alloy, because it has been reported that increasing Mo levels in nickel-base alloys has lowered the thermal expansion coefficients of both the γ and γ' phases (36, 141). Alloys with higher γ' volume fractions and higher elastic moduli also exhibited lower thermal expansion coefficients for both γ and γ' (141).

The precipitation of the BCT Ni_3Mo phase greatly affected the lattice parameters and misfit within the 600 to 800°C temperature range, as was shown in Figures 14 and 15. In particular, the lattice parameter of the matrix was reduced significantly as the matrix was being depleted a bit in Mo in order to form the Ni_3Mo phase. This observation confirms the idea that the DO_{22}-type phase was not responsible for the change in γ lattice parameter and <u>in situ</u> lattice mismatch which occurred after aging,

because the value of a_γ increased after the aging treatment was performed.

Although the $(008)_{BCT}$ peak was observed near the $(004)_\gamma$ peak at temperatures between 677 to 760°C, the peak from this Ni_3Mo phase was not detected near the $(004)_\gamma$ peak at temperatures between 18 and 650°C. This Ni_3Mo phase is reported to precipitate between 772 and 800°C (82), although there was still some of this phase present at lower temperatures, because the aging treatment given to the single crystal specimens included a slow quench through the Ni_3Mo precipitation range. Thus, the BCT phase may not have been detected near the $(004)_\gamma$ peak from 18 to 650°C, because the thermal expansion was such that the lattice parameters of the two phases were too close to be separated. In other words, the BCT peak was probably buried under the γ peak, until at higher temperatures, the BCT peak expanded at a different rate with respect to temperature and separated from the γ peak. Additionally, the position of the Ni_3Mo peak, along with that of the γ $K_{\alpha 2}$ peak, could contribute toward the portion of the γ peak which did not return to a background intensity before the γ' $K_{\alpha 1}$ peak was obtained at higher values of 2θ.

The volume fraction of this Ni_3Mo phase was very small at low temperatures, which is why the $(011)_{BCT}$ peak obtained at ambient temperature was of such a low intensity. Thus, in the range of precipitation of this phase, a higher volume fraction would be present and the peak for Ni_3Mo would be of a more dis-

cernable intensity. This could be another contributing factor as to why the Ni_3Mo peak was not observed near the $(004)_\gamma$ peak until 677°C.

Creep Properties

The similarity of the stress dependent data in Figures 19-22 seems to imply that the same factors are controlling creep deformation between 927 and 1038°C. The stress exponent, n, for the steady-state creep rate and the apparent activation energy, Q, for creep were found to be large in magnitude, in comparison to that for pure metals or simple solid solutions. For these latter single phase materials (143-147), n is usually observed in the range of 3 to 6, and Q is equal to the activation energy for self-diffusion, Q_{SD}. For materials strengthened by a second phase, values of $n > 6$ and $Q > Q_{SD}$ are frequently observed (96, 148), as in the present study, where $n \cong 10$ and $Q = 475 \pm 100$ kJ/mol. The activation energy for the self-diffusion of Mo in Ni is equal to 288 kJ/mol (149) and that of Al in Ni is equal to 267 kJ/mol (59). Thus, in the present study for creep of a Ni-Al-Mo-Ta alloy, Q is also greater than Q_{SD}.

The apparent activation energy for the Ni-Al-Mo-Ta alloy may have been lowered to a value closer to Q_{SD}, if the applied stress σ in Equation [13] was normalized with respect to the elastic modulus, E. By incorporating E into the power law equation, differences between various materials have been taken into

account (145, 146, 150, 151), and the exponential term in Equation [13] can sometimes be replaced by the volume diffusion coefficient, D.

Another approach which rationalizes the high value of n and Q in two-phase alloys has been developed recently (152, 153), whereby the power law creep equation is expressed in terms of an effective stress, σ_e, rather than the applied stress, σ. The effective stress is defined as $\sigma_e = \sigma - \sigma_o$, where σ_o is a measure of the inherent resistance of the material to deformation. The same two phase alloys which yielded values of $n > 6$ and $Q > Q_{SD}$, when the steady-state creep rate was expressed as Equation [13], gave values of $n \cong 4$ and $Q \cong Q_{SD}$, when the effective stress was taken into account (144). Values of the back stress, σ_o, have been obtained by a variety of techniques, including incremental stress drop tests. Although this alternative approach appears to describe creep deformation of precipitation-hardened alloys fairly well, there is no consensus over the physical significance of σ_o, nor of the validity of the methods proposed to measure σ_o (154).

There was some experimental scatter in the creep data, as shown in Figure 19, although this scatter was not considered to be excessive. This Ni-Al-Mo-Ta alloy is anisotropic during creep at 1038^{o}C (82), so orientations were determined in the present study for selected single crystals before and after mechanical testing. The results indicated that the crystals did not undergo lattice rotations during testing. In addition, no trends in prop-

erty differences were revealed as a function of distance or direction off the [001] orientation. As a result, anisotropy was not considered to contribute to the experimental scatter of the creep data; the single crystals were all oriented within 10^{o} of the [001] orientation. Some of this scatter may have been the result of small specimen-to-specimen differences in γ' size, caused by slight variations in the quench rate from the homogenization temperature.

Finally, the ratio of the time to the onset of tertiary creep to the rupture life, t_t/t_f, was shown in Figure 23 to decrease as the stress level increased. This means that the total fraction of life spent in primary plus secondary creep increased as the stress was decreased. This behavior is the reverse of that observed in powder metallurgical nickel-base superalloys which were creep tested at intermediate temperatures (115). In these latter polycrystalline alloys, the ratio of t_t/t_f increased in a non-linear fashion as the stress level increased.

Morphological Changes of γ' During Creep

It is clear from examination of Figures 34-37 that the rafting behavior was very similar in all of the testing conditions studied. Directional coarsening began during primary creep, as evidenced by the raft lengths which increased with time in a linear fashion. The raft lengths continued to increase but then stabilized at a constant value which was attained rapidly, usually

within the first 20 pct. of the creep life of the specimen. This plateau in mean raft length signified that a change in the microstructure had occurred. Comparison of the raft dimension data in Figures 34-37 to the corresponding micrographs in Figures 26, 28, 30, and 32 shows that before the plateau was attained, the microstructure consisted of discrete particles or small platelets of γ' within the matrix. After the onset of the plateau, however, the microstructure consisted of γ-γ' lamellae which were continuous, interconnected, and fully formed. These rafts extended over large distances across the specimen diameter and were interrupted only by an occasional sub-boundary, or more locally, by needles of δ phase. This latter microstructural feature will be discussed more fully in a later section.

The rapid development of directional coarsening in the present alloy is contrary to the observations made in other superalloy single crystals, in which the agglomeration of γ' proceeded slowly during steady-state creep (32, 102, 103) and initiated the onset of tertiary creep. However, the raft development exhibited in the present alloy was comparable to that in a more conventional single crystal alloy, NASAIR 100 (104). Directionally coarsened γ' has also been observed during primary creep at 850^{o}C in another nickel-base alloy, Alloy 713 LC (155).

The mean raft length generally continued to increase after the transition was made into steady-state creep. This observation seems to support the idea that directional coarsening of γ' is

related to both accumulated strain and time. As suggested elsewhere (108), there may be limitations to the applicability of purely elastic considerations in the interpretation of morphological changes of the γ' precipitate during stress coarsening. Furthermore, since the plateau in mean raft length often occurred after the onset of steady-state creep, it appears that the formation of fully developed rafts was not directly related to the onset of second-stage creep. Apparently, sufficient strain hardening for the transition into steady-state creep was obtained by the material prior to the onset of the plateau in mean raft length.

The raft thickness remained constant in the present alloy as a function of time from the start of the creep test, up through at least the onset of tertiary creep; the interlamellar spacing exhibited the same behavior as the raft thickness data. This is an indication of the stability of the finely-spaced rafted structure, and is in direct contrast to the large increase in interparticle spacing, which caused the early onset of tertiary creep and failure in a number of nickel-base alloys (94, 96, 97).

The volume fraction of the alloy has been shown in Figure 38 to be constant as a function of time during creep. This was not a surprising result, because a number of studies (11, 42, 64, 71) have shown that γ' volume fraction remains constant as a function of aging time. Thus, directional coarsening did not occur by the precipitation of additional γ', but developed instead by a stress-assisted diffusion process. A mechanism for directional coars-

ening can be envisaged as follows. The γ'-forming species flow toward the vertical faces of unlinked γ' particles; and the species that are present in the vertical bridges of γ, which initially separate the γ' particles, diffuse simultaneously in the opposite direction. A competitive growth situation, similar to that in Ostwald ripening, is suggested to occur in the present alloy, whereby the small γ' particles dissolve at the expense of the larger particles which increase in length. As the platelets increase in length, the total number of particles in the system decreases, and thus the γ' volume fraction remains constant during the directional coarsening process. The application of the applied stress may cause relatively large γ' particles to dissolve as well, if they are unfavorably positioned with respect to nearby platelets which have started to develop. This selection of favorably located particles for growth has also been rationalized for zero-stress aging behavior in Ni-Al alloys (43). This mechanism seems to describe adequately the observation that the mean γ' raft thickness remained essentially unchanged with increasing creep time.

The apparent resistance to thickening of the γ' rafts in the present alloy can be compared to that of NASAIR 100 (75, 104), which also underwent rapid directional coarsening of the γ' phase. However, in the NASAIR 100 alloy, a gradual thickening of the rafted lamellae occurred after long exposures during steady-state creep. This latter morphological change was reported to result in

an early onset of tertiary creep and failure. The resistance to raft thickening in the present alloy may be related in part to the high mismatch in lattice parameter. The Ni-Al-Mo-Ta alloy had a misfit at the creep testing temperature which was approximately 0.2 pct. higher in magnitude than that of the NASAIR 100 alloy. As the mismatch increases in magnitude, the distance between parallel misfit dislocations becomes reduced, thereby providing a more effective barrier to penetration of the γ' phase by mobile dislocations. More effective barriers at the γ-γ' interfaces would delay appreciable γ' shearing until a point later during creep deformation, and as will be discussed below, γ' shearing may enhance raft thickening.

The composition of the alloy could also be contributing to the stability of the rafts by affecting other parameters in addition to misfit. For example, the Ni-Al-Mo-Ta alloy contains a high percentage of refractory elements, in comparison to NASAIR 100. Specifically, the matrix of the present alloy was saturated with Mo, and this could have a tendency to increase the dislocation drag stress, thereby slowing mobile dislocation motion (82). The impedance of dislocation motion would appear to reduce the rate at which γ' shearing and plate thickening would occur. Finally, the presence of δ phase may have indirectly affected the thickening behavior of the rafts, prior to tertiary creep. It has been demonstrated that the δ phase reduced the creep rupture life of the alloy by providing paths for dislocations to circumvent the γ'

rafts. Thus, it seems possible that this would actually reduce the amount of γ' shearing, thereby delaying the onset of raft thickening. Additional interrupted creep testing of the lower Mo-containing alloy could determine if the presence of δ phase did, in fact, delay the onset of raft thickening, as suggested here.

The rafts in the specimens which had failed after testing under the higher stress levels at 982 and 1038^{o}C had thickened considerably, in comparison to the finely-spaced rafts which were present during steady-state creep. This increase in thickness was an abrupt change, as shown in Figure 34 for the specimens tested at 982^{o}C and 234 MPa. For example, the specimen interrupted after 99.8 hours of testing, which was after the onset of tertiary creep, showed no increase in raft thickness. Thus, it appears that thickening may be enhanced by the substantial amount of total strain which was accumulated during tertiary creep. A mechanism of γ' raft thickening is suggested, whereby γ' shearing causes the formation of small ledges in the γ' phase at the γ-γ' interfaces. These ledges can enhance thickening of precipitate plates (25, 156). Thus, lamellar thickening in the present alloy would increase the mean slip distance of mobile dislocations. This would increase the creep rate, and in turn, produce more shearing and additional plate thickening, such that an autocatalytic process would develop (25).

The specimens which were run to failure under the lower stress levels at 982 and 1038^{o}C, however, did not exhibit an increase

in raft thickness. The difference in thickening behavior between specimens tested under different stress levels at the same temperature is still puzzling; specimens at all stress levels underwent similar amounts of total deformation after failure, as indicated by similar elongations and reductions in area. Since the raft thickness varied along the gage length within the failed specimens, in response to greater deformation within the neck, caution was exercised to ensure that micrographs for quantitative analysis were obtained at appropriate distances away from the necked region.

The line intercept technique is a reproducible, standard procedure used to make quantitative evaluations of microstructural features. The center-to-center spacings between alternating phases of a lamellar structure are difficult to determine experimentally and require arduous measurements (157). However, linear intercept techniques have been used successfully in the determination of edge-to-edge distances within lamellar structures such as pearlite (157). Thus, this measurement technique seemed appropriate for determinations of the raft thickness and interlamellar spacings, although the technique is limited by irregularities which do exist in the γ-γ' microstructure.

A microstructural feature which caused slight difficulty was that the platelets which developed in the alloy were not perfectly parallel to one another, but instead exhibited some waviness. So, although the lamellae in the plateau region were completely formed, an average intercept length of only ~1 μm was obtained, because of

the waviness in the structure. Thus, a fraction of the total raft length was obtained, as is shown schematically in Figure 75. However, the significant aspect of the plateau was not its magnitude; the plateau indicated that a change in the microstructure had occurred from discrete particles in a matrix to continuous and interconnected lamellae. Although the measurement technique had some limitations, the data obtained were internally consistent, and changes in the measured dimensions corresponded to observed changes in microstructural features.

As was mentioned earlier, a higher raft length intercept was mesured in the failed specimens which were tested at the higher stress levels at 982 and 1038^{o}C; these specimens underwent a substantial increase in raft thickness during tertiary creep. However, no increase in raft thickness was observed for the specimens tested at the lower stress levels at these same temperatures, and no increase in raft length was measured in the failed condition for these specimens. This correlation lends additional support to the idea proposed earlier that an increase in raft length measured in the failed condition was related to an increase in raft thickness. Considerably thickened plates in the failed condition would allow a longer intercept length to be measured, as a result of the waviness of the lamellae. Furthermore, there was no metallurgical reason for an increase in raft length to occur in the failed specimens, because the rafts were already essentially infinitely long, as they terminated at the edges of the specimen.

Faster rafting rates were obtained at more elevated temperatures because of more rapid diffusion rates at these higher temperatures. Higher stress levels also increased the kinetics for rafting by hastening the stress-assisted diffusion process. When rafting kinetics were increased, directional coarsening was completed in less time, and in response, the plateau in mean raft length was observed earlier. This plateau was generally obtained with the first 20 pct. of the specimen creep life.

The activation energy for rafting was estimated at a constant stress level. Its value at 179 MPa ($Q_{raft} \cong 381$ kJ/mol) was found to be reasonably close to the apparent activation energy for creep ($Q = 475 \pm 109$ kJ/mol). This implies that similar factors were controlling the temperature dependence of creep and directional coarsening.

Tensile Behavior

Tensile properties were determined in order to characterize the Ni-Al-Mo-Ta alloy more fully and to see if directional coarsening would occur under more rapid strain rates. Similar shapes of engineering stress-strain curves have been obtained at elevated temperatures in other single crystals. For example, negative slopes have been observed in the stress-strain curves of nickel-base superalloy single crystals (32, 158) and in single crystals of Ni_3Al (159) and Ni_3 (Al, X), where X was either Ti or W (160, 161). These same features have also been observed in compression

for nickel-base superalloy single crystals and columnar grained structures (162). The shape of these curves has been attributed to the yield point phenomenon and subsequent work softening (32, 160) due to dynamic recovery (32), although the negative slope has also been explained by pronounced necking in some single crystals (159).

The specimens which had been run to failure during creep testing and during tensile testing at 982^{o}C in the present study underwent similar amounts of total elongation. However, extensive directional coarsening had not developed in the specimens which were tensile tested. Since the tensile tests were completed after only 0.3 hours at the strain rates utilized, it was apparent that directional coarsening did not develop, because there was not sufficient time for diffusion to occur. This lends further support to the idea that strain plus time are necessary to develop extensive directional coarsening of γ'.

It was also shown that the γ-γ' lamellae stabilized during creep at a thickness which remained constant, at least up through the onset of tertiary creep. It was apparent that a limit had been reached in the material, where time plus a substantially higher amount of strain were necessary to alter the fine lamellar structure. This idea is supported further by the microstructure which was obtained after tensile testing was performed on a pre-rafted specimen; this microstructure after tensile testing was the same as that in the pre-rafted condition prior to tensile testing.

It appears that although a large amount of strain caused lamellar thickening in 20 hours of tertiary creep, thickening did not result after the same amount of strain was produced during tensile testing in only 0.3 hours. Thus, the finely-spaced rafted structure is stable, and accumulated strain plus time are necessary in order to alter it.

Finally, it has been suggested (81, 82) that rafting improves the creep properties by preventing dislocation climb, which is the dominant deformation mechanism in nickel-base superalloys at low strain rates and elevated temperatures (31, 32, 106). However, shearing of the γ' phase predominates in tensile testing conditions of high strain rates and elevated temperatures (106, 159).

As shown in Figure 51, the pre-rafted specimen had a lower UTS in comparison to that of the as-solutioned specimen. This difference may have been the result of the deformation mechanism operative under this high strain rate. The as-solutioned Ni-Al-Mo-Ta alloy may have had a higher UTS, because the γ' particles remained discrete, and as a result, the microstructure contained a larger number of γ-γ' interfaces. More interfaces would be intersected by mobile dislocations along {111} planes in the as-solutioned material, since in the pre-rafted material, the γ-γ' interfaces parallel to the applied stress were eliminated. Thus, it is possible that directionally coarsened structures may not be beneficial if particle shearing is normally the dominant deformation mechanism.

Zero-Stress Aging Behavior

The aging studies showed that the γ' precipitate size had stabilized very rapidly at 982°C. This stabilization against coarsening seemed to be related to the loss of precipitate coherency, as evidenced by the specimen on the plateau which had developed dense networks of misfit dislocations at the γ-γ' interfaces. A plateau in mean particle size has also been observed in aging studies of other alloys (163, 164). It has been suggested that the $t^{1/3}$ growth law is obeyed when the growing particles are coherent with the matrix, but that a saturation in particle size occurs after the loss of coherency (163).

The above mentioned observations are not consistent with those of Nicholson (76), who found that the γ' coarsening rate in Nimonic 80A increased after the loss of coherency had occurred. This was attributed (76) to an additional driving force, which is caused by the increase in interfacial energy associated with the formation of the misfit dislocations. Thus, it seems that the coarsening behavior of the present alloy is influenced by another factor, since the loss of coherency during aging at 982°C was correlated with a reduction in coarsening rate to nearly zero. It is suggested here that the stabilization of γ' size in this high misfit alloy may be related to the hypothesis (156, 165) that semi-coherent interfaces have a tendency to be immobile. That is, the dense misfit dislocation networks may be reducing the mobility of the γ-γ' interfaces, thereby decreasing the γ' coarsening rate.

The aging behavior of the present alloy at 1038°C was more puzzling, however. For example, the γ' particles continued to coarsen for some time after coherency had been lost; coherency loss was observed after 45 hours of aging, whereas the plateau in mean particle size was obtained after about 450 hours. Coarsening may have continued because the interfacial networks were more mobile at the higher temperature.

Nevertheless, the γ' coarsening rate in this high misfit alloy at 1038°C was lower than those of more conventional superalloys, such as Udimet 700 (64) and NASAIR 100 (75). Another possible explanation for this behavior could involve Mo saturation in the matrix, which is accompanied by short range ordering effects that could reduce the diffusivity of Al atoms in the matrix (11, 17). Despite the uncertainty in the explanation for this stabilization, the observation of a plateau in γ' particle growth is very significant. This inherent resistance to γ' coarsening is a very desirable feature and warrants further investigation.

Initial Microstructural Effects

A range of γ' sizes, as well as a range of coherency loss, was produced in single crystal specimens of the Ni-Al-Mo-Ta alloy by varying the quench rate from the homogenization temperature to ambient temperature. It was apparent that as particle growth progressed during the slower air quench, the γ' precipitates had a tendency to lose coherency.

This loss of coherency took place rapidly, and as a result, it is suggested that misfit dislocations may be nucleated by prismatic punching, a mechanism which was described earlier. The lattice mismatch of this alloy was relatively large in magnitude, although it did not exceed the value of the critical misfit that has been calculated for prismatic punching for a spherical precipitate in an infinite matrix at 930^{o}C (35, 88). However, it is clear that the assumptions used to make these predictions of critical misfit do not apply to high volume fraction superalloys. Furthermore, the interactions of the stress fields of closely-spaced γ' precipitates may cause stress concentrations in the material, such that the stress criterion for this mechanism is satisfied. Then, particles of a critical size could nucleate misfit dislocations by this punching mechanism.

Prismatic punching may also help to explain the rapid increase in creep strain which occurred for the oil quenched crystals during primary creep. As shown in Figure 66, the rafting process was rapid for the crystals in this initial condition. The γ' particles were coherent and had no misfit dislocations prior to testing. Perhaps as the γ' particles linked together, they reached a critical size whereby the mismatch could not be accommodated elastically. If misfit dislocations were nucleated at the γ-γ' interfaces by the punching mechanism, dislocation loops of opposite sign would be expelled into the matrix (35). These loops could contribute to the rapid rise in creep strain which was ob-

served for these oil quenched specimens.

The loss of coherency could also occur by the attraction of matrix dislocations from another source in the material, such as from the sub-boundaries. However, since most of the γ' particles were so remote with respect to these sub-boundaries, it seem unlikely that dislocations could be attracted so quickly across these large distances. This capture mechanism is generally regarded as a slow process (35), unless the supply of matrix dislocations is augmented by plastic deformation during mechanical testing.

It was found that the initial microstructures produced prior to creep testing had a significant effect on the subsequent creep properties. The increase in creep life achieved as a result of a more rapid quench from the homogenization temperature was not initially anticipated. On the other hand, the pre-aging treatment increased the initial γ' size and reduced the creep life by a factor of two. This result was not too surprising, because it has been demonstrated that coarse γ', caused by overaging, degrades creep properties in polycrystalline materials (66, 166). In addition, it has been shown (81, 82) that an aging treatment which simulates a typical coating cycle for turbine blades reduces the creep life in a similar Ni-Al-Mo-Ta alloy. The microstructure of this aged specimen had directionally coarsened, although the rafts were coarse and not very extensive nor developed. In contrast, the rafted structure produced in the pre-aged specimens in the

present investigation was coarser than that in the air quenched specimens, but was continuous and fully developed, as evidenced in Figure 63b. This is a subtle difference between the simulated coating cycle in references 81 and 82 and the 982^{o}C aging treatment in the present study. Thus, the effects of the pre-aging treatment in the present alloy cannot be attributed to the lack of fully developed rafts, as was the case for the simulated coating cycle.

The initial microstructures prior to testing also drastically affected the subsequent rafting kinetics. The γ' particles in the oil quenched specimens linked together at a rate which was about ten times faster than that of the aged or air quenched specimens. The closely-spaced γ' particles in the oil quenched crystals tended to be aligned along cube directions. This precipitate distribution and spacing may have hastened the development of the rafts, because the distance for diffusion was reduced. In addition, the rafting kinetics may be influenced by misfit dislocations present prior to testing. Since one of the driving forces for directional coarsening is the reduction in elastic strain energy (108), the presence of misfit dislocations can reduce the rate at which the rafts form by consuming the elastic coherency strains. This would reduce the driving force for rafting, and may have had some effect in the aged and air quenched single crystals which contained misfit dislocations prior to testing. A sufficient driving force was still present, however, apparently from

the modulus mismatch and reduction in surface area per unit volume, since the rafts in these crystals did eventually form, although at a slower rate.

The disparity in rafting rates between the different starting microstructures may have contributed somewhat to the differences in creep properties. However, the air quenched and aged specimens exhibited similar rafting rates, and yet their creep lives were significantly different. The reason for such differences in properties seems to be related to the γ-γ' interfacial area per unit volume of material. For a specific γ' volume fraction, a large number of interfaces are present with a finer γ' raft thickness, which can be produced by a refinement of the initial γ' size. Since it is believed that the misfit dislocation networks at the γ-γ' interfaces provide an effective impedance to matrix dislocation motion (81, 82), a larger number of interfaces per unit volume should reduce the creep deformation rate and improve creep properties. Figure 76 shows the microstructures of the aged, air quenched, and oil quenched single crystals after 50 hours of testing at 982^{o}C and 234 MPa. Comparison of these micrographs with the creep curves in Figure 60 shows that the properties improved substantially as the raft thickness decreased and the number of γ-γ' interfaces increased.

A very recent study of single crystals of another Ni-base superalloy, CMSX-2, has shown that a two-fold increase in creep life was attained when the γ' size was increased from about 0.30

μm to 0.45 μm (167). This is in direct contrast to the results of the present study in which γ' refinement improved creep properties. It was shown in CMSX-2 that as the γ' size was increased to 0.45 μm, the particles became aligned along cube directions. It was reported that the improvement in creep life occurred, because slightly more regular γ-γ' lamellae developed in the crystals containing the larger γ' particles. The difference in the magnitude of the mismatch between CMSX-2 and the Ni-Al-Mo-Ta alloy is a likely source for the different creep response observed as a function of initial γ' size. The delay in the changes of particle morphology, as well as particle alignment, which occurs during precipitate coarsening, is probably related to the lower misfit of the CMSX-2 alloy.

Third Phase Precipitation

The extracted residue of the third phase had a composition which was very close to that reported in the literature (135) for the $Ni_{47}Mo_{53}$ δ phase. Emission spectroscopy also detected trace amounts of Ta and Al in the residue, which could have resulted from contamination of the extracted phase by undissolved γ' or γ.

When the δ precipitates were first observed after short elevated temperature exposures, no envelope of γ' had formed around the δ phase. As the exposure time increased and the δ needles coarsened, γ' envelopes developed, presumably as Al and Ta were

rejected (168), while δ consumed the Mo and Ni from the matrix. Thus, one effect of δ may have been to deplete the matrix (2) of Mo. However, the major effect of this third phase seems to have been the interruptions that it caused within the lamellar structure. Discontinuities, such as those depicted in Figure 71a, appeared to provide paths for mobile dislocations to circumvent the γ-γ' interfaces, thereby reducing the effectiveness of the lamellar structure. As a result, the full potential of the rafted structure could not be attained with the composition of Alloy 1, even with the refinement of the initial γ' size.

Thus, a second single crystal composition with a slightly lower Mo content was obtained, in order to examine a similar alloy which did not contain δ. There were also small differences in the Al and Ta contents in this second alloy, which may have changed the solubility of Mo in the matrix. However, these effects appear to have been second-order with respect to that of the Mo content.

The creep life tripled in the air quenched condition when the precipitation of δ was essentially eliminated by a reduction in Mo of only 0.73 wt. pct. The creep lives of single crystals with this lower Mo composition were increased by an additional factor of two, when the γ' size was refined prior to creep testing by an oil quench from the homogenization temperature. Thus, slight compositional modifications brought about significant improvements in the creep properties of an alloy near saturation. Further improvements could be achieved in a specific alloy by changes in the

initial microstructure produced prior to testing.

CONCLUSIONS

Directional coarsening of the γ' particles began in this highly negative misfit alloy during primary creep at temperatures between 982 and 1038^{o}C. The length of the γ' rafts increased linearly with time up to a plateau, which under certain conditions was reached after the onset of steady-state creep. The thickness of the rafts remained constant from the start of the creep test up through at least the onset of tertiary creep. The interlamellar spacing followed a behavior similar to that of the raft thickness data as a function of time; this was a clear indication of the stability of this continuous and finely-spaced directionally coarsened structure. Accumulated strain plus time were necessary to alter the fine γ-γ' lamellae.

Gamma prime sizes ranging from 0.15 to 0.44 μm were produced in different single crystal specimens prior to creep testing by changing the quench rate from the homogenization temperature or by subsequent aging treatments. Oil quenching produced the finest γ' precipitates, and these particles were fully coherent with the γ matrix prior to creep testing. The rafts in the oil quenched crystals developed at a rate which was ten times higher than that of the aged or air quenched crystals. The aligned and closely-

spaced γ' particles in the oil quenched condition may have hastened the development of the rafts, because the distance for diffusion was reduced. The rafting kinetics also appeared to be influenced by the misfit dislocations present in the aged and oil quenched crystals prior to testing. Misfit dislocations consumed the elastic coherency strains, thereby decreasing the rate at which the rafts formed, by reducing the driving force for rafting.

The thickness of the rafts which formed was equal to the initial γ' size, since the γ' particles linked together rapidly without thickening. The single crystals with the finest γ' size exhibited the longest creep lives, because the rafts which formed had a larger γ-γ' interfacial area per unit volume. A large number of interfaces would provide additional barriers to matrix dislocation motion, thereby improving the creep resistance of the material.

Reducing the Mo content in this alloy by only 0.73 wt. pct. improved the creep life by a factor of three in the baseline condition, because the precipitation of a third phase which caused localized interruptions in the lamellar structure was eliminated. The creep lives of single crystals with this lower Mo composition were increased by an additional factor of two, when the γ' size was refined prior to creep testing by an oil quench from the homogenization temperature. Thus, slight compositional modifications brought about substantial improvements in the creep properties of an alloy near saturation. Furthermore, the directionally

coarsened structure and the resulting creep properties could be altered significantly in a specific alloy by changes in the initial microstructure produced prior to testing. It is hoped that this study may assist in the understanding and optimization of this unique microstructure in advanced single crystal turbine blade alloys.

REFERENCES

(1) R. F. Decker: in Proc. of Steel Strengthening Mechanisms Symp., p. 1-23, Zurich, May 5-6, 1969.

(2) R. F. Decker and C. T. Sims: in The Superalloys, C. T. Sims and W. C. Hagel, eds., p. 33, John Wiley and Sons, New York, 1972.

(3) D. R. Muzyka: in The Superalloys, C. T. Sims and W. C. Hagel, eds., p. 113, John Wiley and Sons, New York, 1972.

(4) P. R. Okamoto and G. Thomas: Acta Met., 1971, vol. 19, pp. 825-841.

(5) G. van Tendeloo, R. DeRidder, and S. Amelinckx: Phys. Stat. Sol., 1975, vol. 27(a), pp. 457-468.

(6) M. M. Kersker, E. A. Aigeltinger, and J. J. Hren: in Proc. 38th Annual EMSA Meeting, G. W. Bailey, ed., p. 158, Claitor's Publishing Division, Baton Rouge, 1980.

(7) D. B. Snow: in Proc. 38th Annual EMSA Meeting, G. W. Bailey, ed., p. 334, Claitor's Publishing Division, Baton Rouge, 1980.

(8) M. V. Nathal and L. J. Ebert: to be published in Proc. Fifth Int'l Symp. on Superalloys, M. Gell et al., eds., AIME, 1984.

(9) J. R. Mihalisin and D. L. Pasquine: in Proc. Int'l Symp. on Structural Stability in Superalloys, p. 131, Vol. I, Seven Springs, PA, 1968.

(10) O. H. Kriege and J. M. Baris: Trans. ASM, 1969, vol. 62, pp. 195-200.

(11) W. T. Loomis, J. W. Freeman, and D. L. Sponseller: Met. Trans., 1972, vol. 3, pp. 989-1000.

(12) R. M. N. Pelloux and N. J. Grant: Trans. AIME, 1960, vol. 218, pp. 232-237.

(13) E. R. Parker and T. H. Hazlett: in Relation of Properties to Microstructure, p. 30, ASM, 1954.

(14) N. S. Stoloff: in The Superalloys, C. T. Sims and W. C. Hagel, eds., p. 79, John Wiley and Sons, New York, 1972.

(15) R. Nordheim and N. J. Grant: J. Inst. Met., 1954, vol. 82, pp. 440-444.

(16) T. C. Tiearney, Jr., and N. J. Grant: Met. Trans., 1982, vol. 13A, pp. 1827-1836.

(17) E. Aigeltinger and M. Kersker: Metals Forum, 1981, vol. 4, pp. 112-116.

(18) C. R. Brooks: in Heat Treatment, Structure, and Properties of Nonferrous Alloys, p. 139, ASM, Metals Park, Ohio, 1982.

(19) L. M. Brown and R. K. Ham: in Strengthening Methods in Crystals, A. Kelly and R. B. Nicholson, eds., p. 62, John Wiley and Sons, New York, 1971.

(20) C. Lall, S. Chin, and D. P. Pope: Met. Trans., 1979, vol. 10A, pp. 1323-1332.

(21) V. A. Phillips: Phil. Mag., 1967, vol. 16, pp. 103-117.

(22) R. Nordheim and N. J. Grant: J. Metals, 1954, pp. 211-218.

(23) J. R. Mihalisin and R. F. Decker: Trans. AIME, 1960, vol. 218, pp. 507-515.

(24) R. F. Decker and J. R. Mihalisin: Trans. ASM, 1969, vol. 62, pp. 481-489.

(25) R. G. Davies and T. L. Johnston: in Proc. Third Landing Conf. on Ordered Alloys, B. H. Kear, et al., eds., p. 447, Claitors Publishing Division, Baton Rouge, 1970.

(26) R. F. Decker and R. R. DeWitt: J. Metals, 1965, vol. 17, pp. 139-145.

(27) B. J. Piearcey, B. H. Kear, and R. W. Smashey: Trans. ASM, 1967, vol. 60, pp. 634-645.

(28) B. J. Piearcey and B. E. Terkelsen: Trans. AIME, 1967, vol. 239, pp. 1143-1150.

(29) J. J. Jackson, M. J. Donachie, R. J. Henricks, and M. Gell: Met. Trans., 1977, vol. 8A, pp. 1615-1620.

(30) W. C. Hagel and H. J. Beattie: in Precipitation Processes in Steels, p. 98, Iron and Steel Inst. Special Report No. 64, London, 1959.

(31) C. Carry and J. L. Strudel: Acta Met., 1977, vol. 25, pp. 767-777.

(32) C. Carry and J. L. Strudel: Acta Met., 1978, vol. 26, pp. 859-870.

(33) N. F. Mott and F. R. N. Nabarro: Proc. Phys. Soc., 1940, vol. 52, pp. 86-89.

(34) G. R. Woolhouse and L. M. Brown: J. Inst. Met., 1970, vol. 98, pp. 106-110.

(35) G. C. Weatherly and R. B. Nicholson: Phil. Mag., 1968, vol. 17, pp. 801-831.

(36) D. A. Grose and G. S. Ansell: Met. Trans., 1981, vol. 12A, pp. 1631-1645.

(37) T. B. Gibbons and B. E. Hopkins: Met. Sci. J., 1971, vol. 5, pp. 233-240.

(38) G. N. Maniar, J. E. Bridge, Jr., H. M. James, and G. B. Heydt: Met. Trans., 1970, vol. 1, pp. 31-42.

(39) V. A. Phillips: Scripta Met., 1968, vol. 2, pp. 147-151.

(40) D. Raynor and J. M. Silcock: Met. Sci. J., 1970, vol. 4, pp. 121-130.

(41) R. F. Miller and G. S. Ansell: Met. Trans., 1977, vol. 8A, pp. 1979-1991.

(42) O. H. Kriege and C. P. Sullivan: Trans. ASM, 1968, vol. 61, pp. 278-282.

(43) A. J. Ardell, R. B. Nicholson, and J. D. Eshelby: Acta Met., 1966, vol. 14, pp. 1295-1309.

(44) E. Hornbogen and M. Roth: Z. Metallk., 1967, vol. 58, pp. 842-855.

(45) B. A. Parker and D. R. F. West: Aust. Inst. of Metals, 1969, vol. 14, pp. 102-110.

(46) A. Havalda: Trans. ASM, 1969, pp. 477-480.

(47) H. F. Merrick: in Precipitation Processes in Solids, K. C. Russell and H. I. Aaronson, eds., p. 161, TMS-AIME, New York, 1978.

(48) C. K. L. Davies, P. Nash, and R. N. Stevens: J. Mat. Sci., 1980, vol. 15, pp. 1521-1532.

(49) R. C. Ecob, R. A. Ricks, and A. J. Porter: Scripta Met., 1982, vol. 16, pp. 1085-1090.

(50) I. M. Lifshitz and V. V. Slyozov: J. Phys. Chem. Solids, 1961, vol. 19, pp. 35-50.

(51) C. Wagner: Z. Elektrochem., 1961, vol. 65, pp. 581-591.

(52) G. W. Greenwood: Acta Met., 1956, vol. 4, pp. 243-248.

(53) A. J. Ardell: in Proc. Int'l Symp. on Mechanism of Phase Transformation in Crystalline Solids, p. 111, Inst. of Metals Monograph and Rept. Series 33, 1968.

(54) A. J. Ardell and R. B. Nicholson: J. Phys. Chem. Solids, 1966, vol. 27, pp. 1793-1804.

(55) A. J. Ardell: Acta Met., 1968, vol. 16, pp. 511-516.

(56) A. J. Ardell: Met. Trans., 1970, vol. 1, pp. 525-534.

(57) P. K. Rastogi and A. J. Ardell: Acta Met., 1971,. vol. 19, pp. 321-330.

(58) A. J. Ardell: Acta Met., 1967, vol. 15, pp. 1772-1775.

(59) R. A. Swalin and A. Martin: J. Metals, 1956, vol. 206, pp. 567-572.

(60) A. J. Ardell: Acta Met., 1972, vol. 20, pp. 61-71.

(61) J. D. Livingston: Trans. AIME, 1959, vol. 215, pp. 566-571.

(62) D. J. Chellman and A. J. Ardell: Acta Met., 1971, vol. 22, pp. 577-588.

(63) W. I. Mitchell: Z. Metallk., 1964, vol. 55, pp. 613-616.

(64) E. H. Van der Molen, J. M. Oblak, O. H. Kriege: Met. Trans., 1971, vol. 2, pp. 1627-1633.

(65) C. H. White: in The Nimonic Alloys, W. Betteridge and J. Heslop, eds., p. 63, Crane Russak and Co., Inc., New York, 1974.

(66) R. A. Stevens and P. E. J. Flewitt: Mat. Sci. Eng., 1979, vol. 37, pp. 237-247.

(67) C. K. L. Davies, P. Nash, and R. N. Stevens: Acta Met., 1980, vol. 28, pp. 179-189.

(68) A. D. Brailsford and P. Wynblatt: Acta Met., 1979, vol. 27, pp. 489-497.

(69) A. J. Porter, R. A. Ricks, and R. C. Ecob: J. Mat. Sci., 1983, vol. 18, pp. 1895-1896.

(70) R. D. Doherty: Met. Sci. J., 1982, vol. 16, pp. 1-13.

(71) V. Biss and D. L. Sponseller: Met. Trans., 1973, vol. 4, pp. 1953-1960.

(72) P. Nash: Ph.D. Thesis, London, 1977.

(73) B. Bergman: Scand. J. Metallurgy, 1975, vol. 4, pp. 97-108.

(74) E. A. Fell: Metallurgia, 1961, vol. 63, p. 157-166.

(75) M. V. Nathal: Ph.D. Thesis, Case Western Reserve University, Cleveland, OH, 1983.

(76) R. B. Nicholson: in Interfaces Conf., R. C. Gifkins, ed., p. 139, Aust. Inst. Metals, Melbourne, 1969.

(77) J. W. Martin and R. D. Doherty: in Stability of Microstructure in Metallic Systems, p. 154, Cambridge University Press, Cambridge, 1976.

(78) F. C. Frank and J. H. Van Der Merwe: Proc. R. Soc. A, 1950, vol. 201, pp. 261-268.

(79) P. K. Rastogi: J. App. Phys., 1970, vol. 41, pp. 4243-4244.

(80) A. Lasalmonie and J. L. Strudel: Phil. Mag., 1975, vol. 32, pp. 937-949.

(81) D. D. Pearson, F. D. Lemkey, and B. H. Kear: in Proc. Fourth Int'l Symp. on Superalloys, J. K. Tien, et al., p. 513, ASM, Metals Park, OH, 1980.

(82) D. D. Pearson, B. H. Kear, and F. D. Lemkey: in Creep and Fracture of Engineering Materials and Structures, B. Wilshire and D. R. J. Owens, eds., p. 213, Pineridge Press Ltd., Swansea, U. K., 1981.

(83) R. A. MacKay and L. J. Ebert: to be published in Proc. Fifth Int'l Symp. on Superalloys, M. Gell, et al., eds., AIME, 1984.

(84) H. Brooks: in Metal Interfaces, p. 20, ASM, Cleveland, 1952.

(85) J. W. Matthews: in Dislocations in Solids, F. R. N. Nabarro, ed., p. 463, North-Holland Publishing Company, Amsterdam, 1979.

(86) J. Friedel: in Dislocations, p. 371, Pergamon Press, New York, 1964.

(87) L. M. Brown, G. R. Woolhouse and U. Valdre: Phil. Mag., 1968, vol. 17, pp. 781-789.

(88) G. C. Weatherly: Phil. Mag., 1968, vol. 17, pp. 791-799.

(89) A. J. Ardell: Phil. Mag., 1967, vol. 16, pp. 147-158.

(90) R. S. Barnes and D. J. Mazey: Acta Met., 1964, vol. 11, pp. 281-286.

(91) R. G. Baker, D. G. Brandon, and J. Nutting: Phil. Mag., 1959, vol. 4, pp. 1339-1345.

(92) G. A. Webster and C. P. Sullivan: J. Inst. Metals, 1967, vol. 95, pp. 138-142.

(93) G. A. Webster and B. J. Piearcey: Met. Sci. J., 1967, vol. 1, pp. 97-104.

(94) C. P. Sullivan, G. A. Webster, and B. J. Piearcey: J. Inst. Metals, 1968, vol. 96, pp. 274-281.

(95) W. Danesi and M. Donachie: J. Inst. Metals, 1969, vol. 97, pp. 107-111.

(96) J. P. Dennison, P. D. Holmes, and B. Wilshire: Mat. Sci. Eng., 1978, vol. 33, pp. 35-47.

(97) H. Burt, J. P. Dennison, I. C. Elliot, and B. Wilshire: Mat. Sci. Eng., 1982, vol. 53, pp. 245-250.

(98) I. L. Mirkin and O. D. Kancheev: Met. Sci. Heat Treatment, 1967, vol. 1, pp. 10-13.

(99) J. K. Tien and S. M. Copley: Met. Trans., 1971, vol. 2, pp. 215-219.

(100) J. K. Tien and S. M. Copley: Met. Trans., 1971, vol. 2, pp. 543-553.

(101) J. K. Tien and R. P. Gamble: Met. Trans., 1972, vol. 3, pp. 2157-2162.

(102) C. Carry and J. L. Strudel: in Proc. Fourth Int'l Conf. on the Strength of Metals and Alloys, Laboratoire de Physique du Solide, ed., p. 324, Nancy, France, vol. 1, 1976.

(103) C. Carry, S. Dermarkar, J. L. Strudel, and B. C. Wonsiewicz: Met. Trans., 1979, vol. 10A, pp. 855-860.

(104) M. V. Nathal and L. J. Ebert: Scripta Met., 1983, vol. 17, pp. 1151-1154.

(105) R. A. MacKay and L. J. Ebert: Scripta Met., 1983, vol. 17, pp. 1217-1222.

(106) G. R. Leverant, B. H. Kear, and J. M. Oblak: Met. Trans., vol. 4, pp. 355-362.

(107) D. H. Maxwell: U. S. Patent 3,617,397, November 2, 1971.

(108) A. Pineau: Acta Met., 1976, vol. 24, pp. 559-564.

(109) J. D. Eshelby: Proc R. Soc. A, 1957, vol. 241, pp. 376-396.

(110) J. D. Eshelby: Prog. Solid. Mech., I. N. Sneddon and R. Hill, eds., 1961, vol. 2, pp. 89-140.

(111) T. Miyazaki, K. Nakamura, and H. Mori: J. Mat. Sci., 1979, vol. 14, pp. 1827-1837.

(112) R. G. Davies and N. S. Stoloff: Trans. AIME, 1965, vol. 233, pp. 714-719.

(113) P. E. Armstrong and H. L. Brown: Trans. AIME, 1964, vol. 230, pp. 962-966.

(114) G. N. Maniar and J. E. Bridge, Jr.: Met. Trans., 1971, vol. 2, pp. 95-102.

(115) C. C. Law and M. J. Blackburn: Met. Trans., 1980, vol. 11A, pp. 495-507.

(116) M. J. Donachie, Jr., and O. H. Kriege: J. Mat., 1972, vol. 7, no. 3, pp. 269-278.

(117) Z. Lashko: Joint Publications Research Service 56746, 1972.

(118) C. B. Shoemaker, A. H. Fox, and D. P. Shoemaker: Acta Cryst., 1960, vol. 13, pp. 585-587.

(119) J. M. Walsh and M. J. Donachie, Jr.: Met. Trans., 1973, vol. 4, pp. 2854-2855.

(120) M. C. Flemings: in Solidification Processing, p. 330, McGraw-Hill, Inc., New York, 1974.

(121) A. F. Giamei, E. H. Kraft, and F. D. Lemkey: in New Trends in Materials Processing, C. S. Hartley, ed., p. 48, ASM, Metals Park, OH, 1976.

(122) T. Z. Kattamis and J. C. Lecomte: J. Mater. Sci., 1978, vol. 13, pp. 2731-2736.

(123) R. A. MacKay: M.S. Thesis, Case Western Reserve University, Cleveland, OH, May 1981.

(124) R. A. MacKay and R. D. Maier: Met. Trans., 1982, vol. 13A, pp. 1747-1754.

(125) G. D. Merz, T. Z. Kattamis, and A. F. Giamei: J. Mater. Sci., 1979, vol. 14, pp. 663-670.

(126) P. L. Martin, H. A. Lipsitt, and J. C. Williams: in Rapid Solidification Processing: Principles and Technologies, II, R. Mehrabian, et al., eds., p. 123, Claitor's Publishing Division, Baton Rouge, 1980.

(127) C. E. Lowell, R. G. Garlick, and B. Henry: Met. Trans., 1976, vol. 7A, pp. 655-660.

(128) D. C. Montgomery and E. A. Peck: in Introduction to Linear Regression Analysis, p. 168, John Wiley and Sons, New York, 1982.

(129) D. F. Paulonis, J. M. Oblak, and D. S. Duvall: Trans. ASM, 1969, vol. 62, pp. 611-622.

(130) D. L. Anton and D. D. Pearson: Presented at 1983 TMS-AIME Fall Meeting, Philadelphia, PA.

(131) F. C. Monkman and N. J. Grant: in Deformation and Fracture at Elevated Temperatures, N. J. Grant and A. W, Mullendore, eds., p. 91, The M. I. T. Press, Cambridge, MA, 1965.

(132) S. D. Antolovich, P. Domas, and J. L. Strudel: Met. Trans., 1979, vol. 10A, pp. 1859-1868.

(133) G. Bergman and D. P. Shoemaker: Acta Cryst., 1954, vol. 7, pp. 857-865.

(134) C. B. Shoemaker and D. P. Shoemaker: Acta Cryst., 1963, vol. 16, pp. 997-1009.

(135) A. V. Virkar and A. Raman: Z. Metallk., 1969, Bd. 60, H. 7, pp. 594-600.

(136) P. Nash, S. Fielding, and D. R. F. West: Metal Sci. J., 1983, vol. 17, pp. 192-194.

(137) S. Chakravorty and D. R. F. West: Met. Sci. J., 1983, vol. 17, pp. 573-580

(138) D. B. Miracle, K. A. Lark, V. Srinivasan, and H. A. Lipsitt: Met. Trans., 1984, vol. 15A, pp. 481-486.

(139) F. C. Hull: Metals Progress, 1969, vol. 96, p. 139.

(140) R. A. Ricks, A. J. Porter, and R. C. Ecob: Acta Met., 1983, vol. 31, pp. 43-53.

(141) H. Morrow, D. L. Sponseller, and M. Semchyshen: Met. Trans., 1975, vol. 6A, pp. 477-485.

(142) M. P. Arbuzov and I. A. Zelenkov: Phys. Met. Metall., 1963, vol. 16, pp. 65-68.

(143) H. E. Evans and G. Knowles: Met. Sci. J., 1980, vol. 14, pp. 262-266.

(144) K. R. Williams and B. Wilshire: Met. Sci. J., 1973, vol. 7, pp. 176-179.

(145) T. G. Langdon: in Proc. Sixth Int'l Conf. Strength of Metals and Alloys, R. C. Gifkins, ed., p. 1105, Pergamon Press, Oxford, 1982.

(146) W. D. Nix and B. Ilschner: in Proc. Fifth Int'l Conf. Strength of Metals and Alloys, P. Hassen, et al., eds., p. 1503, Pergamon Press, Oxford, 1979.

(147) D. McLean: Rep. Progress Phys., 1966, vol. 29, pp. 1-29.

(148) R. W. Lund and W. D. Nix: Met. Trans., 1975, vol. 6A, pp. 1329-1333.

(149) R. A. Swalin, A. Martin, and R. Olson: Trans. AIME, 1957, vol. 209, pp. 936-939.

(150) C. R. Barrett and O. D. Sherby: Trans. AIME, 1965, vol. 233, pp. 1116-1119.

(151) M. McLean: in Directionally Solidified Materials for High Temperature Service, p. 176, The Metals Society, London, 1983.

(152) P. L. Threadgill and B. Wilshire: in Proc. of Iron and Steel Inst. Conf. on Creep Strength in Steel and High Temperature Alloys, p. 8, The Metals Society, London, 1974.

(153) C. N. Ahlquist and W. D. Nix: Acta Met., 1971, vol. 19, pp. 373-385.

(154) M. McLean: in Proc. Fourth Int'l Symp. on Superalloys, J. K. Tien, et al., eds., p. 661, ASM, Metals Park, OH, 1980.

(155) D. Schwahn, W. Kesternich, and H. Schuster: Met. Trans., 1981, vol. 12A, pp. 155-165.

(156) H. I. Aaronson, J. K. Lee, and K. C. Russell: in Precipitation Processes in Solids, K. C. Russell and H. I. Aaronson, eds., p. 31, TMS-AIME, New York, 1978.

(157) E. E. Underwood: in Quantitative Stereology, p. 48, Addison-Wesley Publishing Co., Reading, MA, 1970.

(158) B. H. Kear and B. J. Piearcey: Trans. AIME, 1967, vol. 239, pp. 1209-1215.

(159) S. M. Copley and B. H. Kear: Trans. AIME, 1967, vol. 239, pp. 977-984.

(160) K. Aoki and O. Izumi: J. Mat. Sci., 1979, vol. 14, pp. 1800-1806.

(161) T. Saburi, T. Hamana, S. Nenno, and H. Pak: Jap. J. Appl. Phys., 1977, vol. 16, no. 2, pp. 267-272.

(162) C. C. Law and A. F. Giamei: Met. Trans., 1976, vol. 7A, pp. 5-16.

(163) J. W. Martin and F. J. Humphreys: Scripta Met., 1974, vol. 8, pp. 679-680.

(164) P. K. Footner and B. P. Richards: J. Mat. Sci., 1982, vol. 17, pp. 2141-2153.

(165) H. I. Aaronson: in Decomposition of Austenite by Diffusional Processes, V. F. Zackay and H. I. Aaronson, eds., p.387, Interscience Publishers, New York, 1960.

(166) G. A. Webster and B. J. Piearcey: Trans. ASM, 1966, vol. 59, pp. 847-859.

(167) P. Caron and T. Khan: Mat. Sci. Eng., 1983, vol. 61, pp. 173-184.

(168) K. A. Williams, D. B. Miracle, and H. A. Lipsitt: in Rapid Solidification Processing: Principles and Technologies, II, R. Mehrabian et al., eds., p. 129, Claitor's Publishing Division, Baton Rouge, 1980.

TABLE I

CHEMICAL ANALYSES OF NICKEL-BASE SUPERALLOYS
USED IN THE PRESENT STUDY (WT. PCT.)

	ELEMENTS			
Alloy	Al	Mo	Ta	Ni
1	5.80	14.63	6.24	balance
2	6.05	13.90	5.85	balance

TABLE II

DIFFRACTOMETER SCAN DATA FOR Ni-Al-Mo-Ta
SINGLE CRYSTALS AT ROOM TEMPERATURE

Peak Used	$2\theta_{\gamma}(K_{\alpha})$	$2\theta_{\gamma'}(K_{\alpha 1})$	$2\theta_{\gamma'}(K_{\alpha 2})$	a_{γ}(Å)	$a_{\gamma'}$(Å)	δ(pct.)
(024)*	145.62	147.62	148.60	3.6057	3.5870	-0.5200
(024)	144.59	147.67	148.68	3.6159	3.5864	-0.8192
(024)	144.67	147.64	148.66	3.6151	3.5866	-0.7915
(012)	--	57.43	--	--	3.5848	--
(004)	116.90	118.43	118.90	3.6154	3.5864	-0.8053
(004)	116.96	118.44	118.91	3.6143	3.5863	-0.7777

* after homogenization only

TABLE III

HIGH TEMPERATURE X-RAY DIFFRACTION DATA
FOR [001]-ORIENTED Ni-Al-Mo-Ta SINGLE CRYSTALS

Temp.(°C)	$2\theta_\gamma(K_\alpha)$	$2\theta_{\gamma'}(K_{\alpha 1})$	$2\theta_{\gamma'}(K_{\alpha 2})$	a_γ(Å)	$a_{\gamma'}$(Å)	δ(pct.)
18.3	116.96	118.44	118.91	3.6143	3.5863	-0.7783
37.8	116.92	118.39	118.87	3.6150	3.5871	-0.7764
93.3	116.80	118.27	118.75	3.6174	3.5893	-0.7787
148.9	116.69	118.15	118.62	3.6195	3.5916	-0.7730
204.4	116.57	118.03	118.48	3.6219	3.5941	-0.7697
260.0	116.45	117.89	118.37	3.6242	3.5964	-0.7692
315.6	116.31	117.78	118.23	3.6270	3.5988	-0.7797
371.1	116.22	117.65	118.12	3.6287	3.6011	-0.7654
426.7	116.07	117.50	117.98	3.6317	3.6038	-0.7706
482.2	115.92	117.38	117.84	3.6347	3.6063	-0.7839
537.8	115.81	117.25	117.72	3.6368	3.6087	-0.7776
593.3	115.63	117.09	117.56	3.6404	3.6117	-0.7918
648.9	115.60	116.94	117.42	3.6410	3.6145	-0.7310
704.4	115.81	116.98	117.44	3.6368	3.6139	-0.6317
760.0	115.80	116.82	117.27	3.6370	3.6171	-0.5492
815.6	114.92	116.36	116.79	3.6548	3.6263	-0.7828
871.1	114.72	116.19	116.64	3.6588	3.6294	-0.8081
926.7	114.57	116.04	116.49	3.6619	3.6323	-0.8105

TABLE IV

PREDICTED LATTICE CONSTANTS AND LATTICE MISFIT

Temp.(°C)	a_γ(Å)	$a_{\gamma'}$(Å)	δ(pct.)
200.0	3.6214	3.5935	-0.7730
400.0	3.6304	3.6024	-0.7743
600.0	3.6411	3.6127	-0.7819
800.0	3.6535	3.6245	-0.7959
982.0	3.6663	3.6365	-0.8142
1038.0	3.6704	3.6404	-0.8209
1093.0	3.6747	3.6444	-0.8280

TABLE V

DIFFRACTOMETER SCAN DATA FOR Mo-RICH BCT PHASE
AT VARIOUS TEMPERATURES

Temp.(°C)	BCT Peak Used	2 θ	a (Å)	c (Å)*
760.0	(008)	114.65	3.5885	7.3205
18.3	(011)	27.50	3.6091	7.3625
704.4	(008)	114.50	3.5915	7.3267
704.4	(006)	78.45	3.2460	6.6219
732.2	(008)	114.36	3.5943	7.3325
760.0	(008)	114.67	3.5881	7.3197

* Obtained from assumption that c/a ~ 2.04 (ref. 129)

TABLE VI

KINETICS OF γ' RAFTING

Testing Conditions		Rafting Rate
Temp. (^{o}C)	Stress (MPa)	(μm/hr)
982	234	0.0156
982	186	0.0104
1038	179	0.0475
1038	147	0.0169

TABLE VII

RATE CONSTANTS k FOR γ' COARSENING IN VARIOUS MATERIALS AT 1038°C

Material	k ($\mu m^3/hr$)	Reference	Note
Ni-Al	7.50×10^{-4}	Ardell and Nicholson (43)	Extrapolated from 775°C
Udimet 700	2.44×10^{-4}	Van Der Molen et al. (64)	
NASAIR 100	2.10×10^{-4}	Nathal (75)	Extrapolated from 1000°C
Ni-Al-Mo-Ta	3.76×10^{-5}	present study	for cuboidal particles
Ni-Al-Mo-Ta	1.76×10^{-2}	present study	for rafts at 179 MPa
Ni-Al-Mo-Ta	6.67×10^{-3}	present study	for rafts at 147 MPa

TABLE VIII

CREEP DATA AT 982°C AND 234 MPa FOR VARIOUS STARTING γ' SIZES AND Mo CONTENTS

Tested Condition	γ' Size (μm)	Mo Level (wt. pct.)	Creep Life (hrs.)	$\dot{\epsilon}_s$ x 10^{-8} sec^{-1}
air quenched and aged	0.44	14.6	63.9	10.83
air quenched	0.33	14.6	120.0	3.17
oil quenched	0.15	14.6	189.1	1.64
air quenched	0.33	13.9	355.9	0.93
oil quenched	0.15	13.9	704.7	0.28

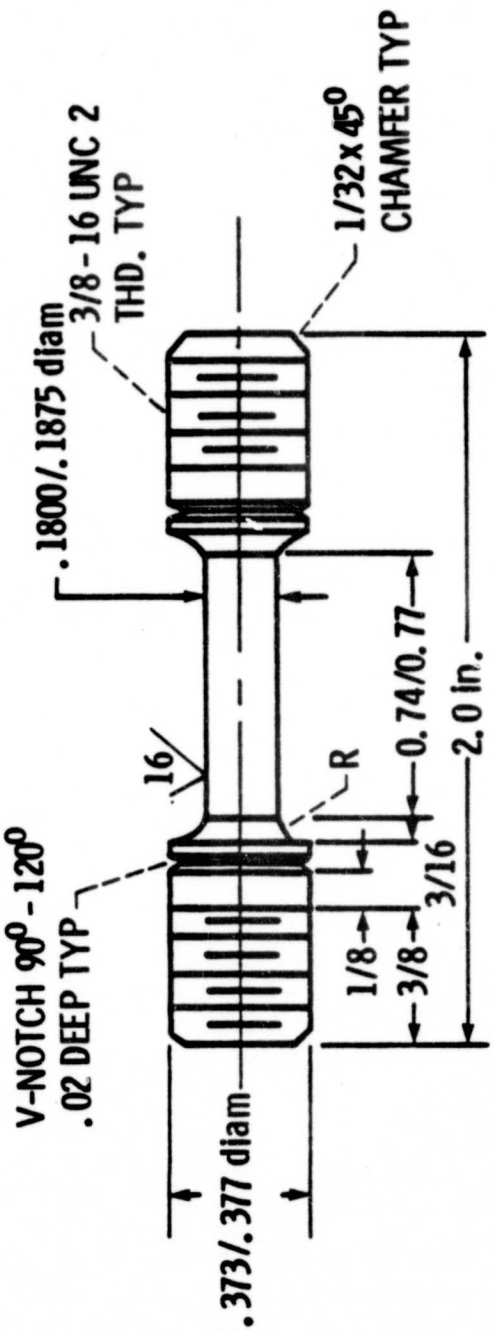

Figure 1. Specimen configuration which shows the locations of the circumferential v-notches for placement of the extensometer knife edges.

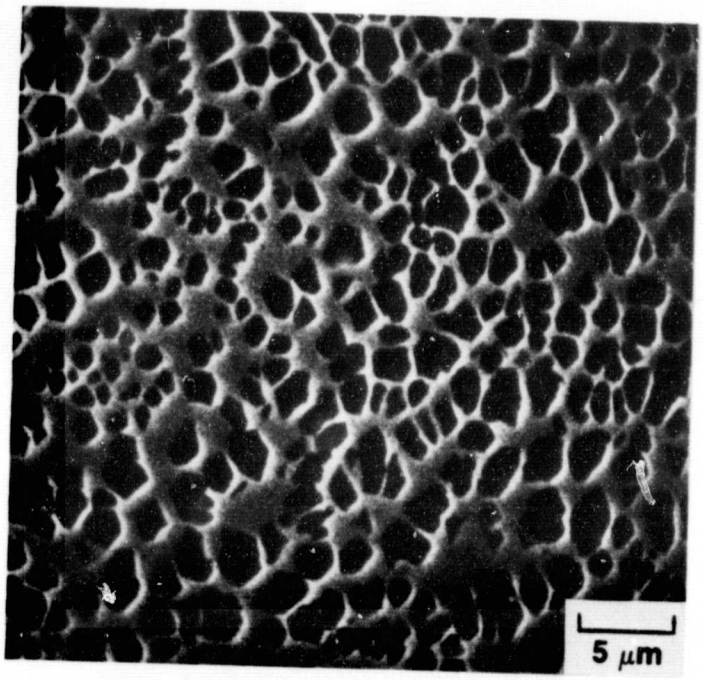

Figure 2. The γ-γ' microstructure of a Ni-Al-Mo-Ta single crystal is shown in the as-cast condition. The dark precipitate is the γ' phase.

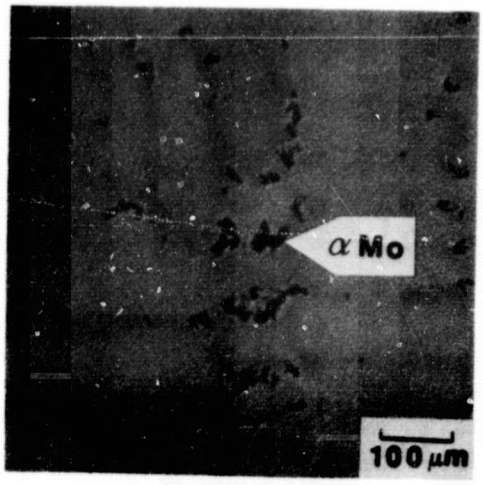

(a)

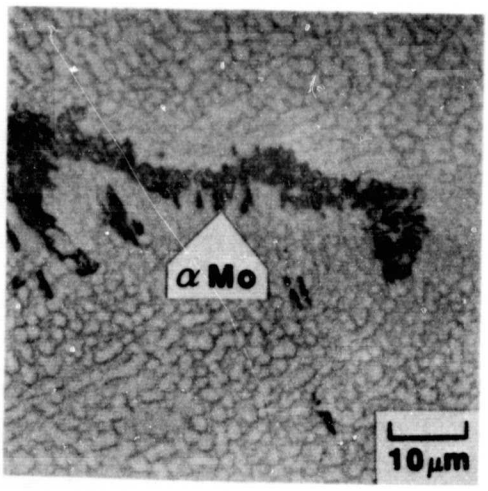

(b)

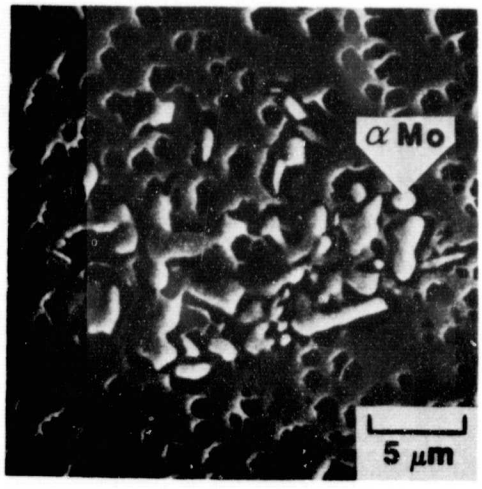

(c)

Figure 3. Interdendritic regions of a Ni-Al-Mo-Ta single crystal in the as-cast condition. α-Mo is depicted in (a) and (b) by optical microscopy and in (c) by SEM.

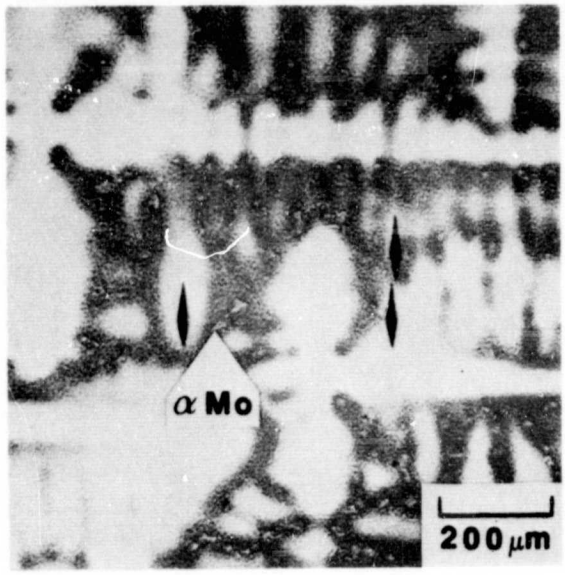

Figure 4. Microhardness indenter marks delineate area of as-cast specimen which was examined by microprobe. The results are shown in Figure 6.

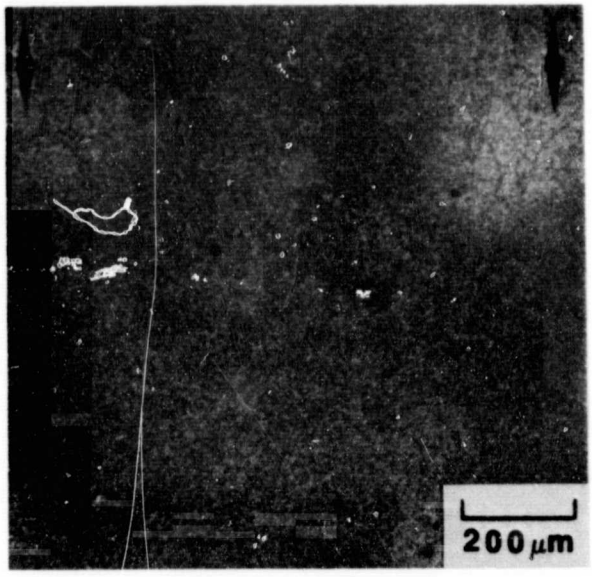

Figure 5. Microhardness indenter marks delineate area of homogenized specimen which was examined by microprobe. The results are shown in Figure 7.

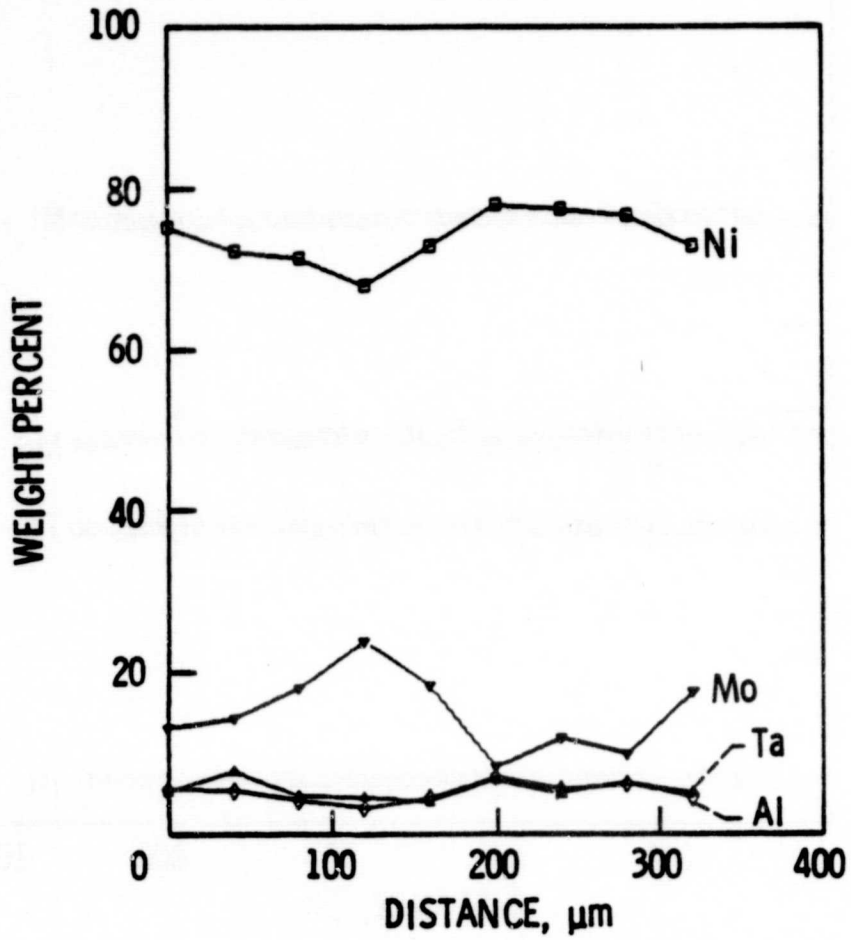

Figure 6. Microprobe results showing variation in element levels as a function of distance within the as-cast specimen illustrated in Figure 4.

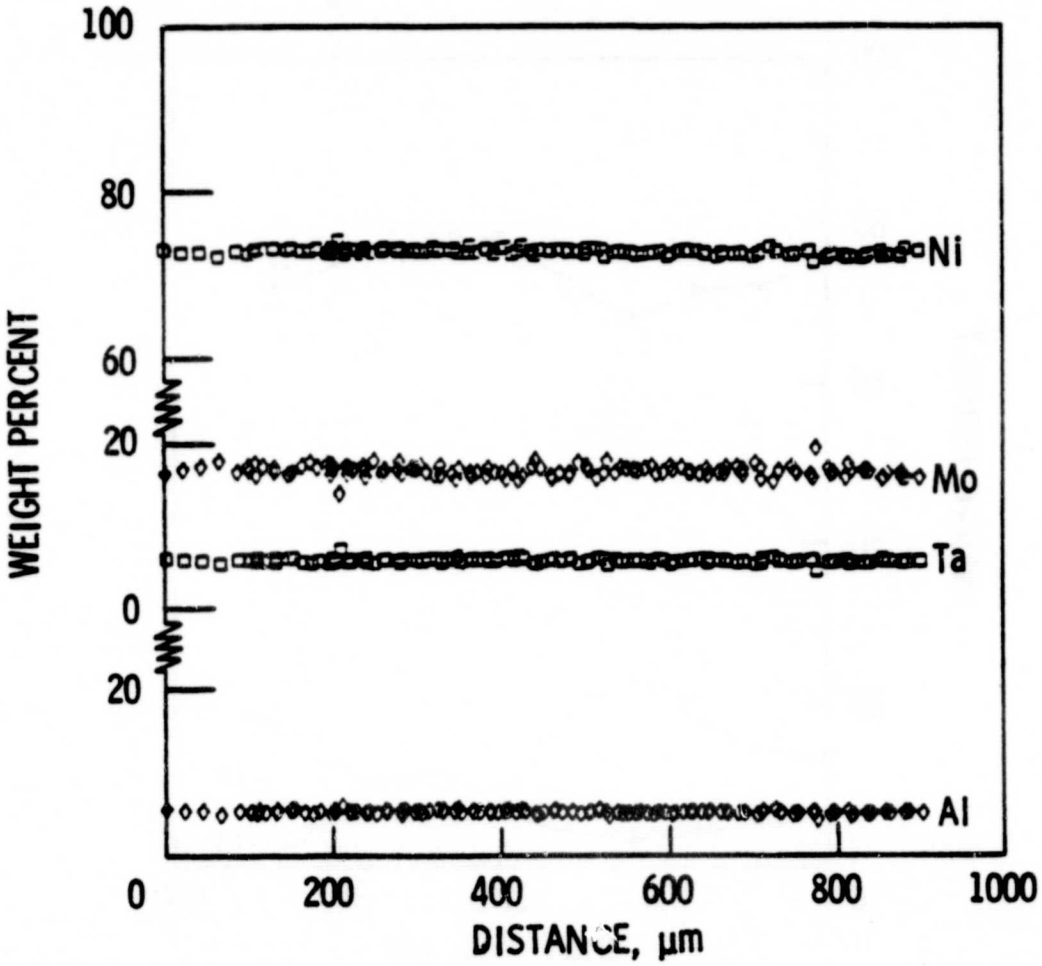

Figure 7. Microprobe results showing the constancy of the element levels as a function of distance within the homogenized specimen illustrated in Figure 5.

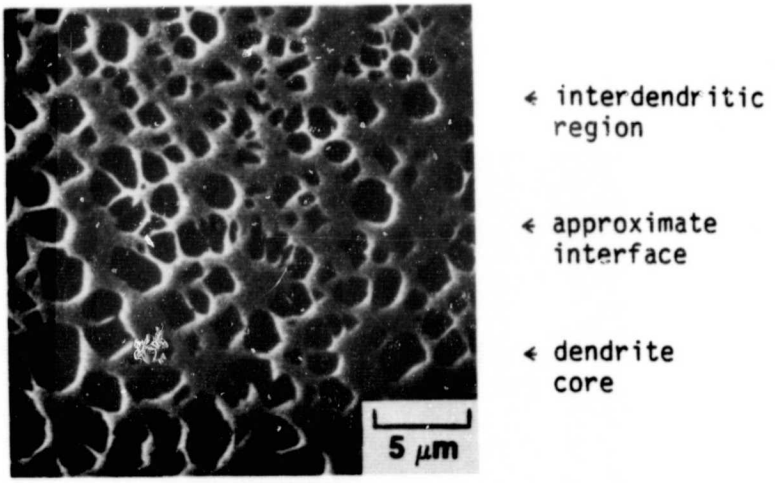

Figure 8. The change in γ' size which exists at the interface between a dendrite core and an interdendritic region in as-cast material.

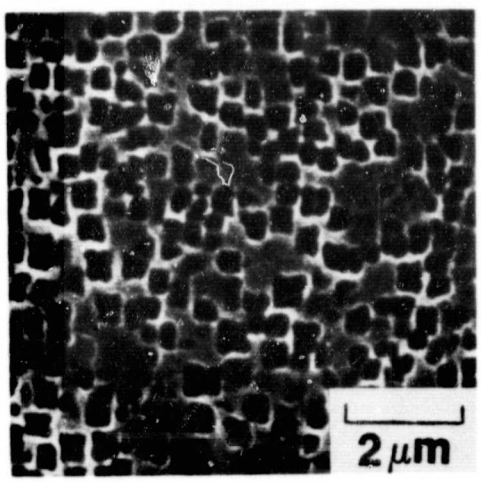

Figure 9. Refined γ' dispersion produced by homogenization.

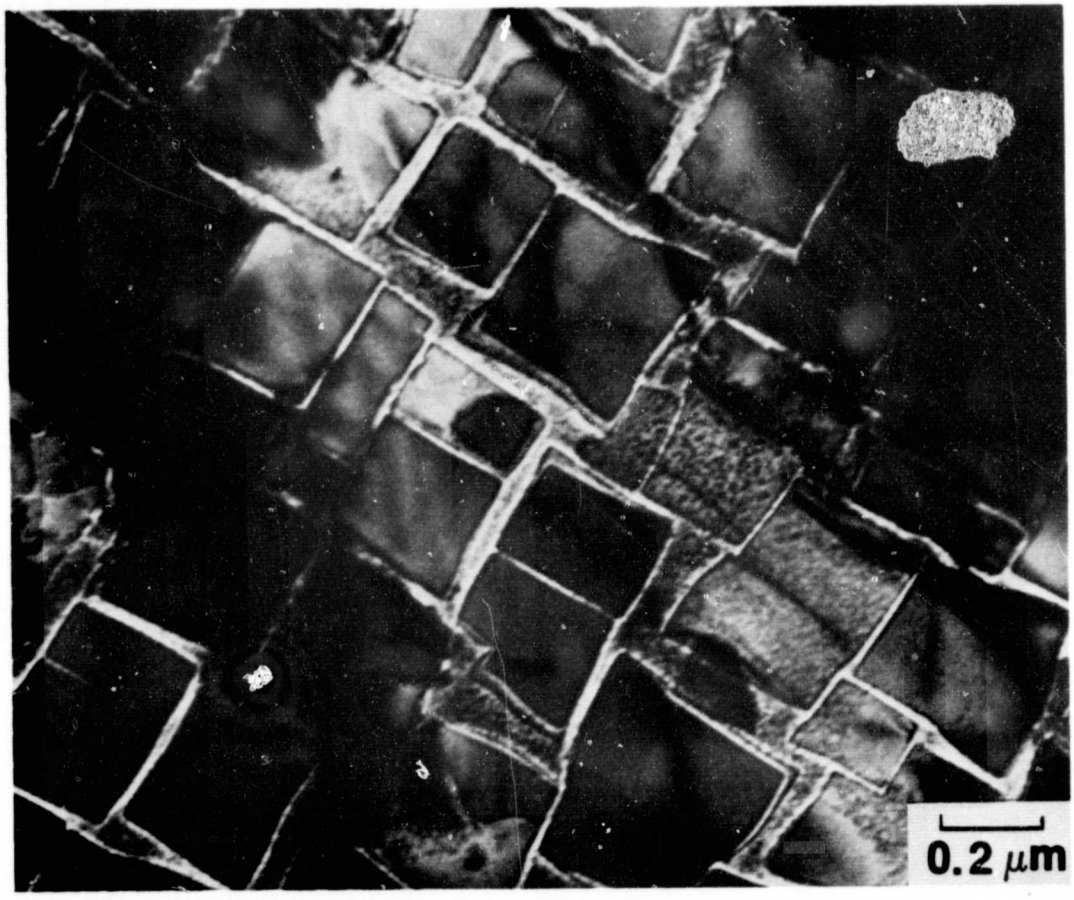

Figure 10. TEM micrograph showing mottled appearance of the γ matrix due to ultrafine γ' and γ'' Ni_3Mo phase.

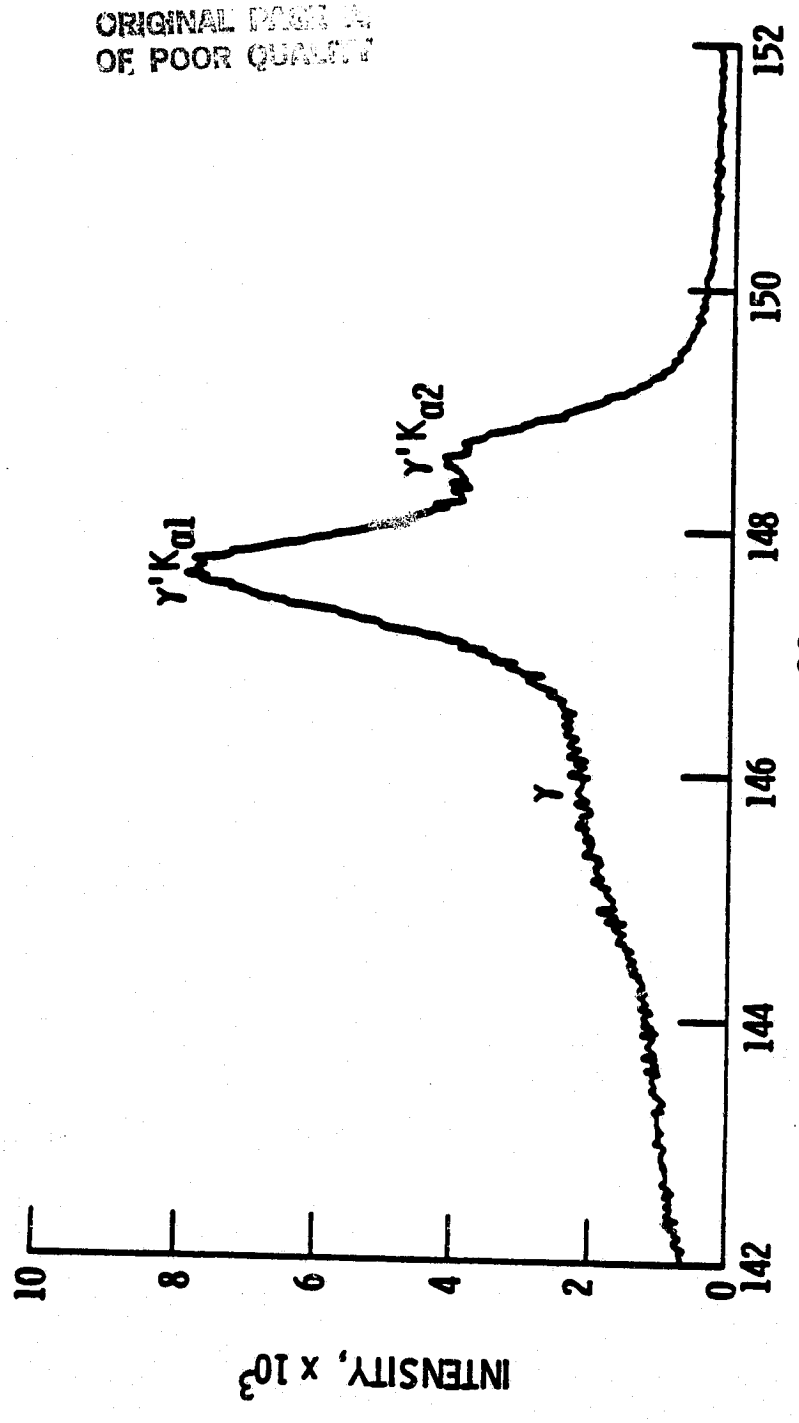

Figure 11. Diffractometer scan of the (024) γ and γ' peaks of a Ni-Al-Mo-Ta single crystal in the homogenized and air quenched condition.

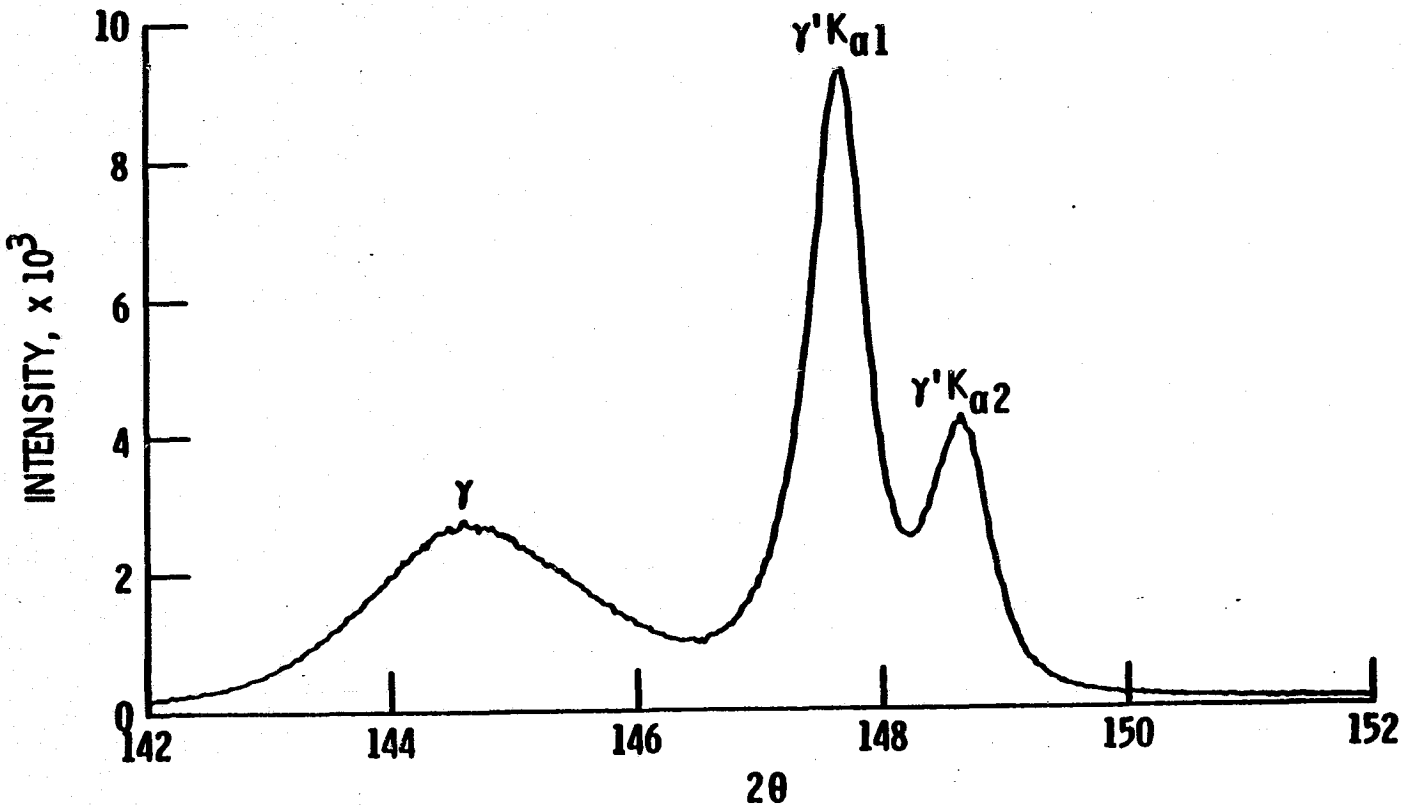

Figure 12. Diffractometer scan of the (024) γ and γ' peaks of a Ni-Al-Mo-Ta single crystal after homogenization and subsequent aging at 1080°C for four hours and at 870°C for sixteen hours.

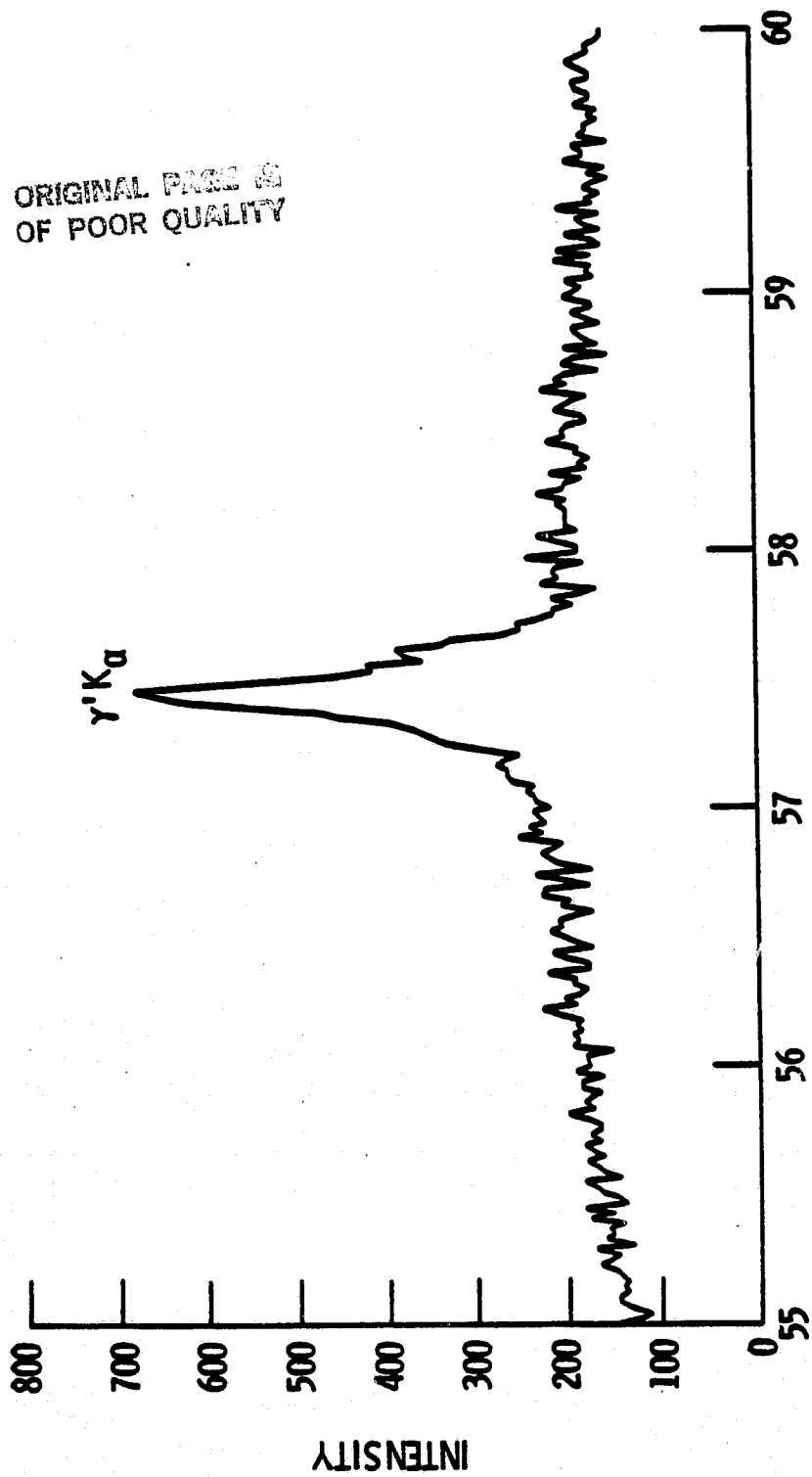

Figure 13. Diffractometer scan of the (012) γ' peak of a Ni-Al-Mo-Ta single crystal after homogenization and aging.

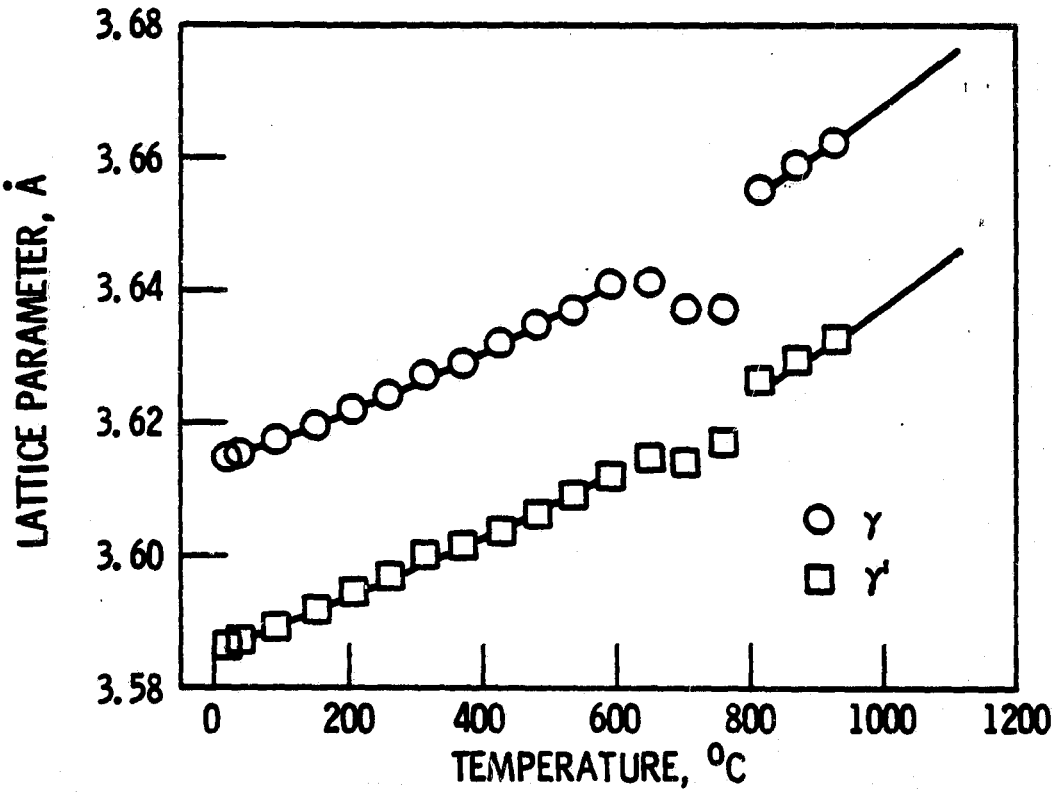

Figure 14. The lattice parameters of the γ and γ' phases are plotted as a function of temperature.

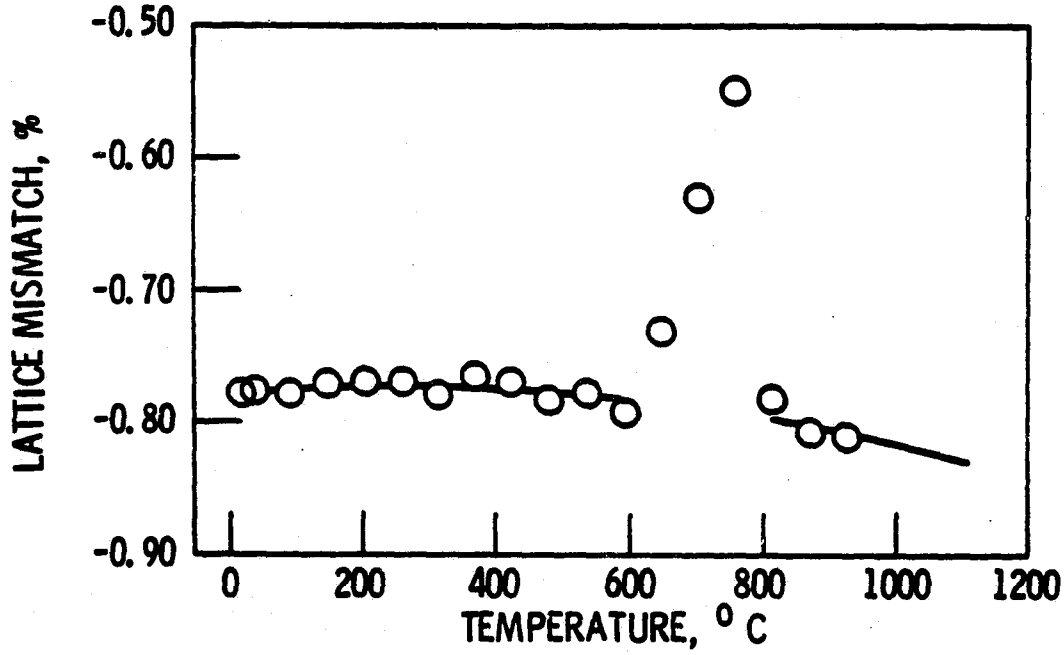

Figure 15. The mismatch in lattice parameter between γ and γ' is plotted as a function of temperature.

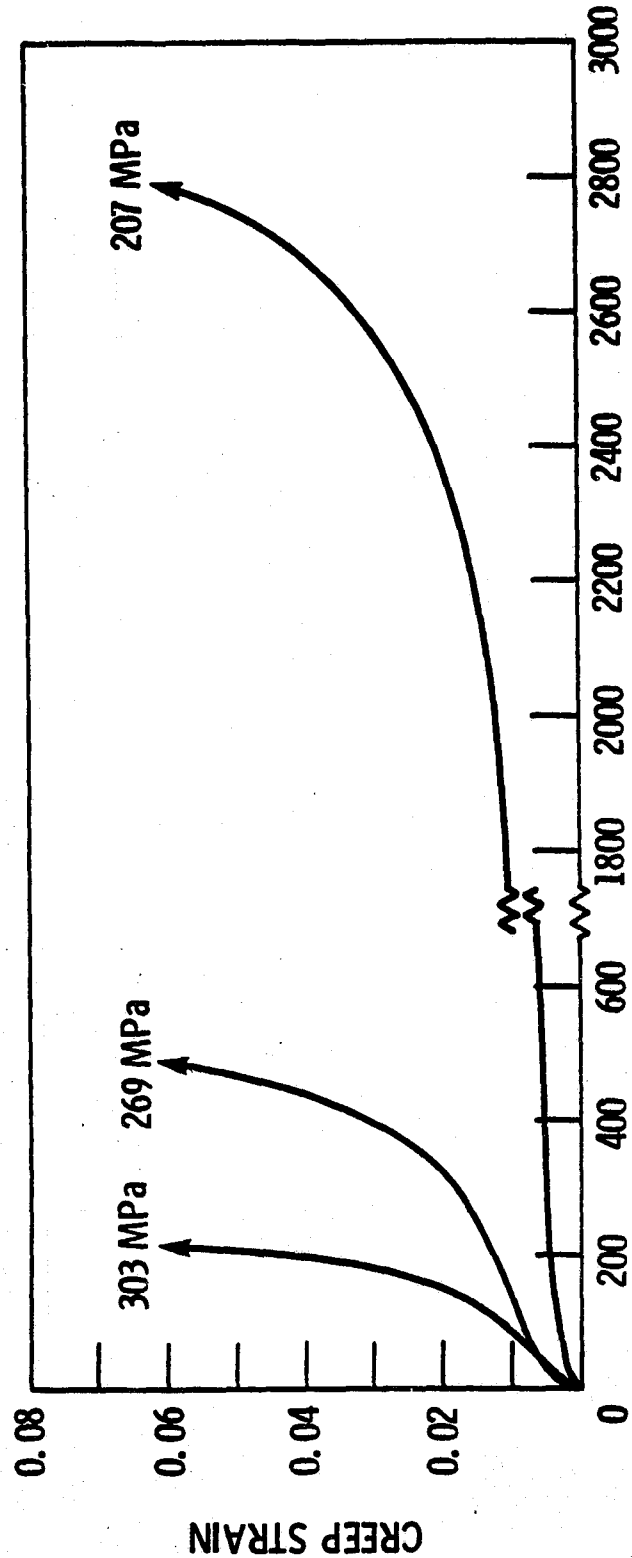

Figure 16. Creep rupture curves for specimens run to failure at various stress levels at 927°C.

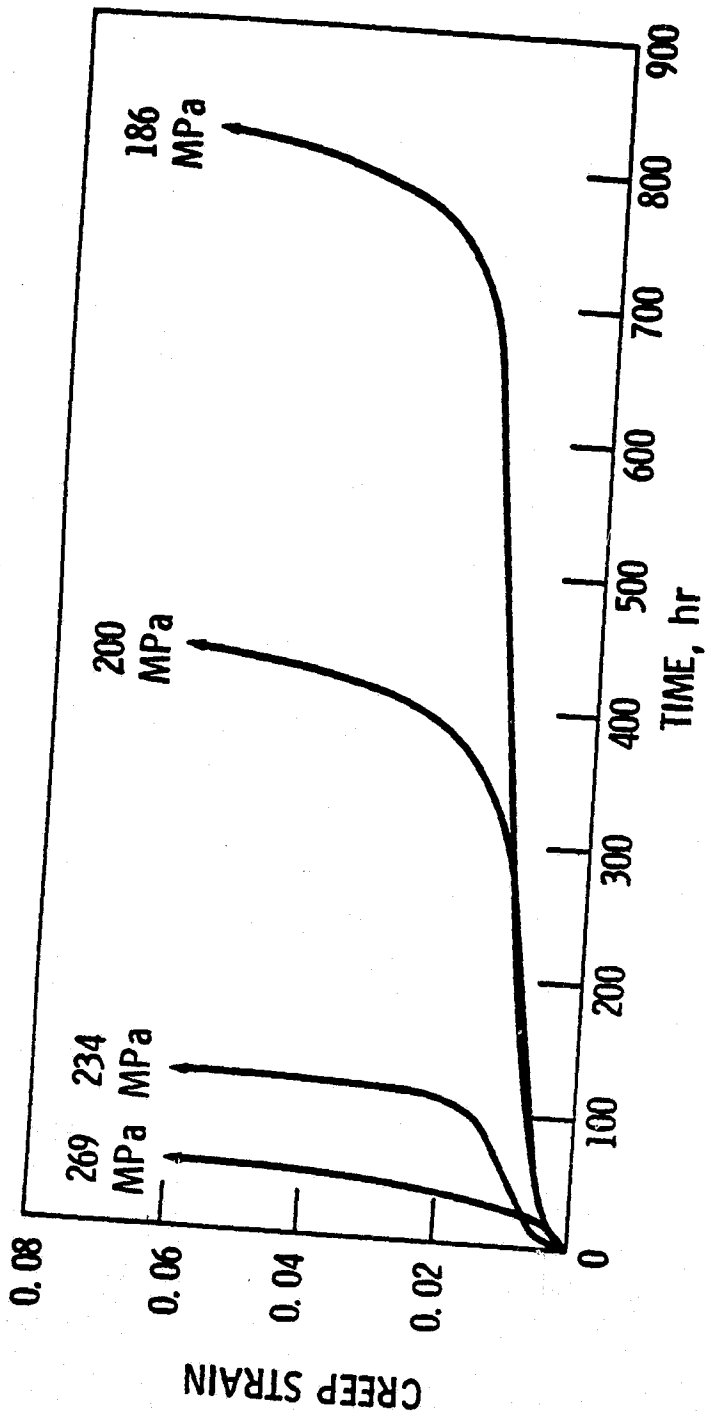

Figure 17. Creep rupture curves for specimens run to failure at various stress levels at 982°C.

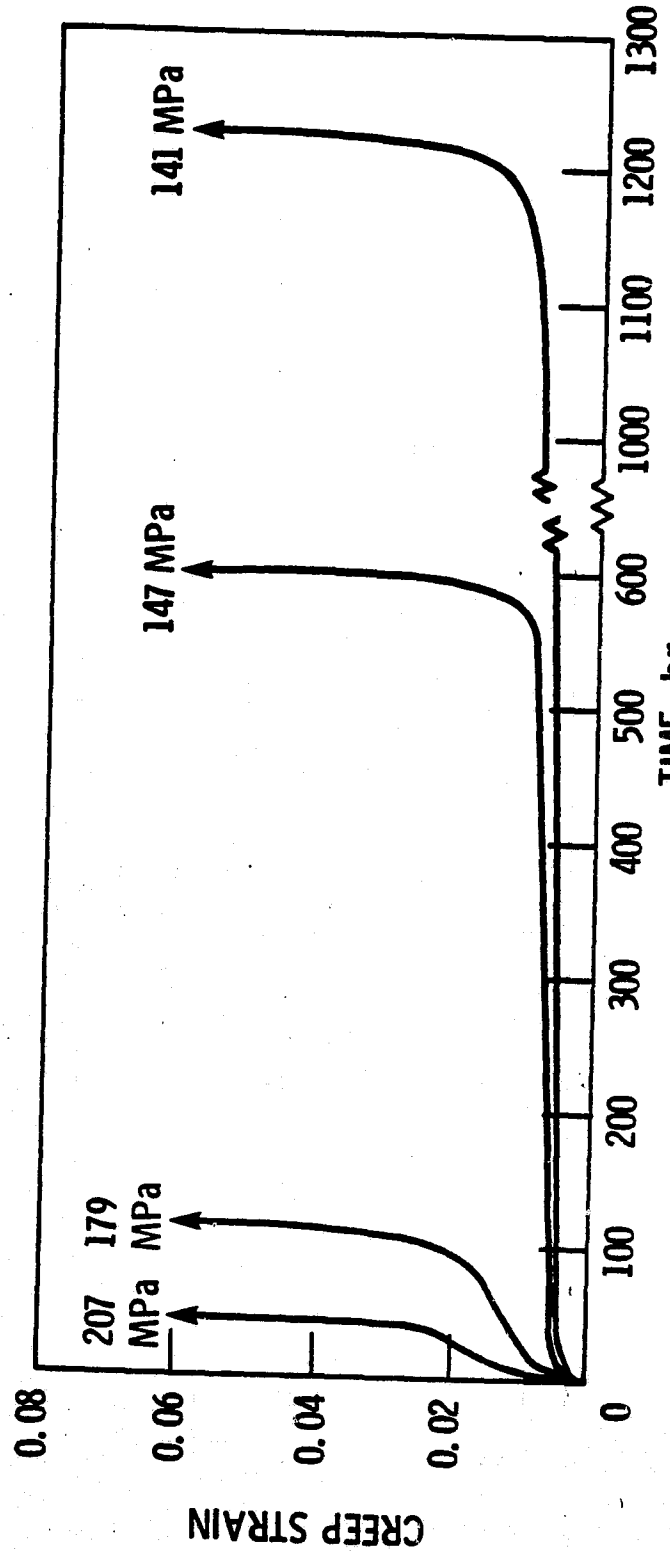

Figure 18. Creep rupture curves for specimens run to failure at various stress levels at 1038°C.

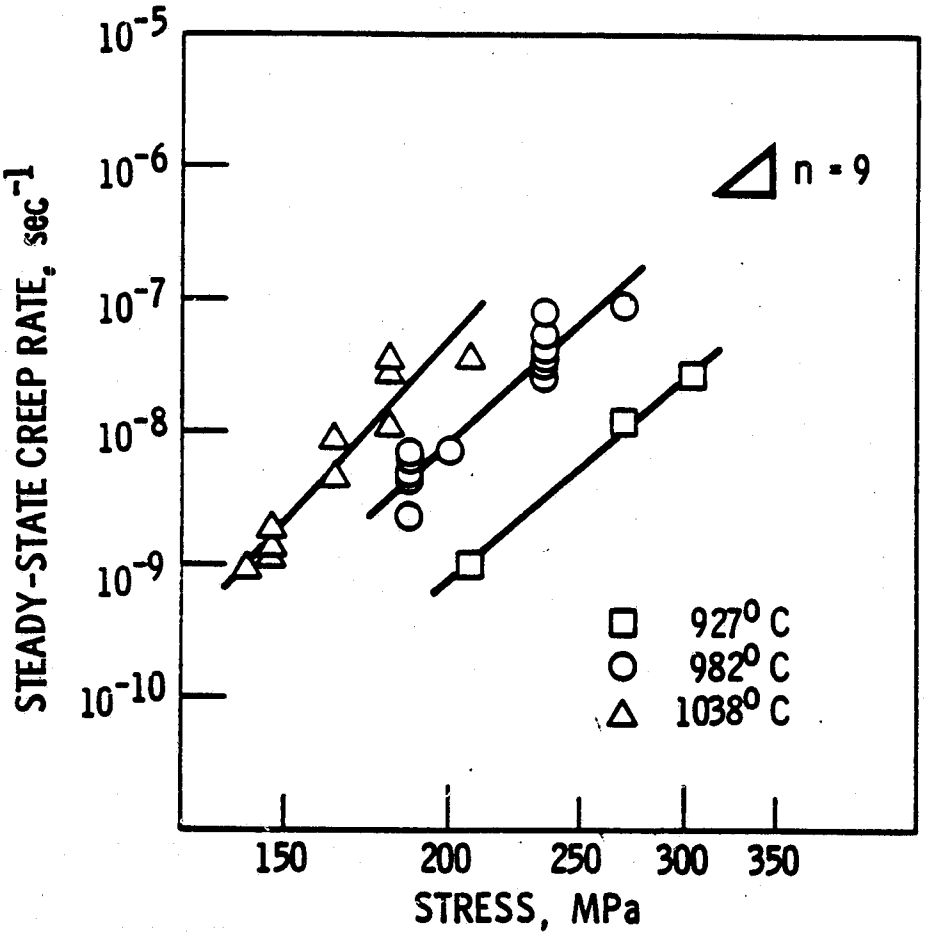

Figure 19. The stress dependence of steady-state creep rate is illustrated at 927, 982, and 1038°C. A slope, or stress exponent, n, of 9 is shown for comparison.

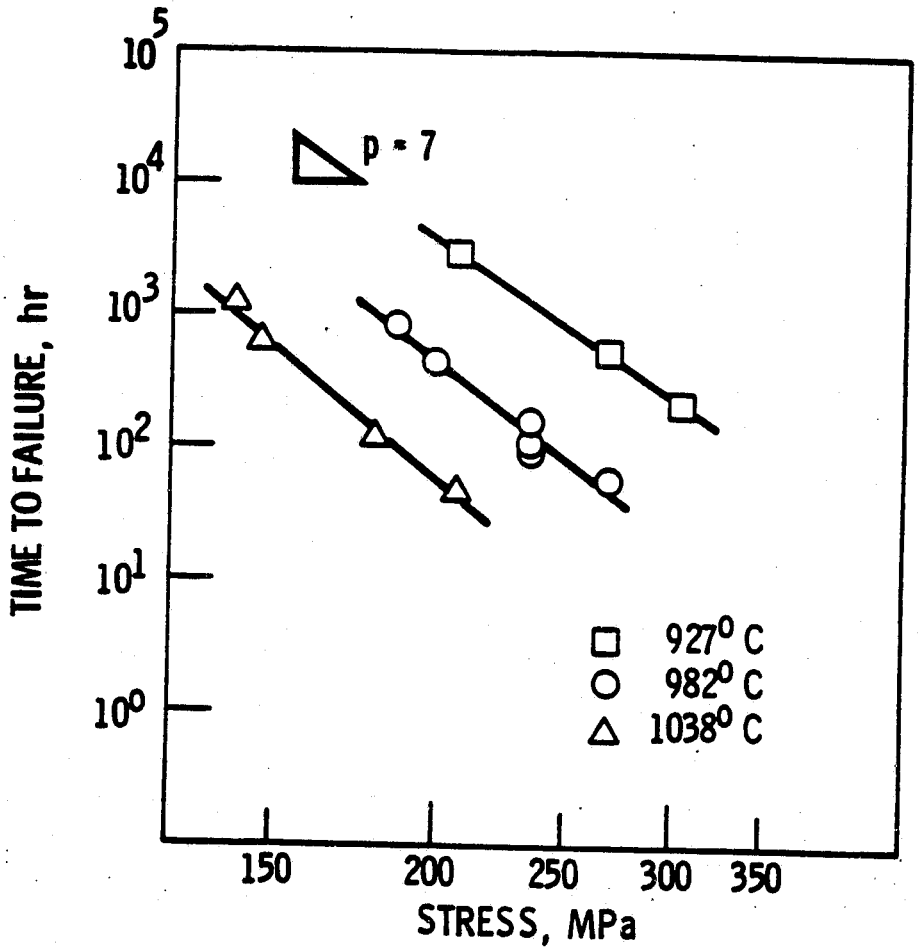

Figure 20. The stress dependence of creep rupture life is illustrated at 927, 982, and 1038°C. A slope equal to 7 is shown for comparison.

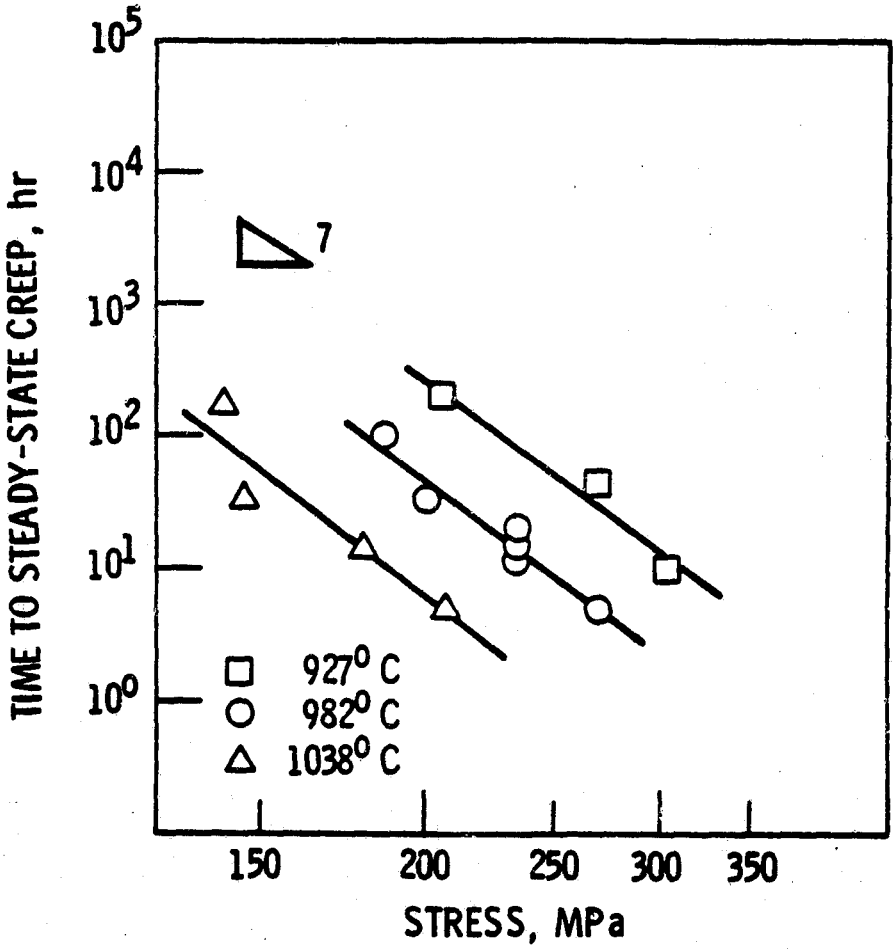

Figure 21. The time to the onset of steady-state creep is plotted versus stress at 927, 982, and 1038°C.

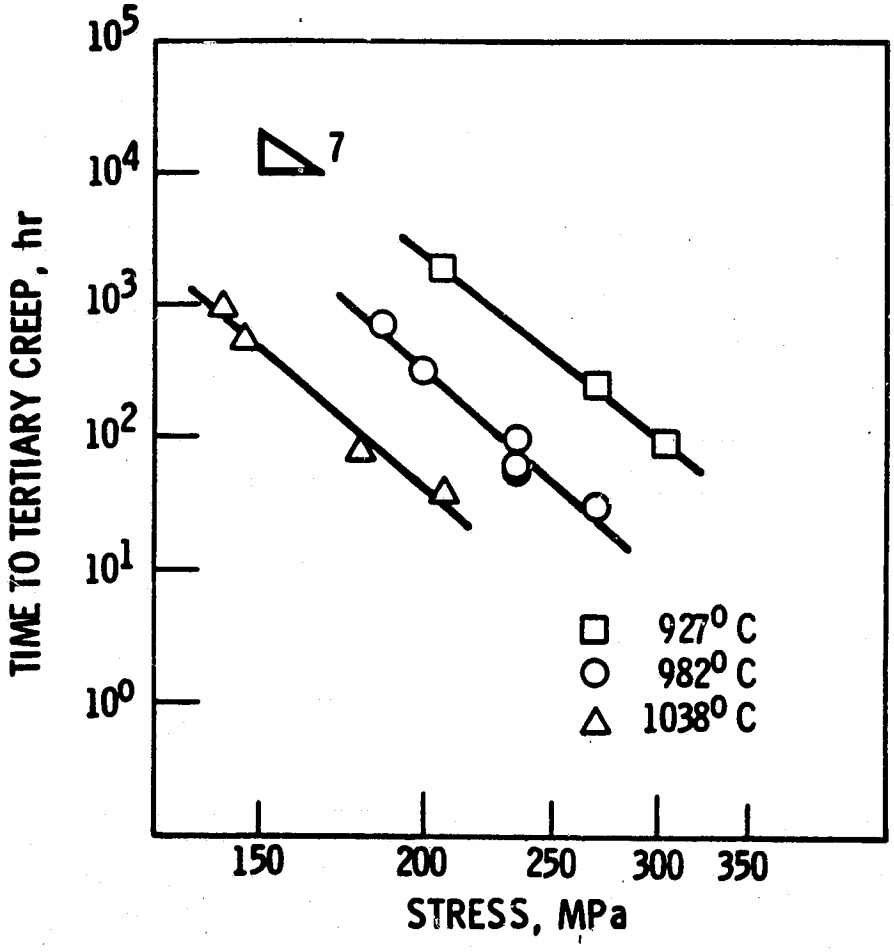

Figure 22. The time to the onset of tertiary creep is plotted versus stress at 927, 982, and 1038°C.

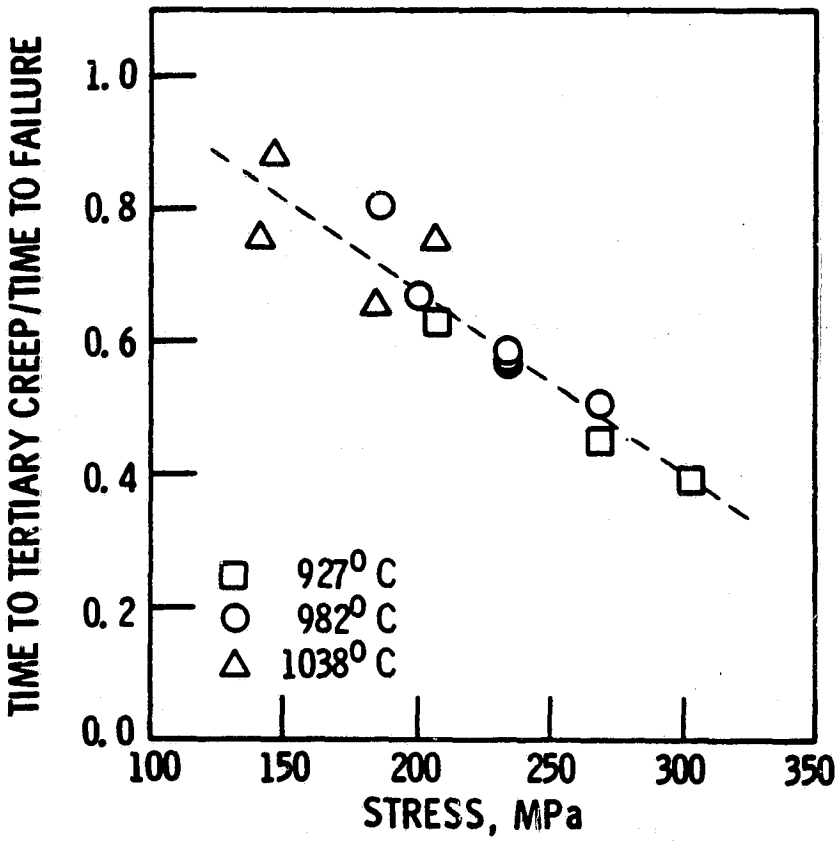

Figure 23. The ratio of the time to the onset of tertiary creep to the rupture life is plotted versus stress at 927, 982, and 1038°C.

Figure 24. The orientation of a γ' platelet is shown schematically for an [001]-oriented single crystal with a negative misfit under an applied uniaxial tensile stress.

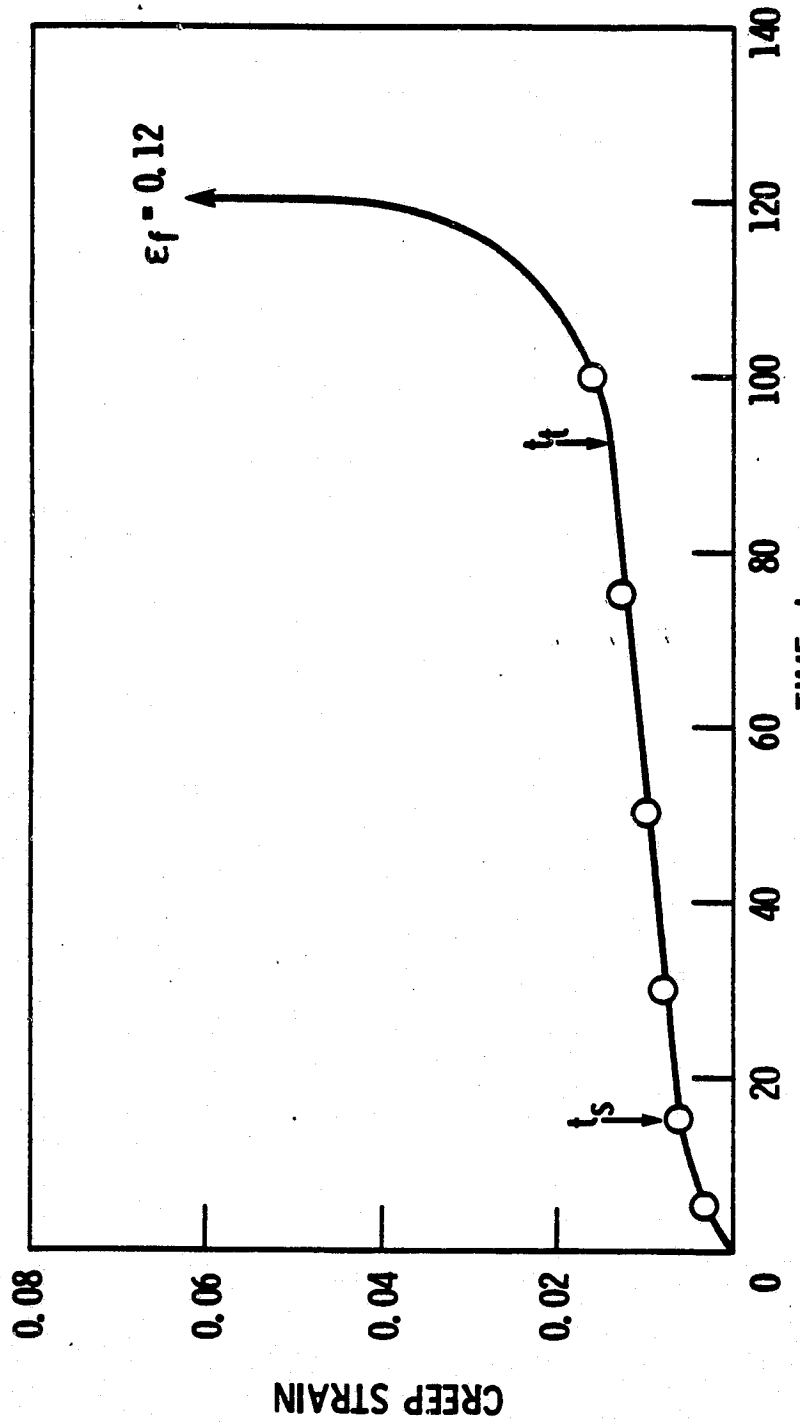

Figure 25. A typical creep curve of the Ni-Al-Mo-Ta single crystals tested at 982°C and 234 MPa. The open circles correspond to the microstructures, shown in Figure 26, of specimens whose tests were interrupted at specific times. The times to the onset of steady-state creep, t_s, and to the onset of tertiary creep, t_t, are indicated by the arrows.

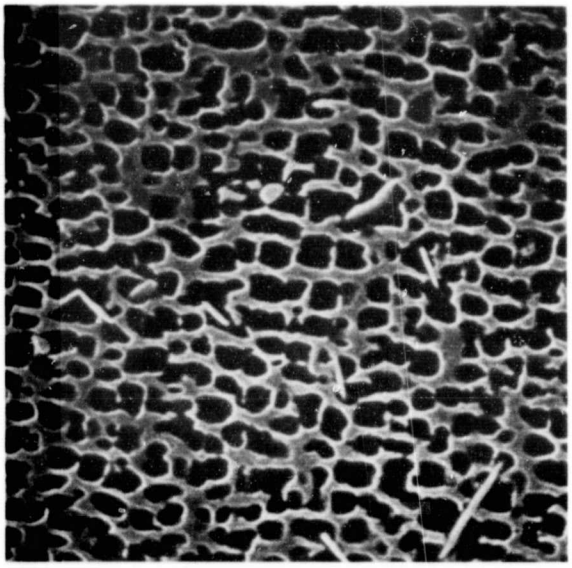

(a)

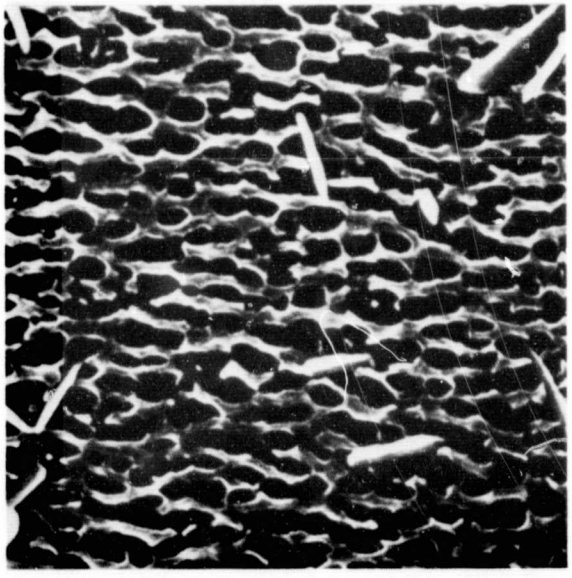

(b)

Figure 26. The development of directional coarsening of γ' at 982°C and 234 MPa is illustrated at: (a) 5, (b) 15, (c) 30, (d) 50, (e) 75, (f) 99.8, and (g) 120 hours, in failed condition. The stress axis is vertical in all photos.

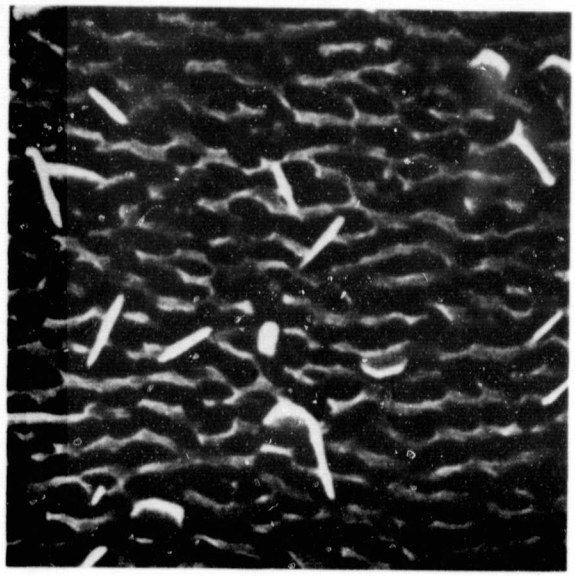

(c)

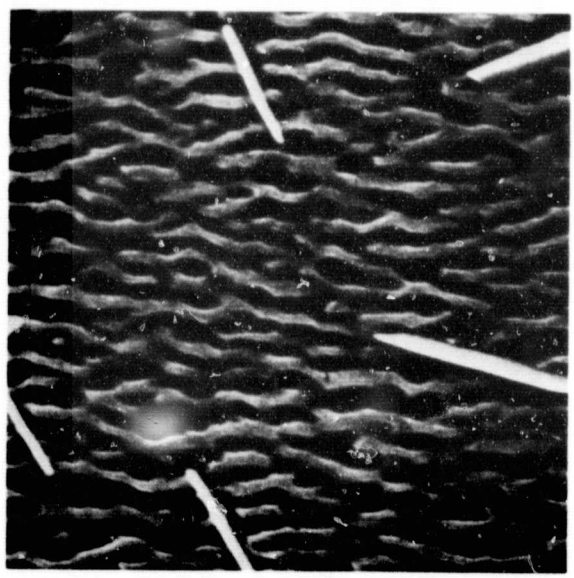

(d)

Figure 26 continued

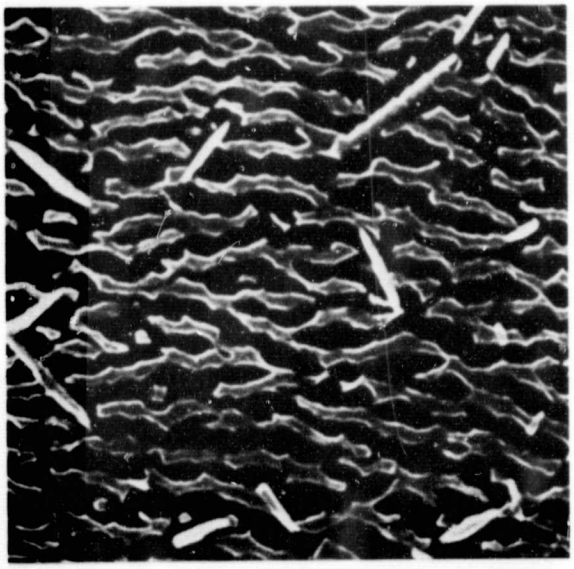

(e)

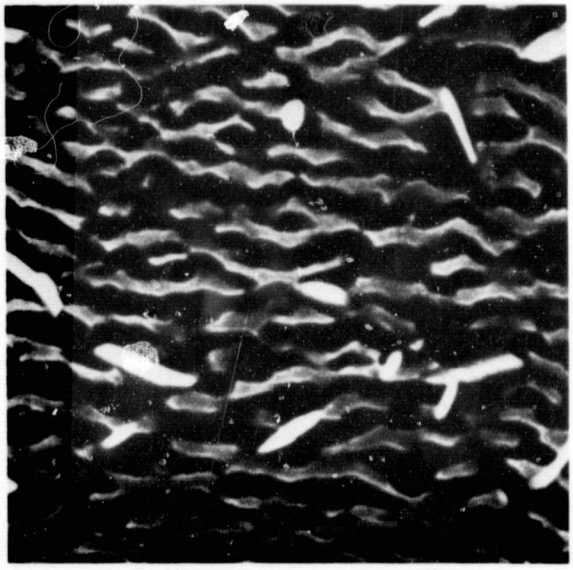

(f)

Figure 26 continued

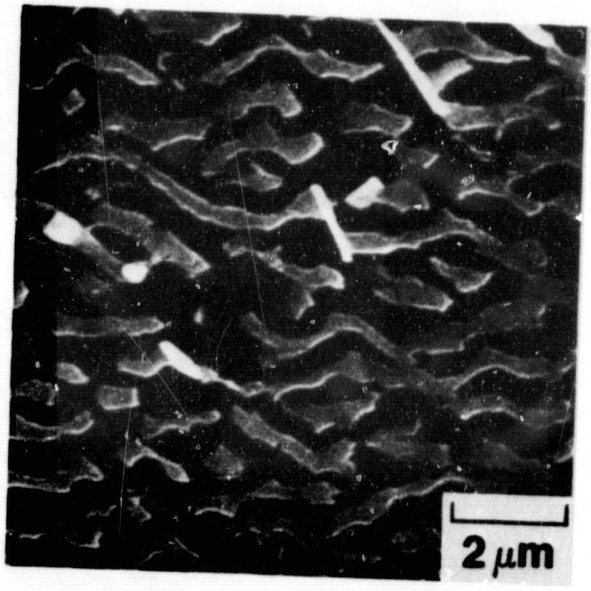

(g)

Figure 26 concluded

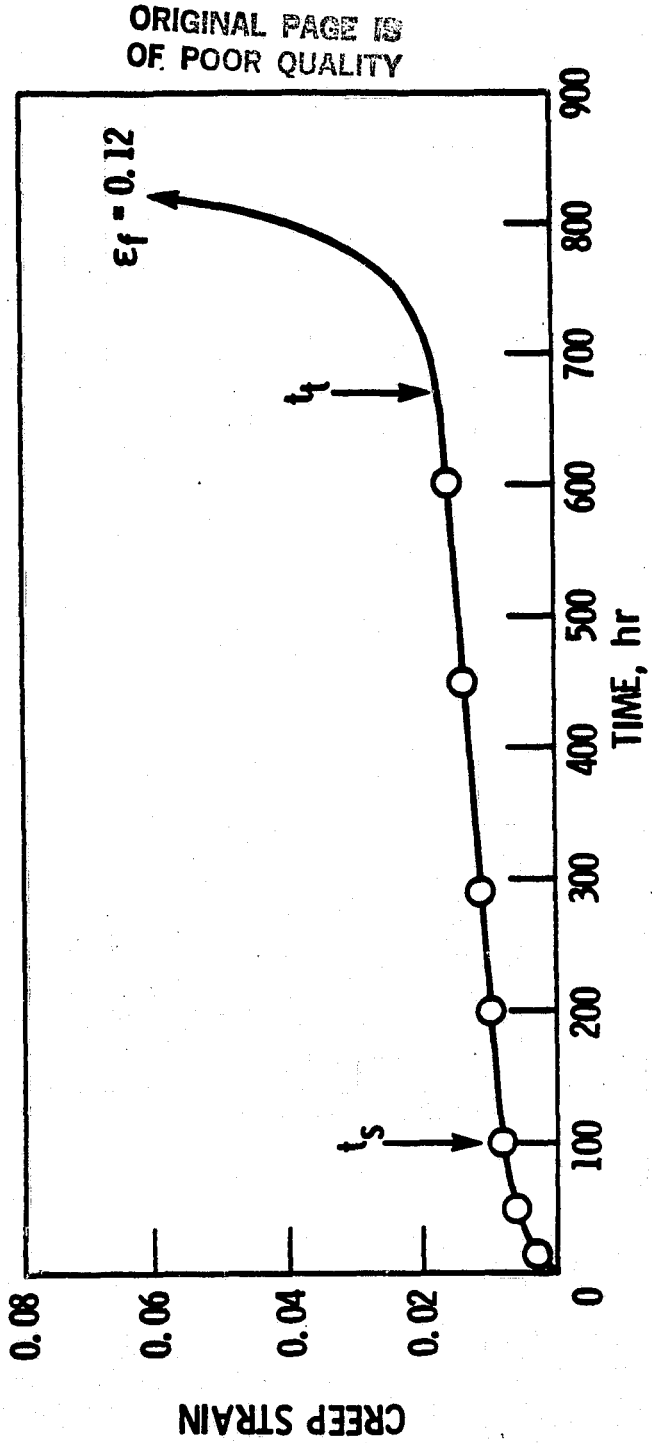

Figure 27. A typical creep curve of the Ni-Al-Mo-Ta single crystals tested at 982°C and 186 MPa. The open circles correspond to the microstructures, shown in Figure 28, of specimens whose tests were interrupted at specific times. The times to the onset of steady-state creep, t_s, and to the onset of tertiary creep, t_t, are indicated by the arrows.

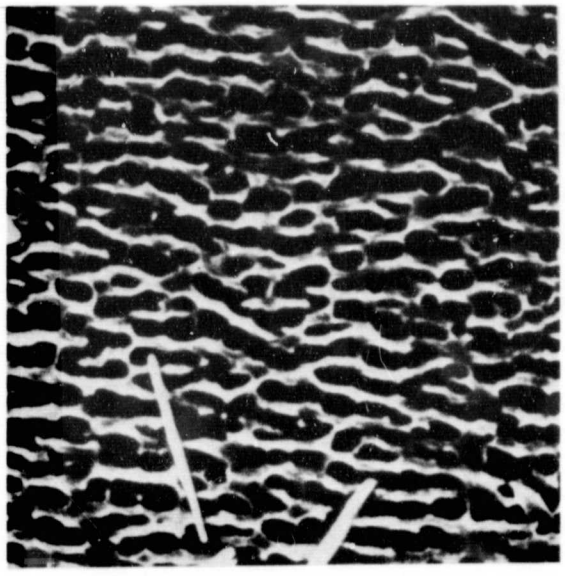

(a)

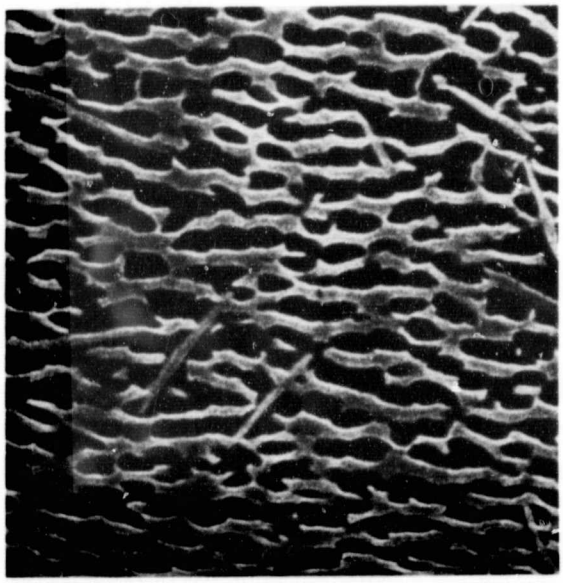

(b)

Figure 28. The development of directional coarsening of γ' at 982°C and 186 MPa is illustrated at: (a) 15, (b) 50, (c) 100, (d) 199, (e) 295, (f) 450, (g) 600, and (h) 831 hours, in failed condition. The stress axis is vertical in all photos.

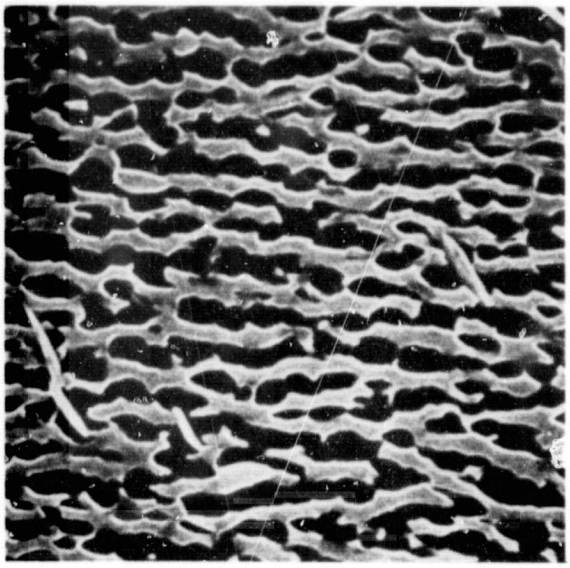

(c)

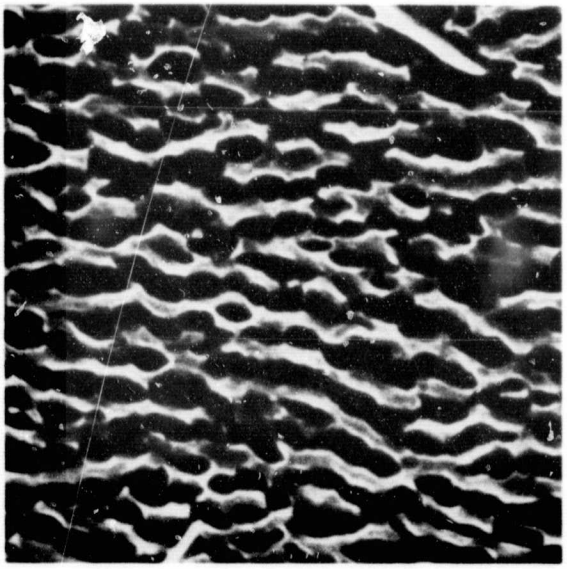

(d)

Figure 28 continued

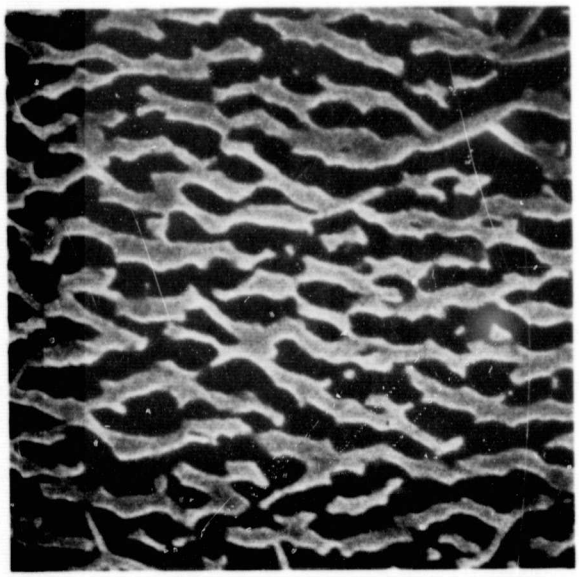

(e)

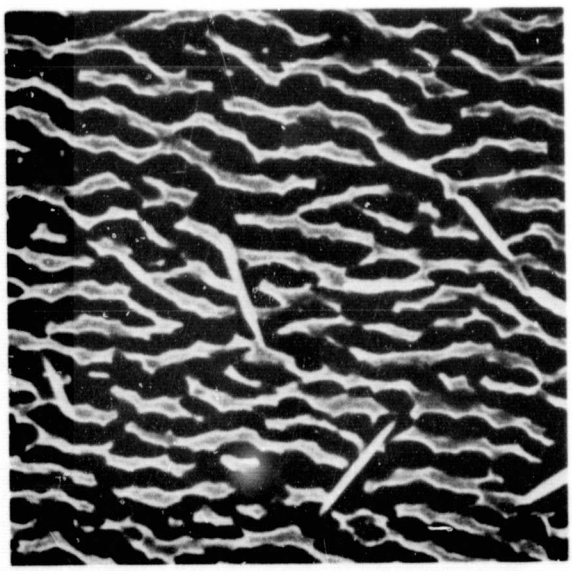

(f)

Figure 28 continued

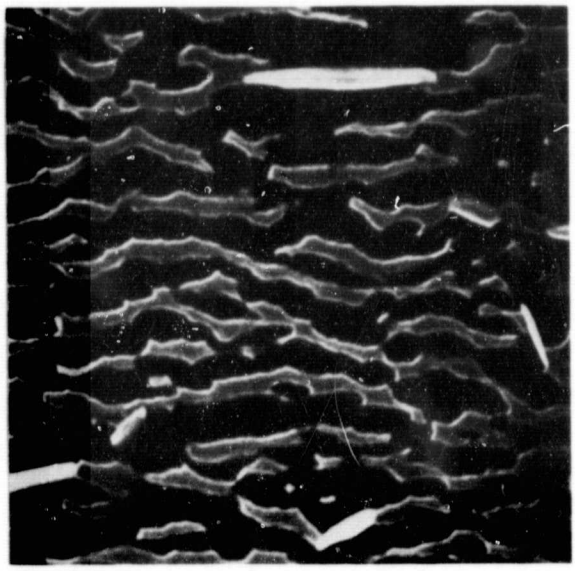

(g)

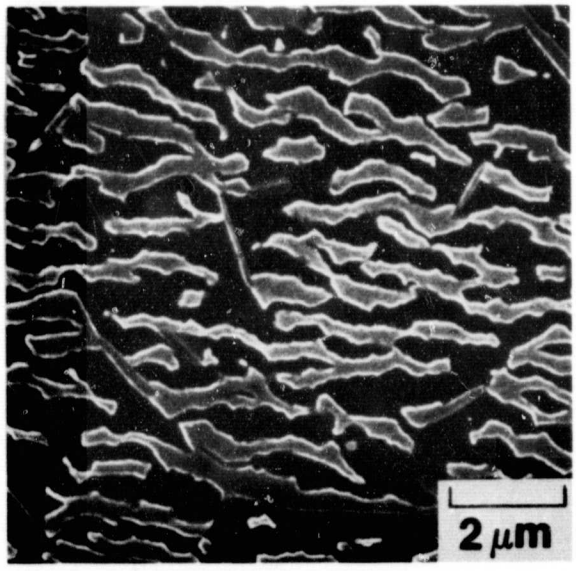

(h)

Figure 28 concluded

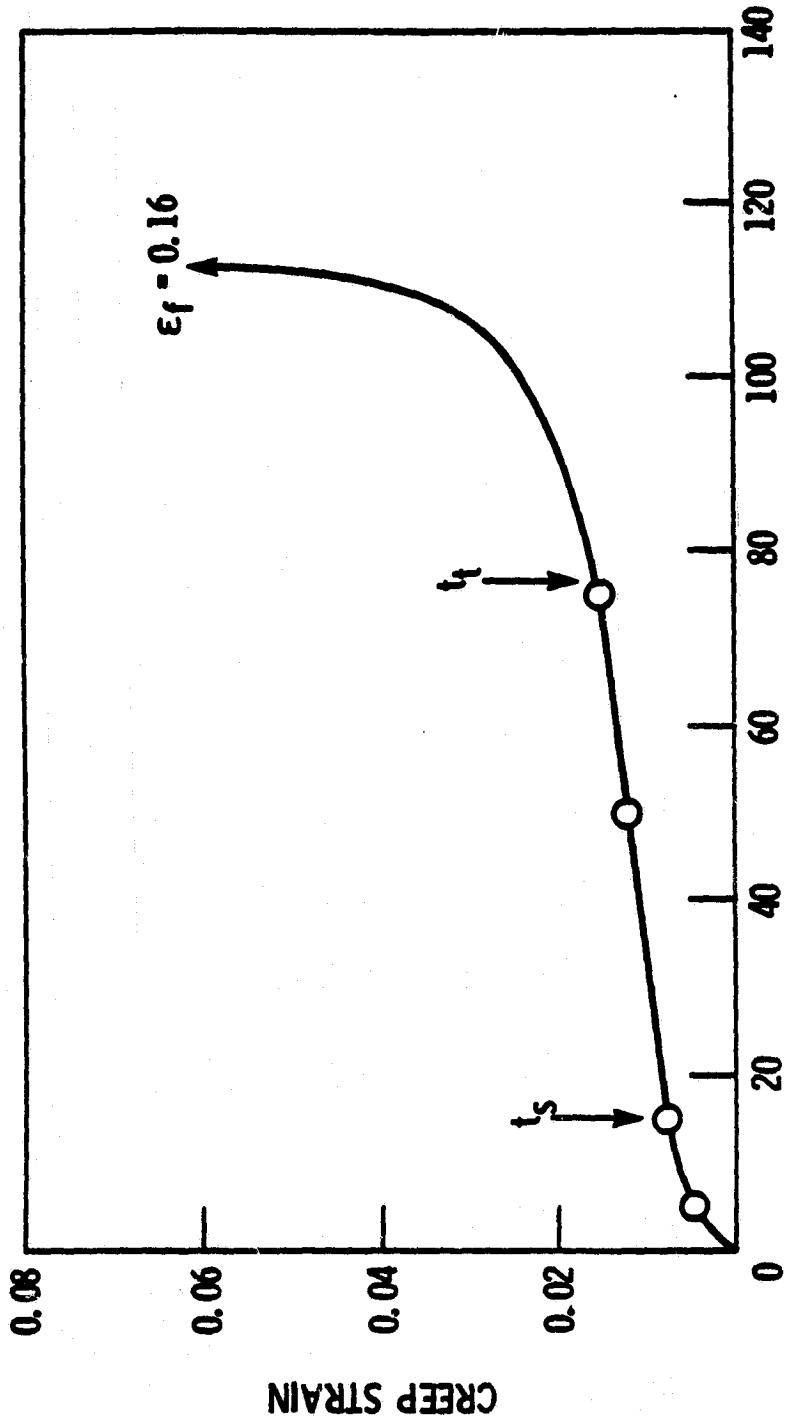

Figure 29. A typical creep curve of the Ni-Al-Mo-Ta single crystals tested at 1038°C and 179 MPa. The open circles correspond to the microstructures, shown in Figure 30, of specimens whose tests were interrupted at specific times. The times to the onset of steady-state creep, t_s, and to the onset of tertiary creep, t_t, are indicated by the arrows.

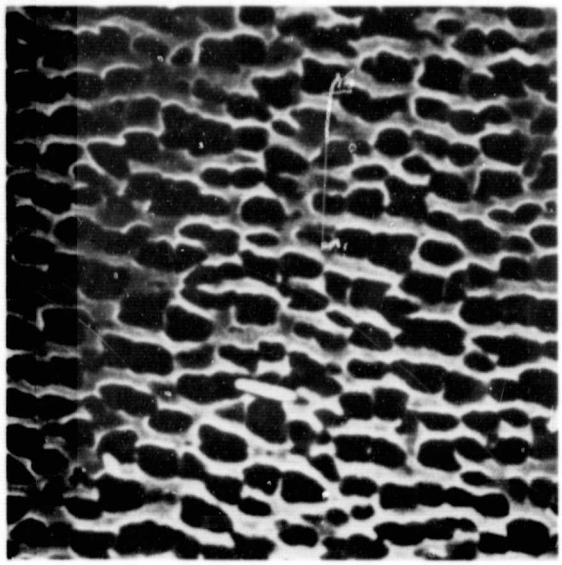

(a)

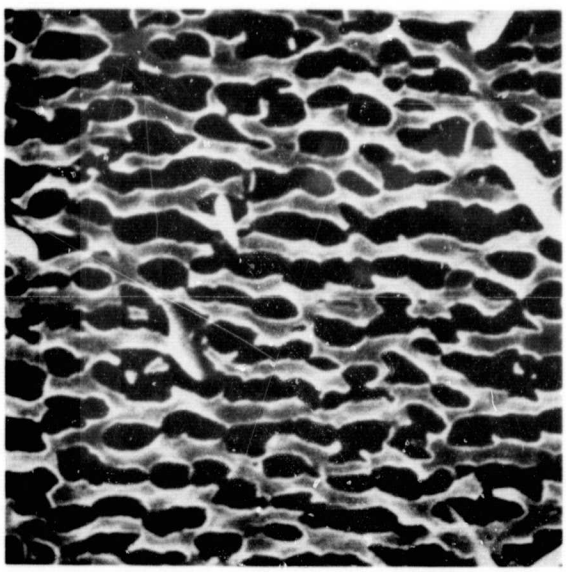

(b)

Figure 30. The development of directional coarsening of γ' at $1038^{o}C$ and 179 MPa is illustrated at: (a) 5, (b) 15, (c) 50, (d) 75, (e) 116.3 hours, in failed condition away from the neck, and (f) 116.3 hours, in failed condition behind the fracture surface. The stress axis is vertical in all photos.

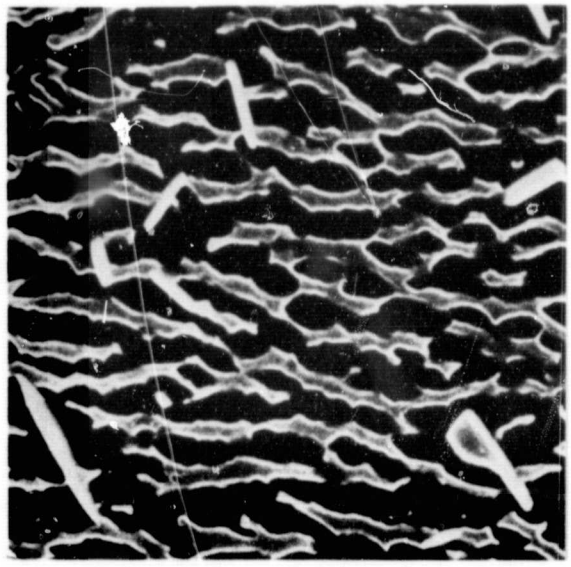

(c)

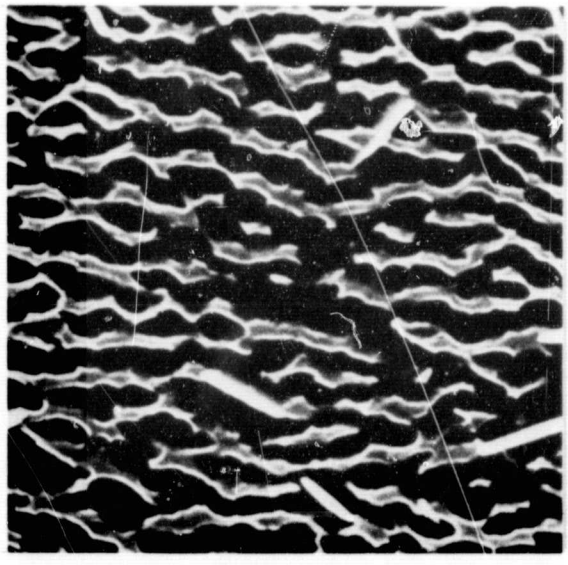

(d)

Figure 30 continued

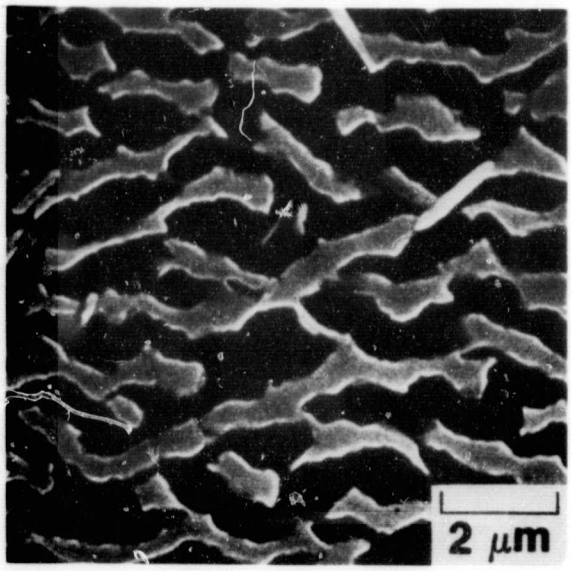

(e)

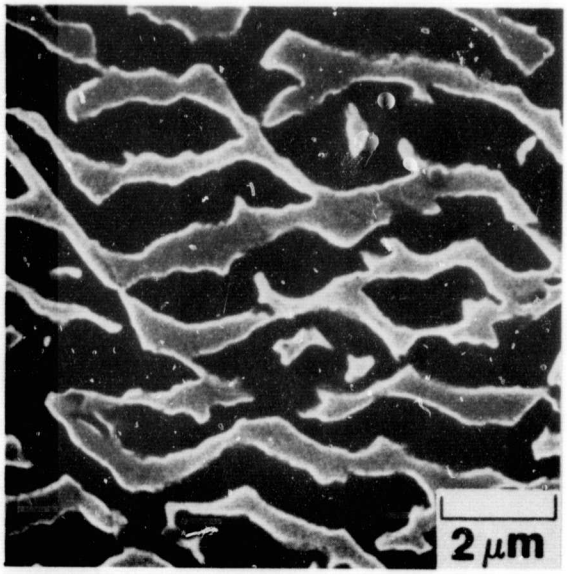

(f)

Figure 30 concluded

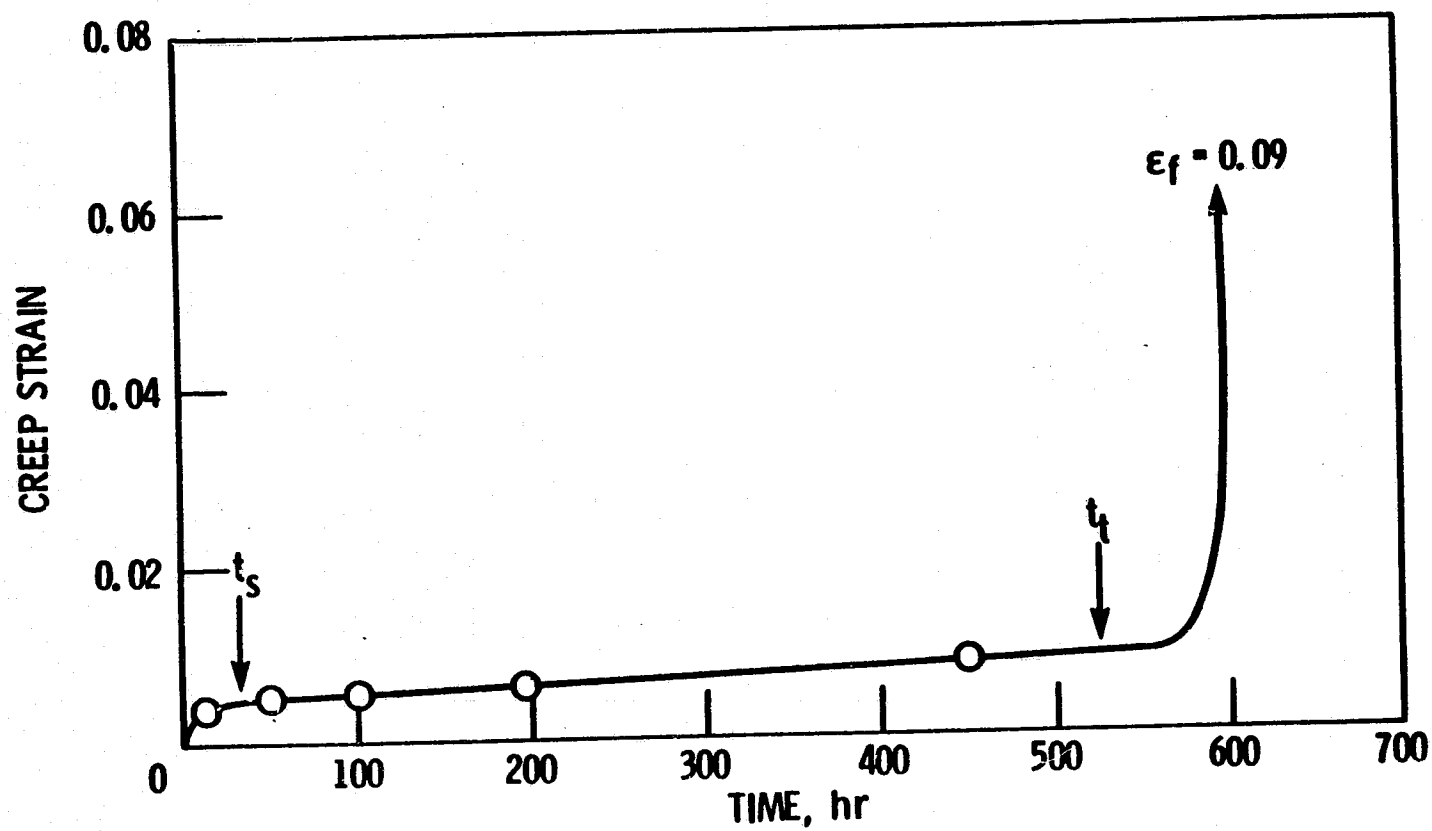

Figure 31. A typical creep curve of the Ni-Al-Mo-Ta single crystals tested at 1038°C and 147 MPa. The open circles correspond to the microstructures, shown in Figure 32, of specimens whose tests were interrupted at specific times. The times to the onset of steady-state creep, t_s, and to the onset of tertiary creep, t_t, are indicated by the arrows.

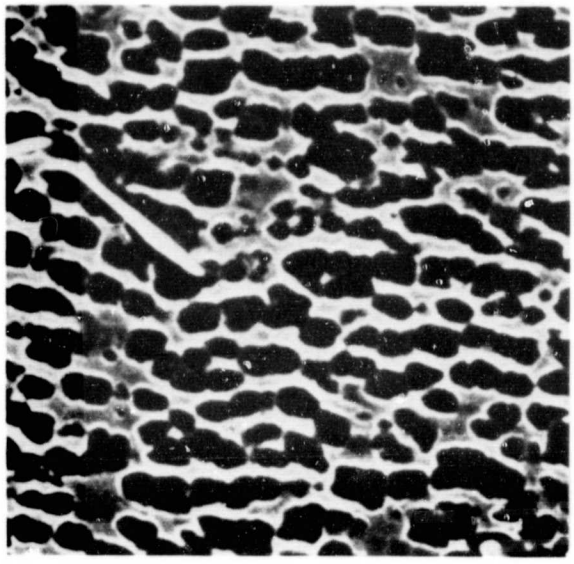

(a)

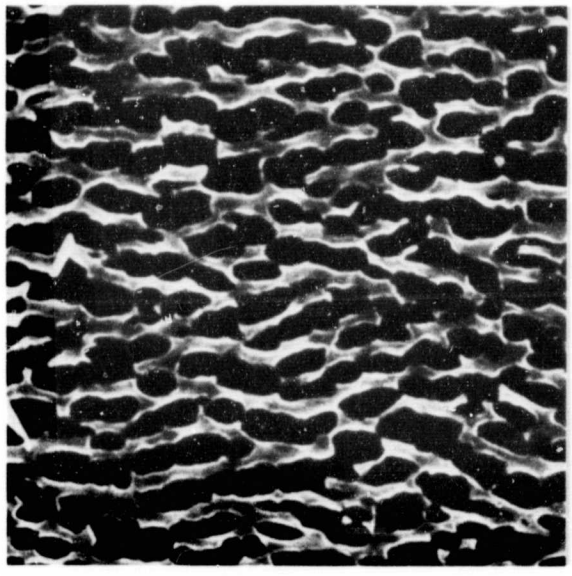

(b)

Figure 32. The development of directional coarsening of γ' at $1038^{o}C$ and 147 MPa is illustrated at: (a) 15, (b) 50, (c) 100, (d) 195, (e) 450, and (f) 598 hours, in failed condition. The stress axis is vertical in all photos.

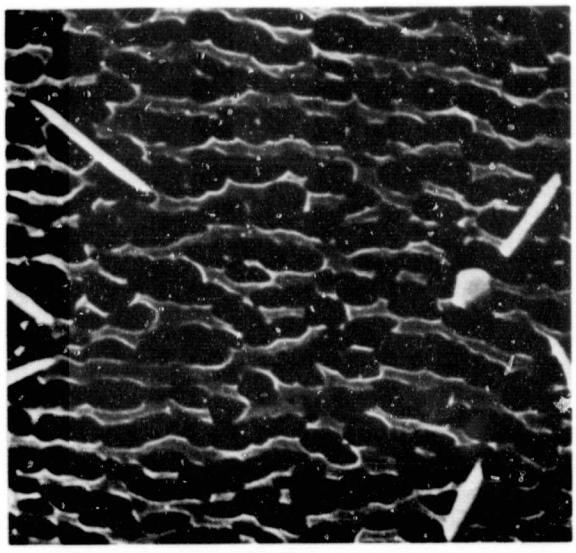

(c)

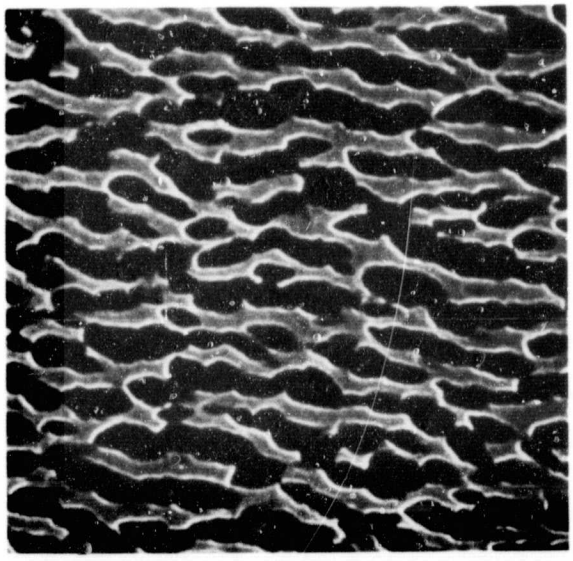

(d)

Figure 32 continued

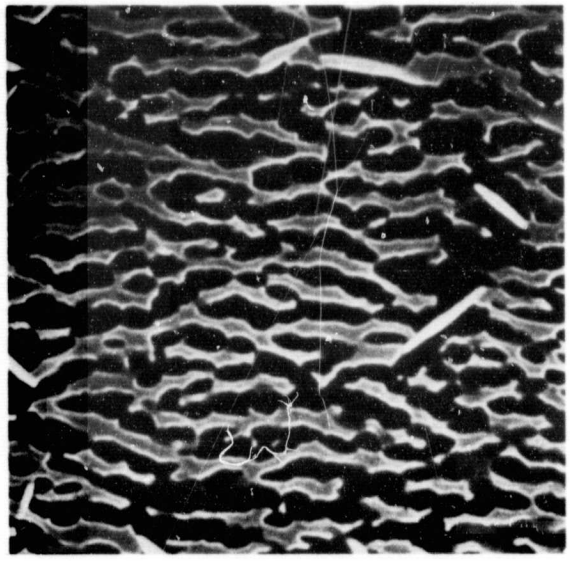

(e)

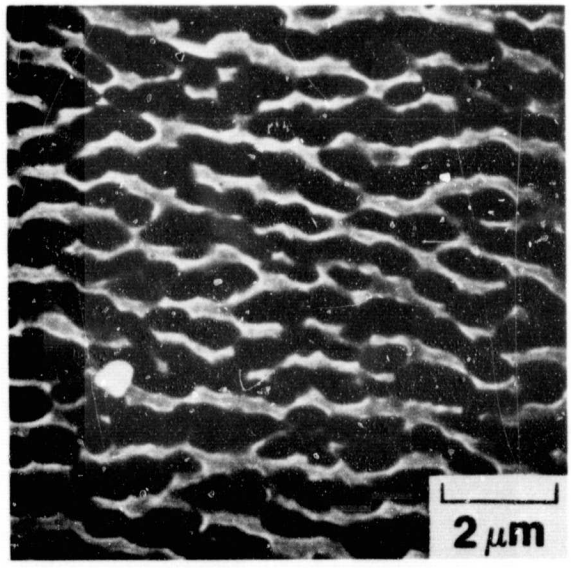

(f)

Figure 32 concluded

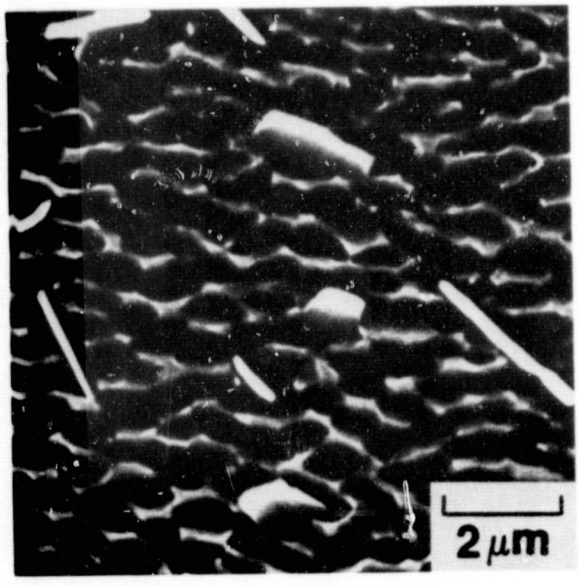

(a)

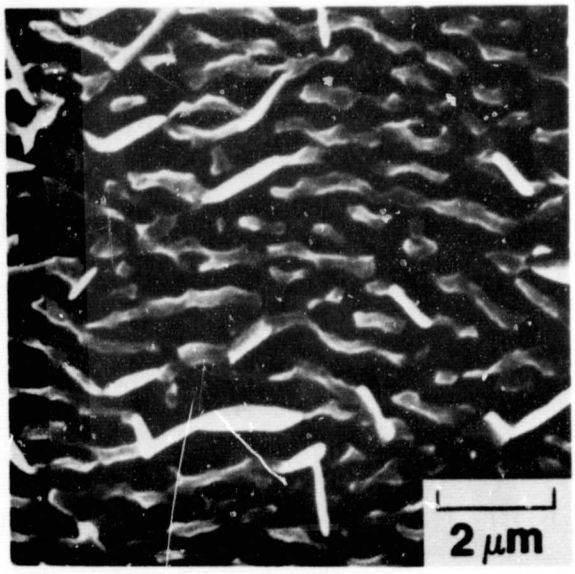

(b)

Figure 33. Directionally coarsened γ' in failed creep specimens tested at 927°C and (a) 303 MPa, (b) 269 MPa, (c) 207 MPa, in uniform gage section, and (d) 207 MPa, in necked region. The stress axis is vertical in all photos.

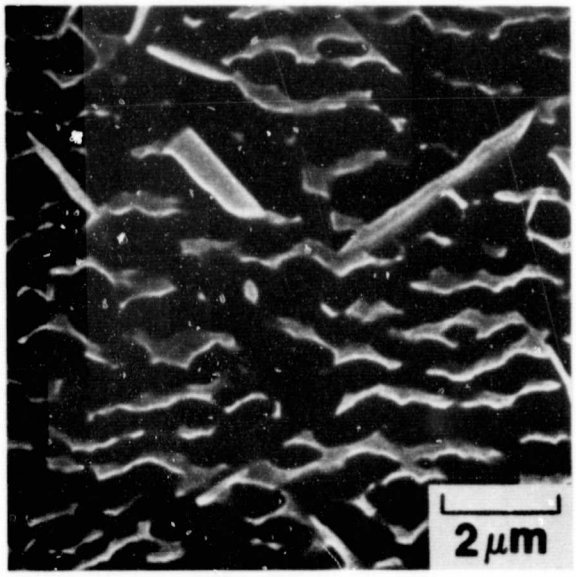

(c)

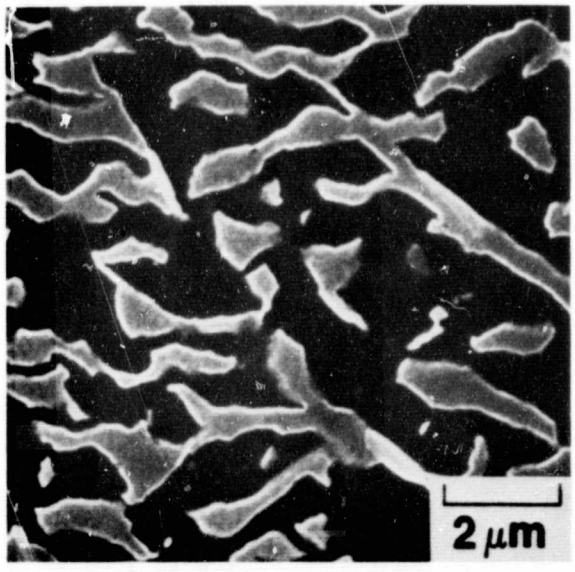

(d)

Figure 33 concluded

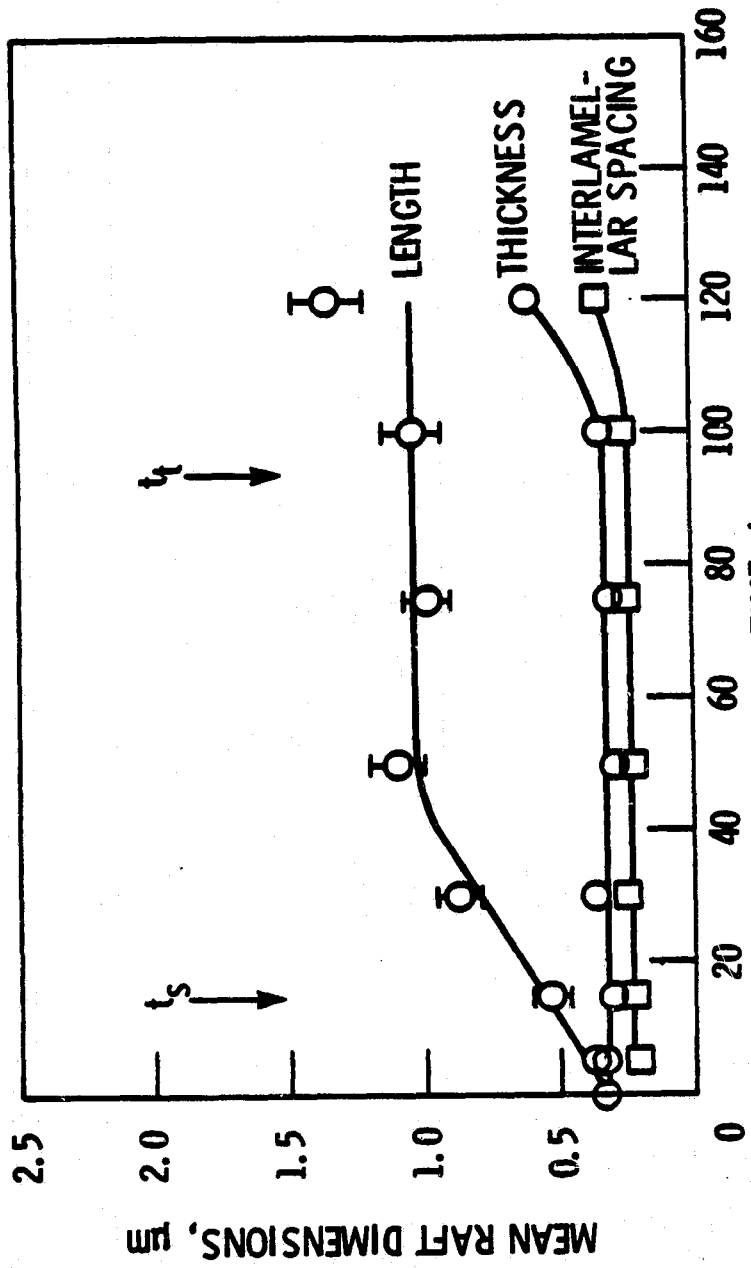

Figure 34. The mean dimensions of the γ' rafts are plotted as a function of time during creep at 982°C and 234 MPa. Error bars for 95 pct. confidence intervals were drawn when end points of intervals were outside of data point symbols.

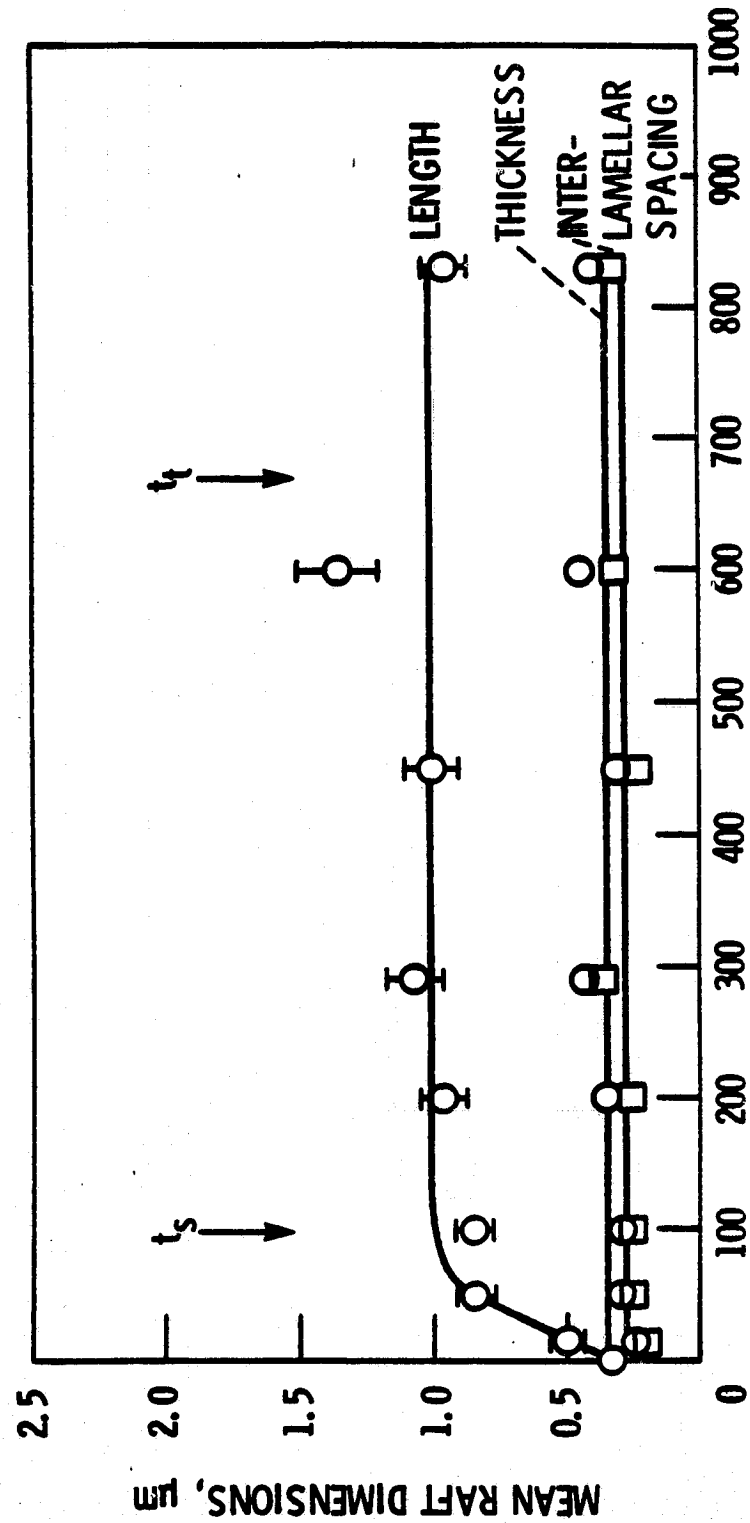

Figure 35. The mean dimensions of the γ' rafts are plotted as a function of time during creep at 982°C and 186 MPa. Error bars for 95 pct. confidence intervals were drawn when end points of intervals were outside of data point symbols.

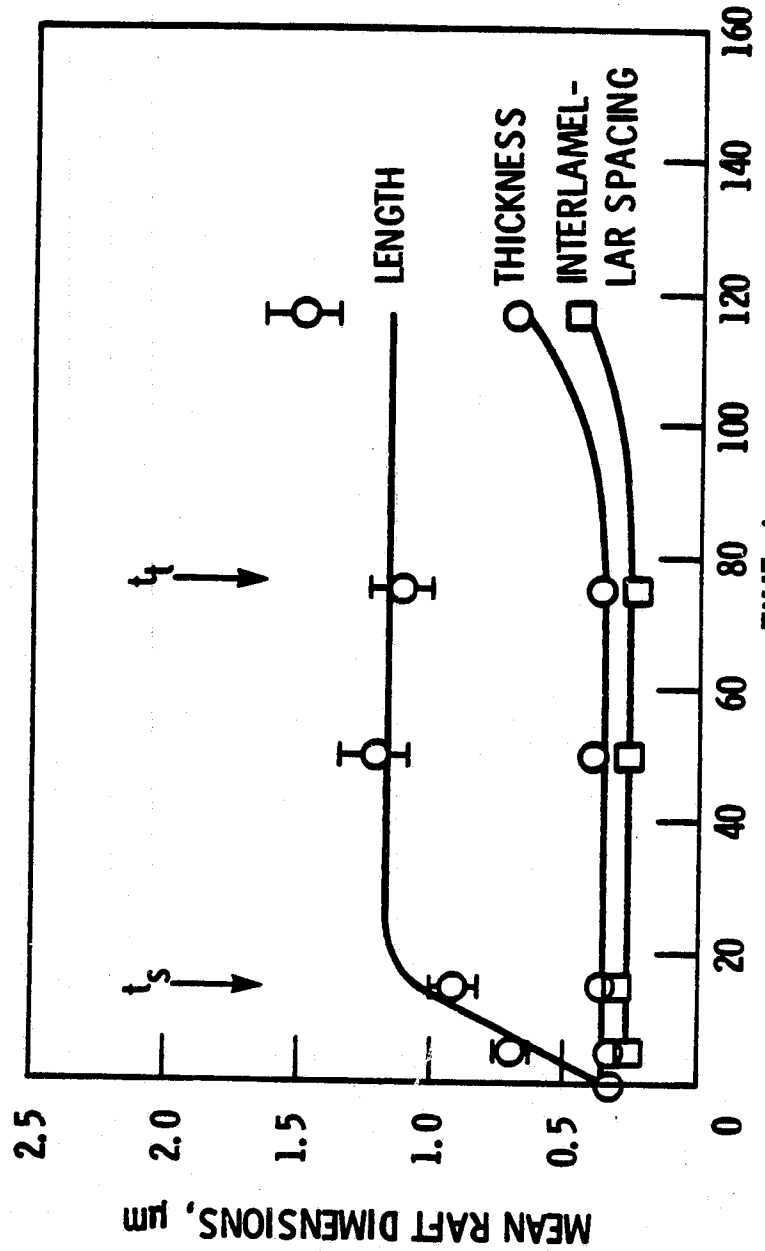

Figure 36. The mean dimensions of the γ' rafts are plotted as a function of time during creep at 1038°C and 179 MPa. Error bars for 95 pct. confidence intervals were drawn when end points of intervals were outside of data point symbols.

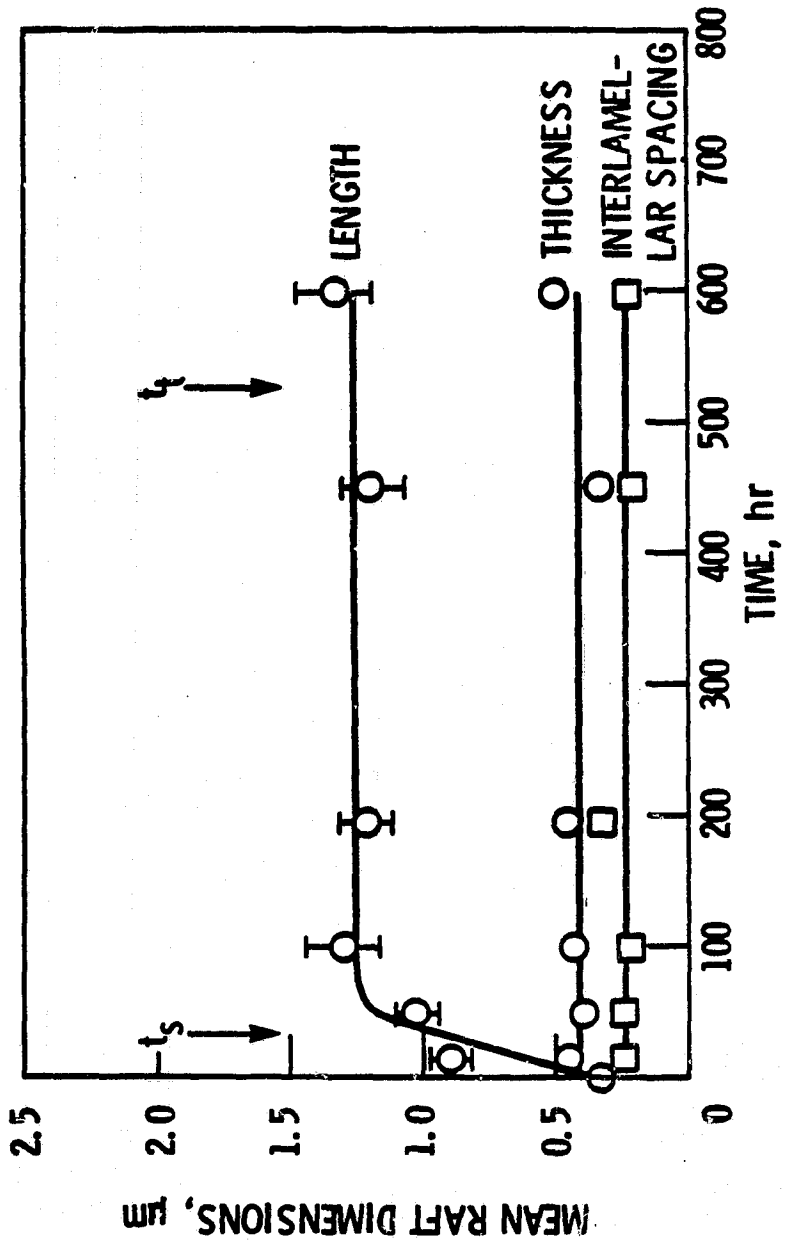

Figure 37. The mean dimensions of the γ' rafts are plotted as a function of time during creep at 1038°C and 147 MPa. Error bars for 95 pct. confidence intervals were drawn when end points of intervals were outside of data point symbols.

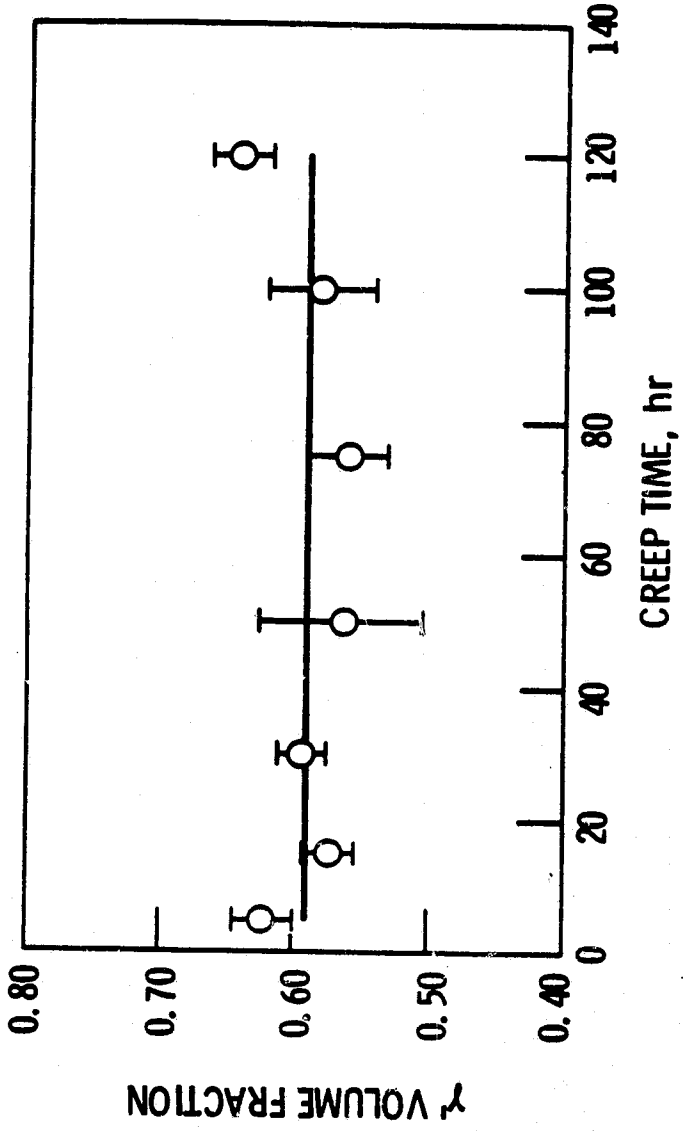

Figure 38. The γ' volume fraction is plotted as a function of time during creep at 982°C and 234 MPa.

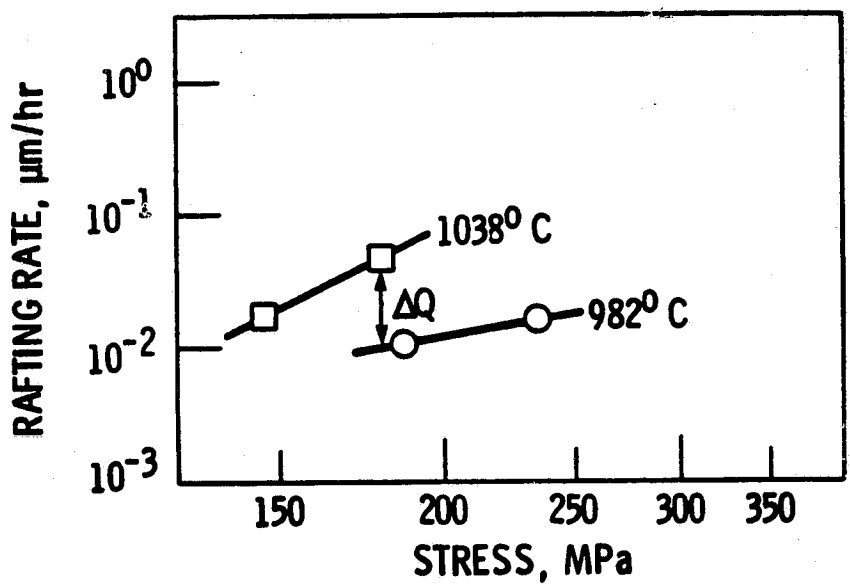

Figure 39. The stress dependence of the rafting rate is illustrated at 982 and 1038°C. The stress at which the apparent activation energy, Q, for rafting was measured is also indicated.

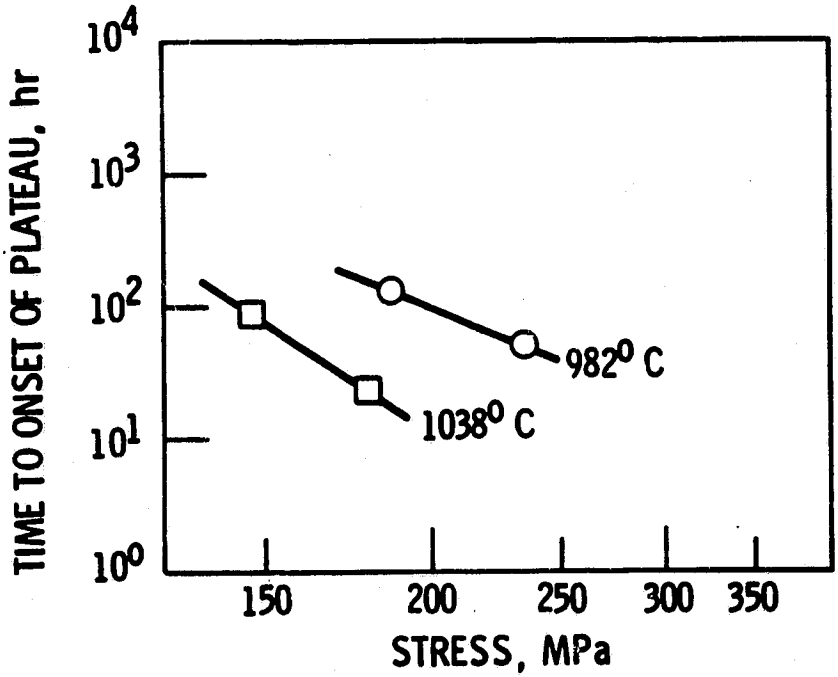

Figure 40. The time to the onset of the plateau in mean raft length is plotted as a function of stress at 982 and 1038°C.

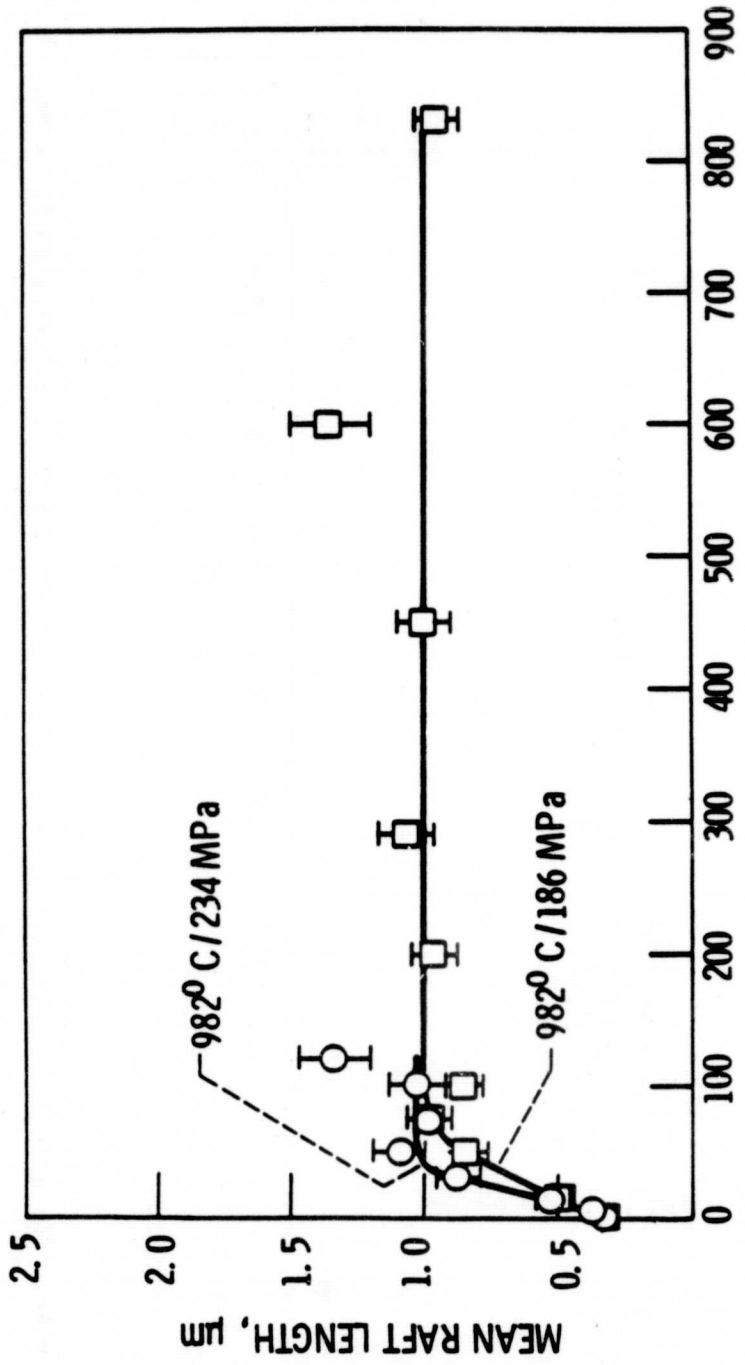

Figure 41. The effect of applied stress on the mean raft length is illustrated for creep at 982°C.

C - 3

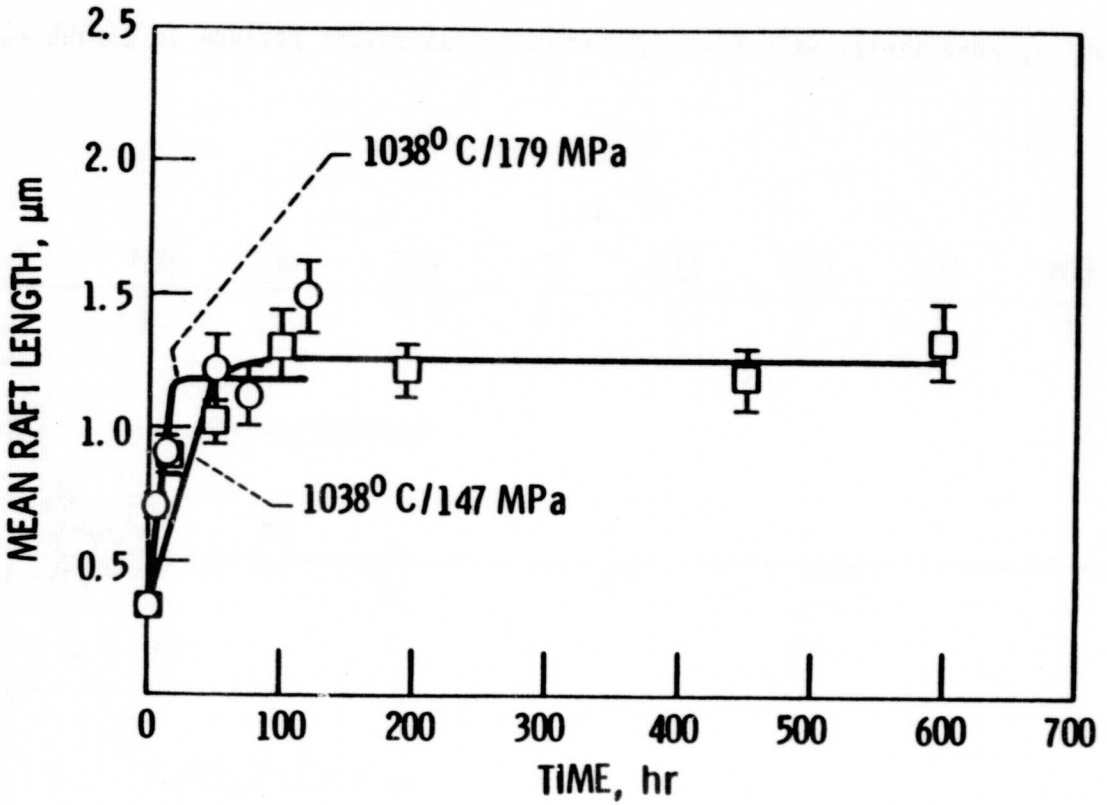

Figure 42. The effect of applied stress on the mean raft length is illustrated for creep at 1038°C.

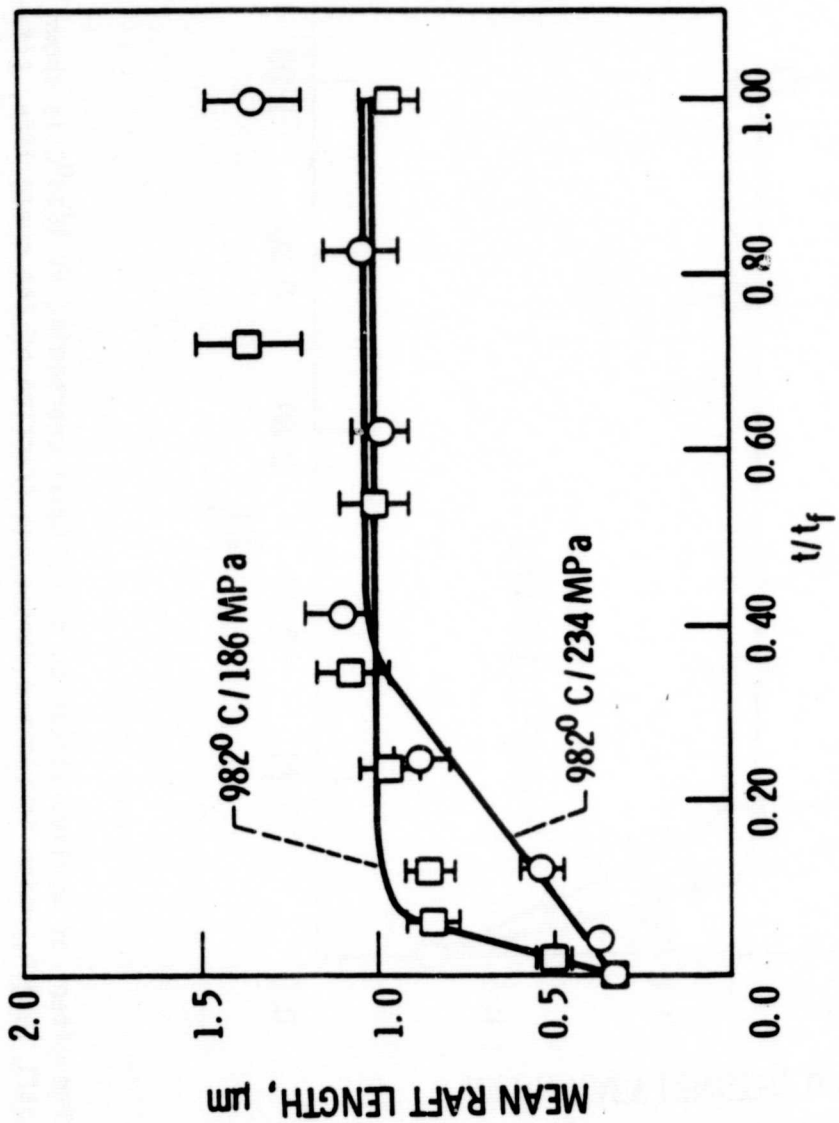

Figure 43. The effect of applied stress on directional coarsening at 982°C is shown for the mean raft length, which is plotted versus the fraction of the creep life, t/t_f.

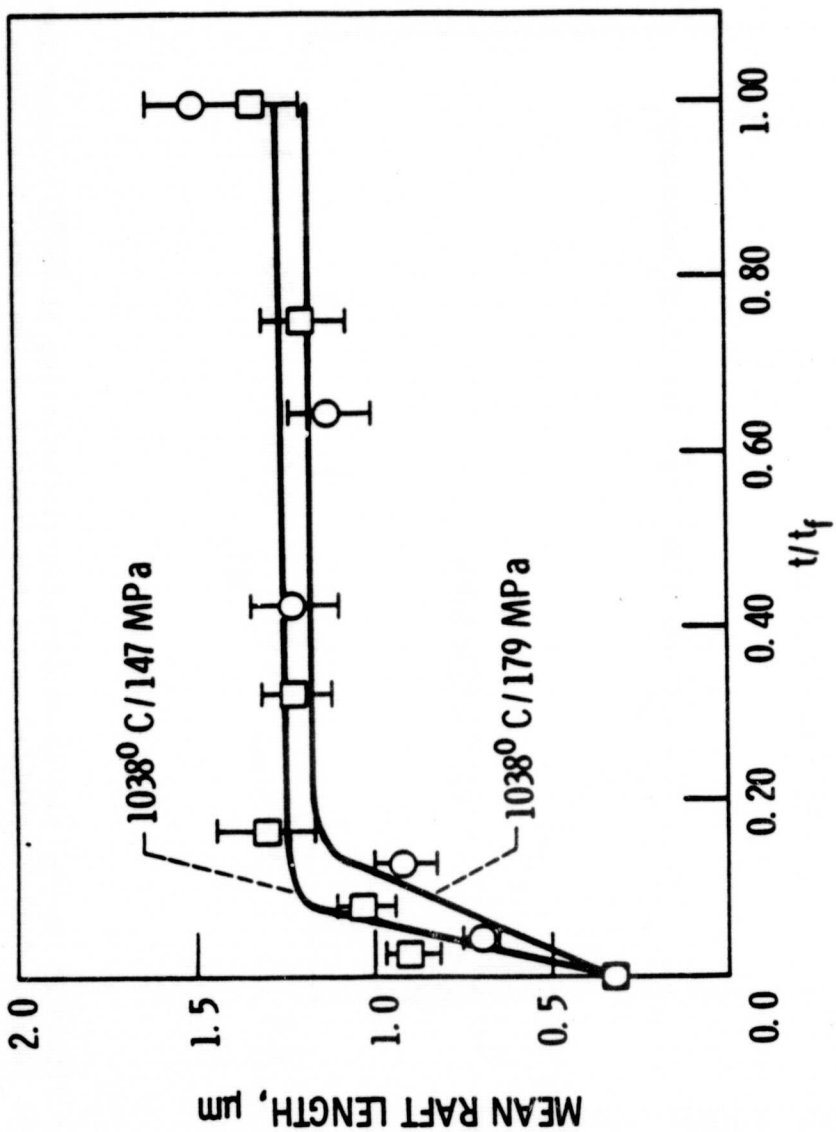

Figure 44. The effect of applied stress on directional coarsening at 1038°C is shown for the mean raft length, which is plotted versus the fraction of the creep life, t/t_f.

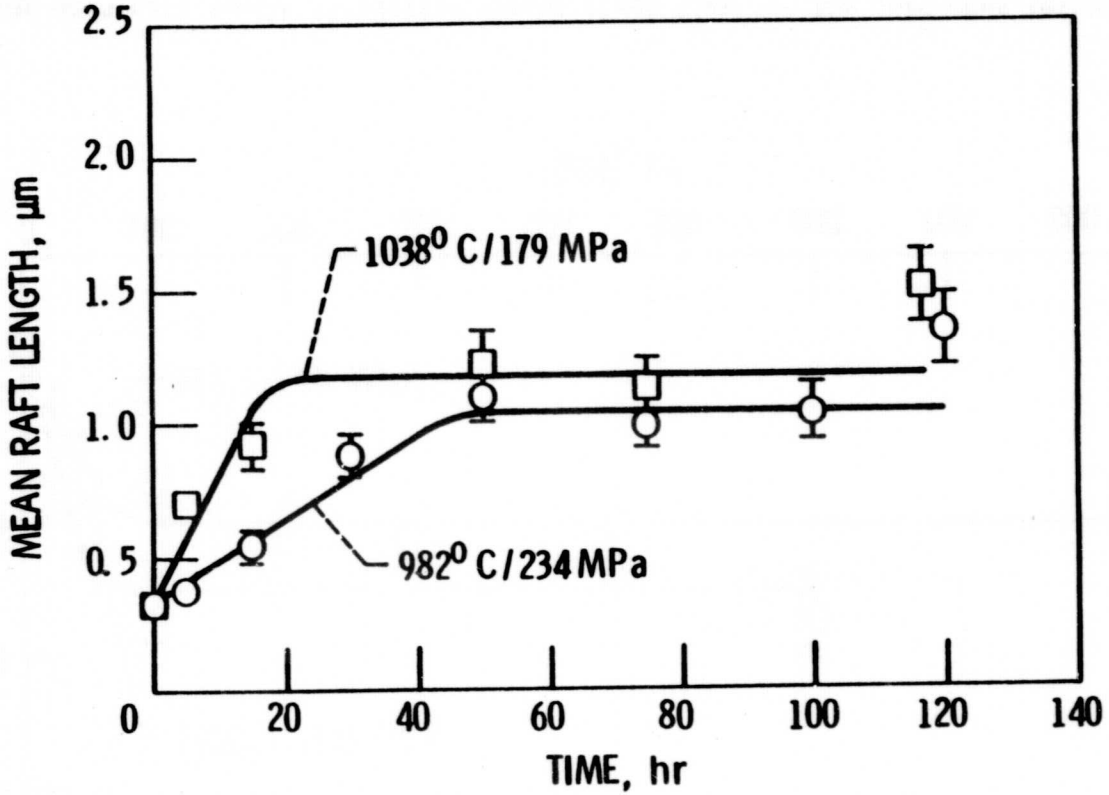

Figure 45. The influence of temperature on the mean raft length is illustrated for creep under two testing conditions which produced equivalent creep lives and steady-state creep rates.

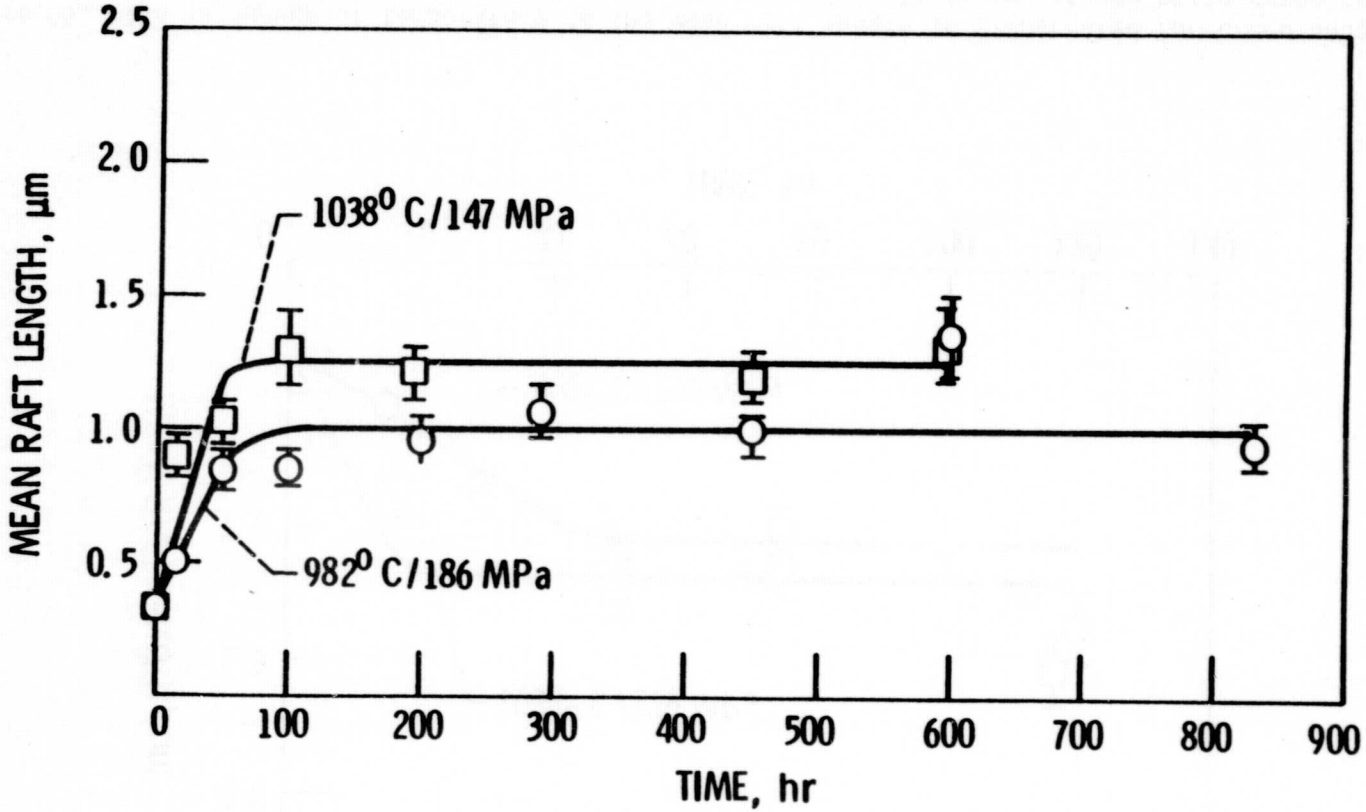

Figure 46. The mean raft length is plotted versus creep time for the specimens tested under the lowest stress levels at 982 and 1038°C.

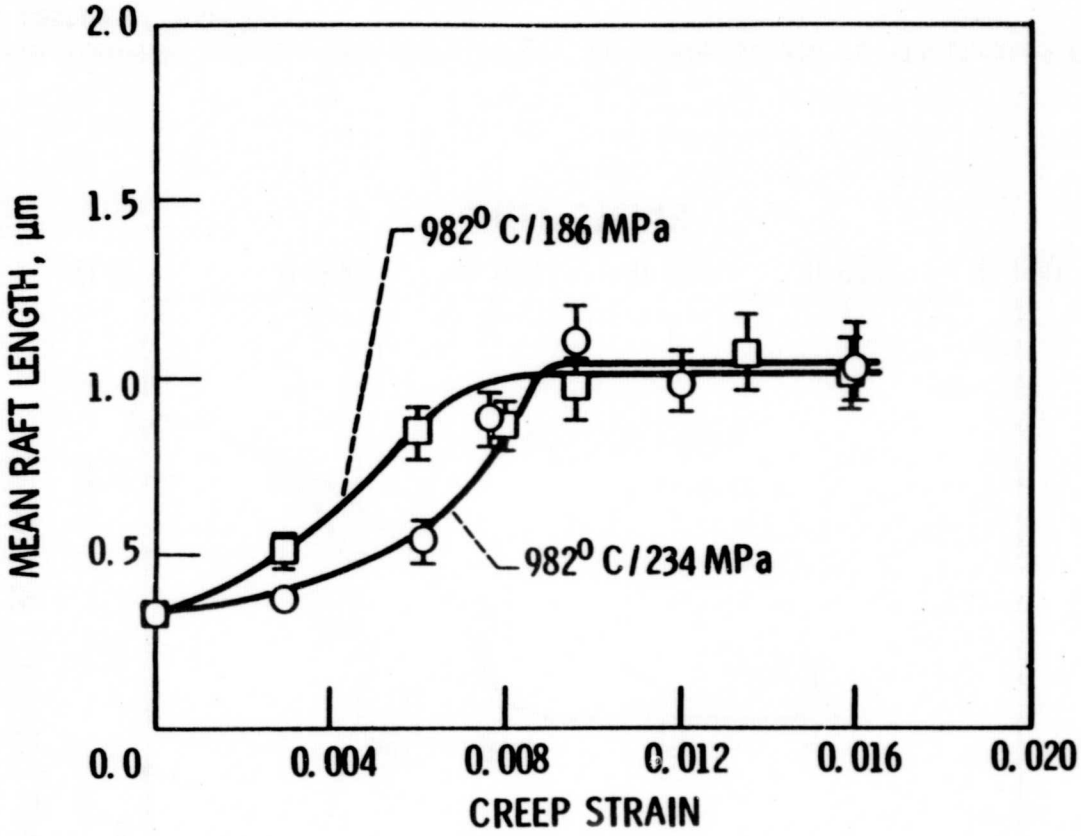

Figure 47. The relationship between mean raft length and creep strain is illustrated for the specimens tested at 982°C.

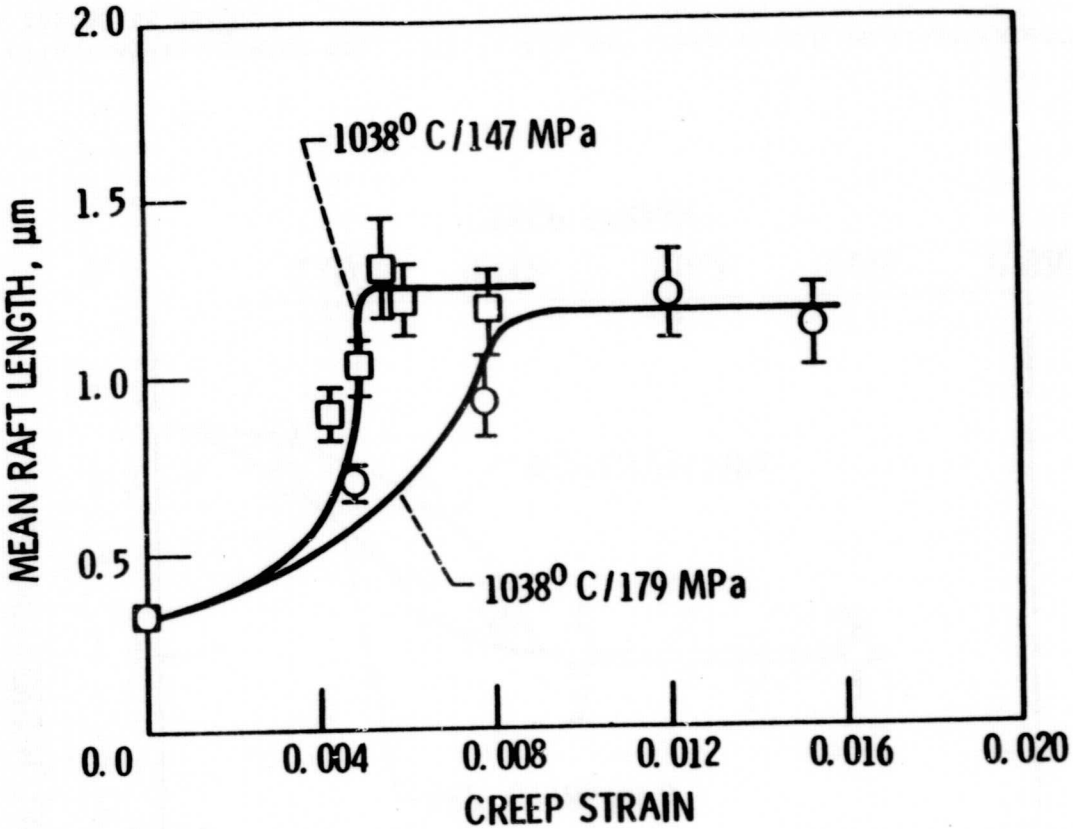

Figure 48. The relationship between mean raft length and creep strain is illustrated for the specimens tested at 1038°C.

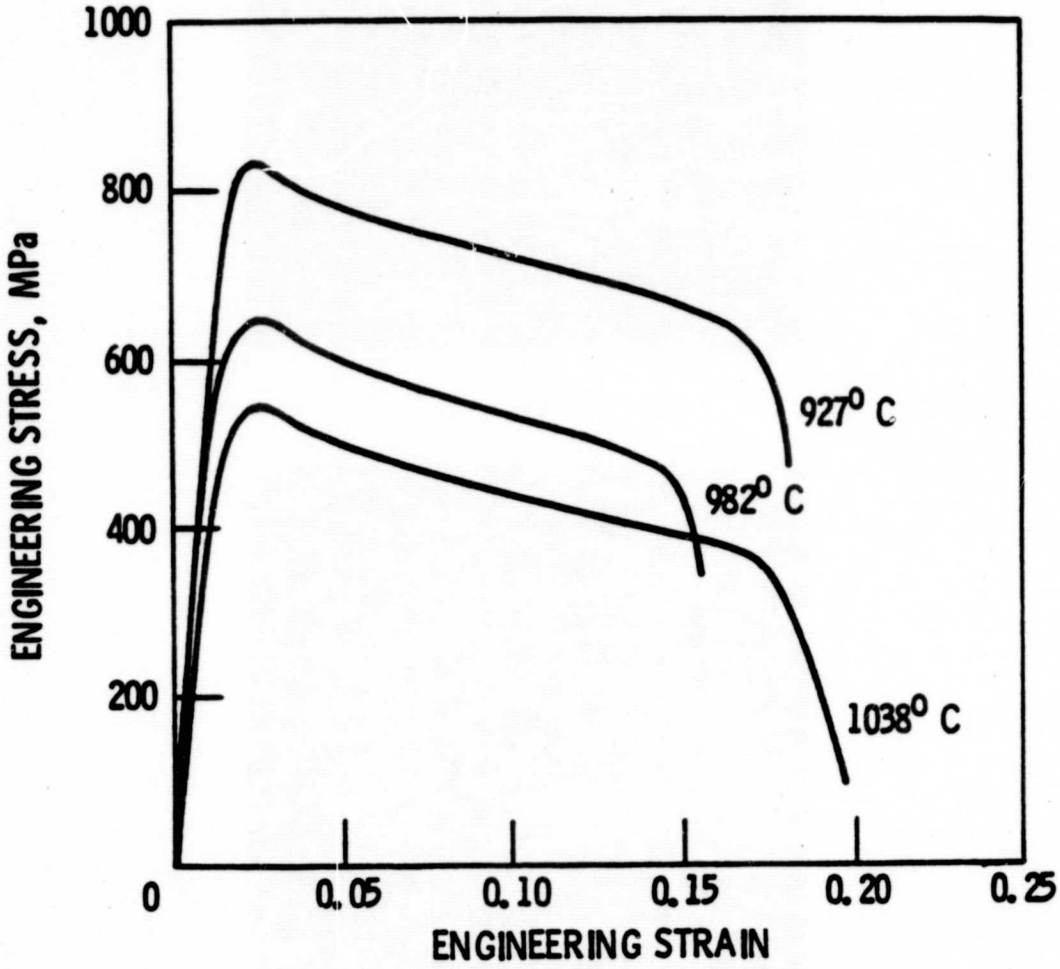

Figure 49. Engineering stress-strain curves for Ni-Al-Mo-Ta single crystals between 927 and 1038°C.

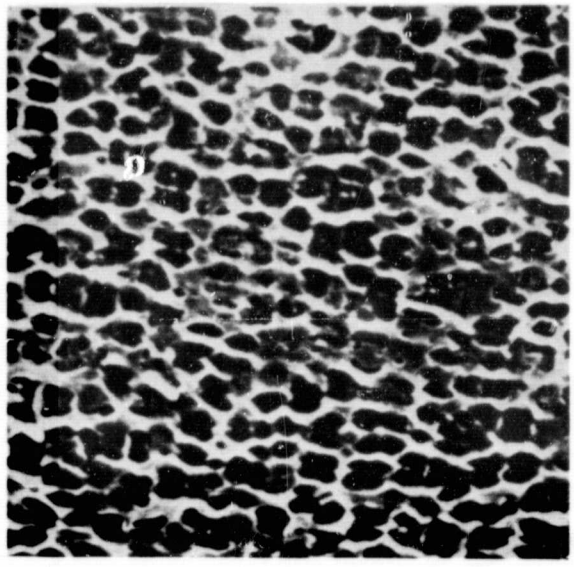

(a)

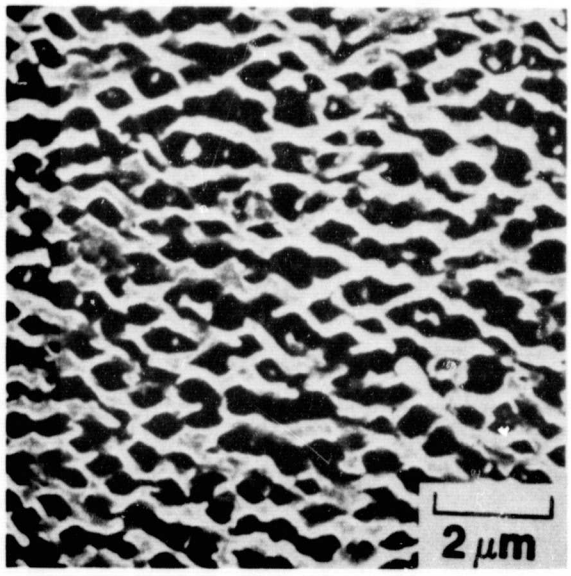

(b)

Figure 50. γ-γ' microstructures in failed specimens after tensile testing at (a) 982 and (b) 1038°C.

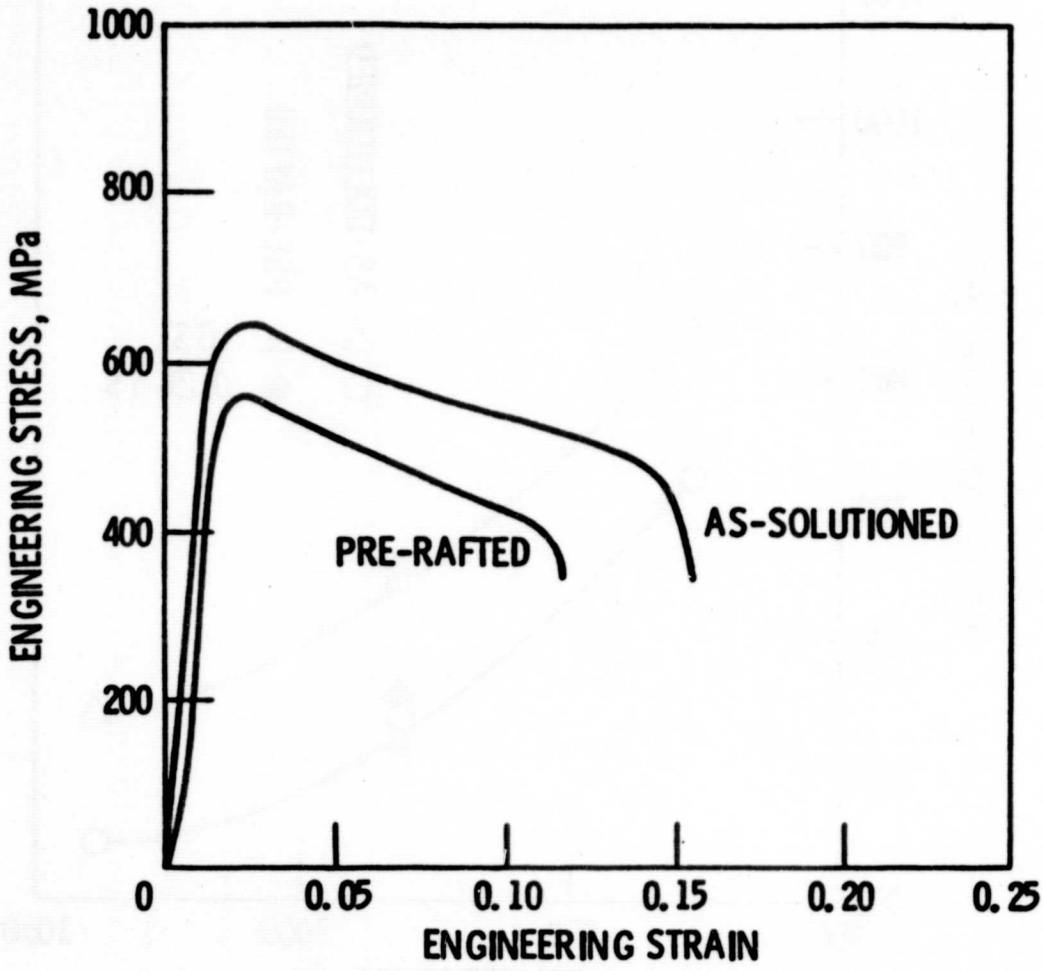

Figure 51. Engineering stress-strain curves of tensile tests at 982°C for specimens in the as-solutioned and pre-rafted conditions.

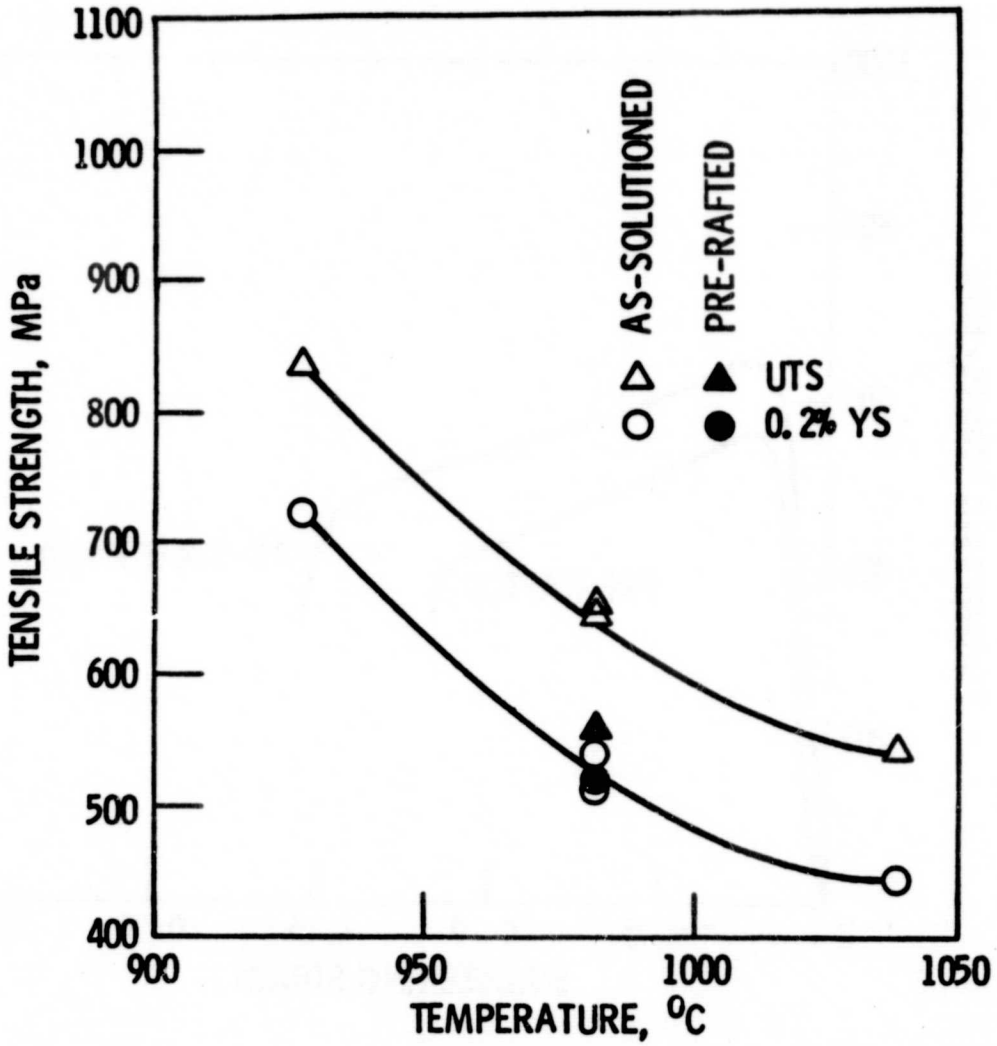

Figure 52. The ultimate tensile strengths and 0.2 pct. yield strengths are illustrated as a function of temperature. Open symbols correspond to specimens in the as-solutioned condition. Closed symbols correspond to the specimen which was pre-rafted prior to tensile testing.

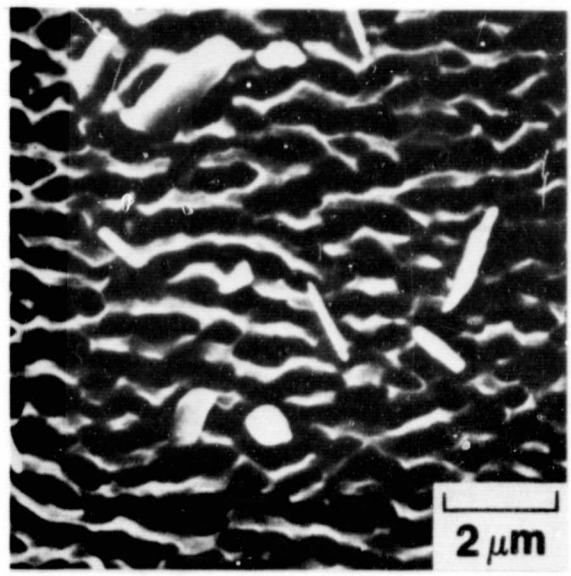

(a)

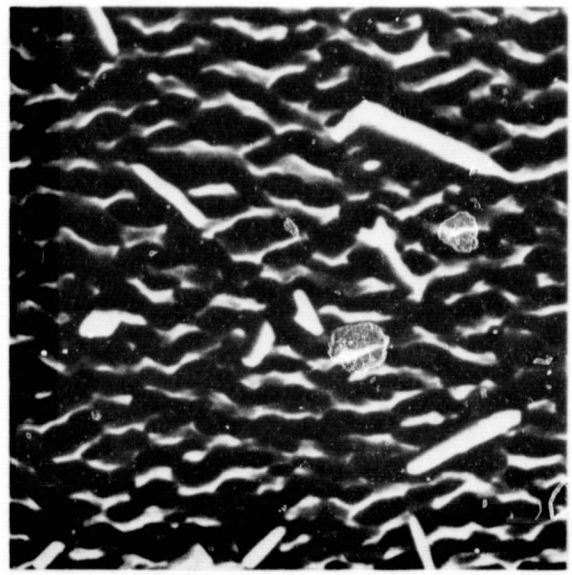

(b)

Figure 53. Directional coarsening is shown in failed specimens after pre-rafting plus tensile testing at 982°C. Micrographs were obtained from (a) the uniform gage section and (b) directly behind the fracture surface.

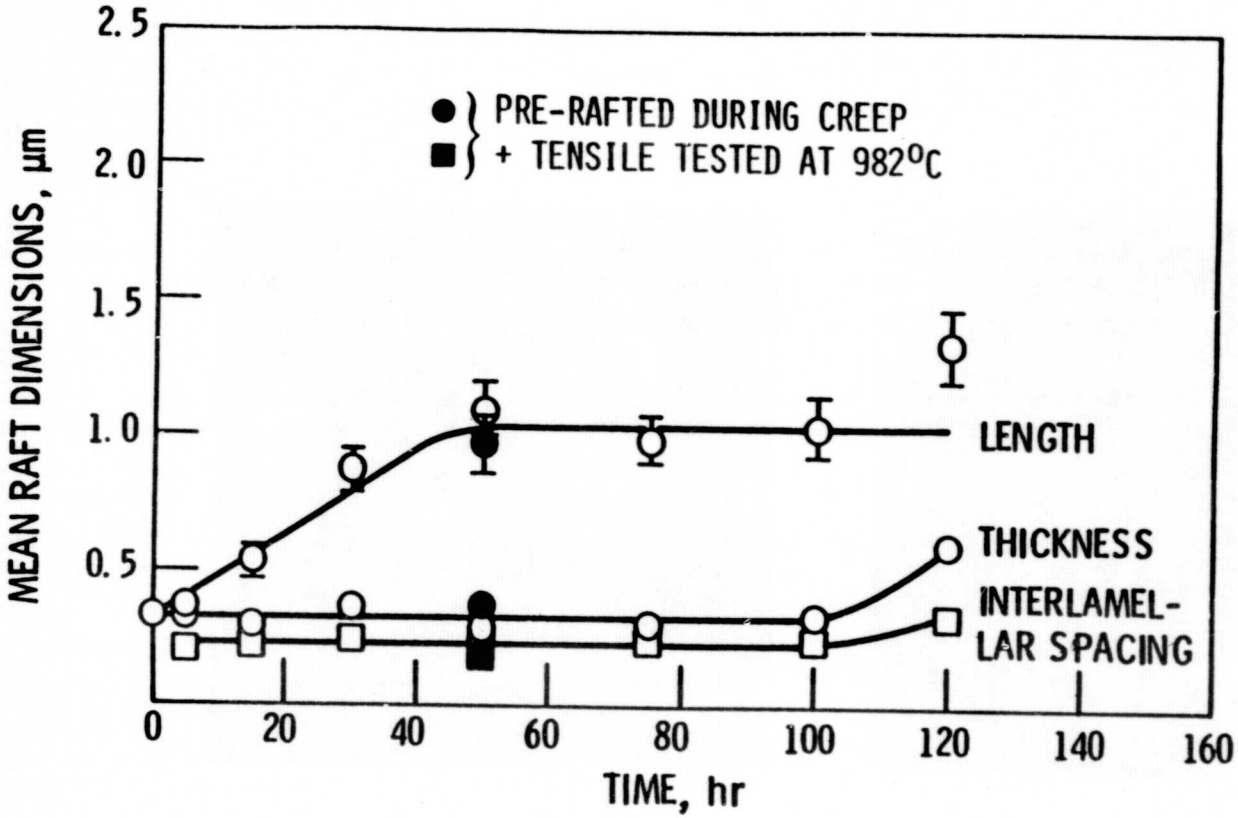

Figure 54. Raft dimensions for the pre-rafted plus tensile tested specimens are indicated by the solid symbols. Pre-rafting was accomplished by creep testing for 50 hours at 982°C and 234 MPa. Superimposed on these data are the raft dimensions for the specimens which were interrupted during creep at 982°C and 234 MPa and shown previously in Figure 34.

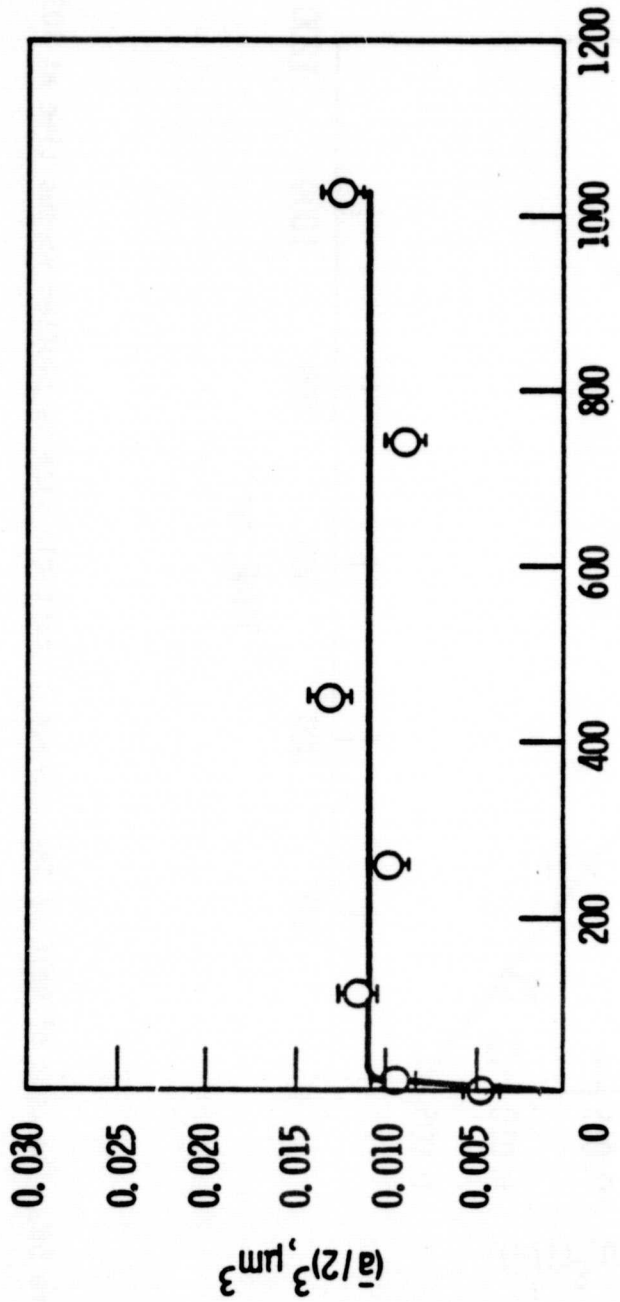

Figure 55. The cube of half of the average γ' particle size is plotted versus time at 982°C.

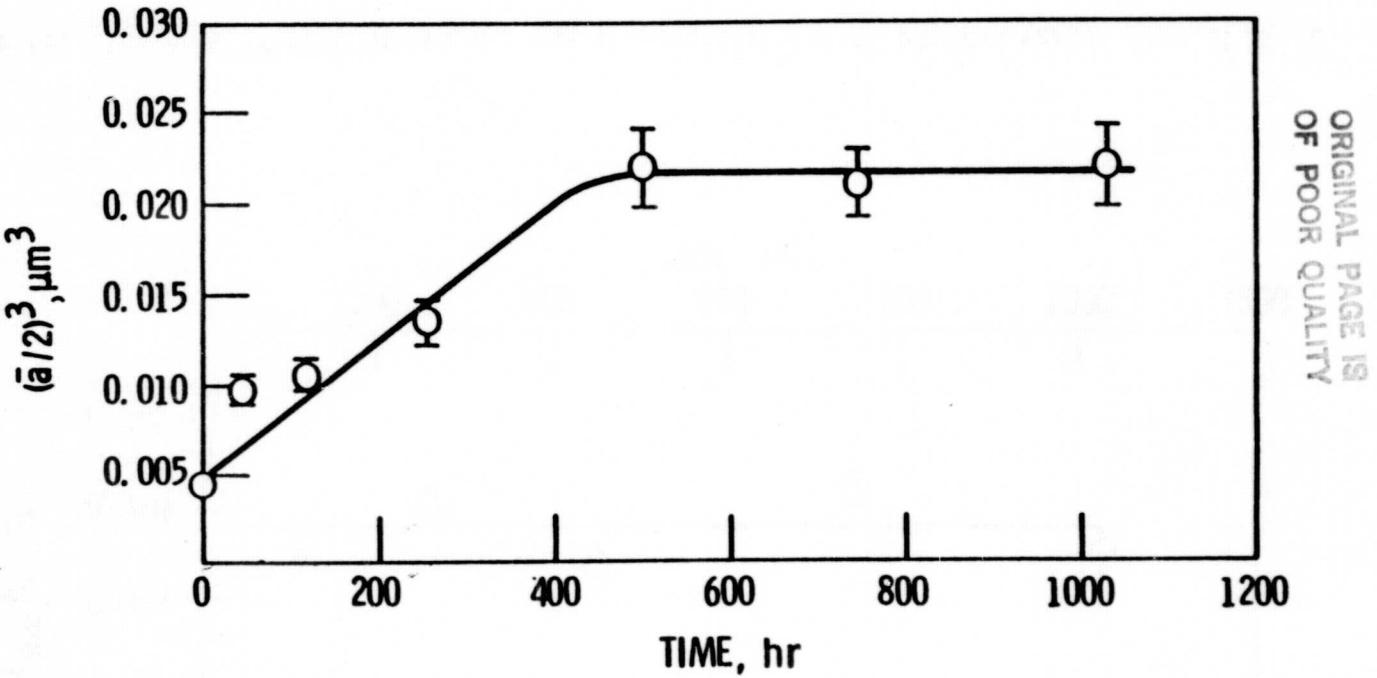

Figure 56. The cube of half of the average γ' particle size is plotted versus time at 1038°C.

Figure 57. TEM micrograph showing the γ' particles and misfit dislocation networks after 114.9 hours of zero-stress aging at $982^{0}C$.

Figure 58. TEM micrograph showing the γ' particles and misfit dislocation networks after 45 hours of zero-stress aging at 1038°C.

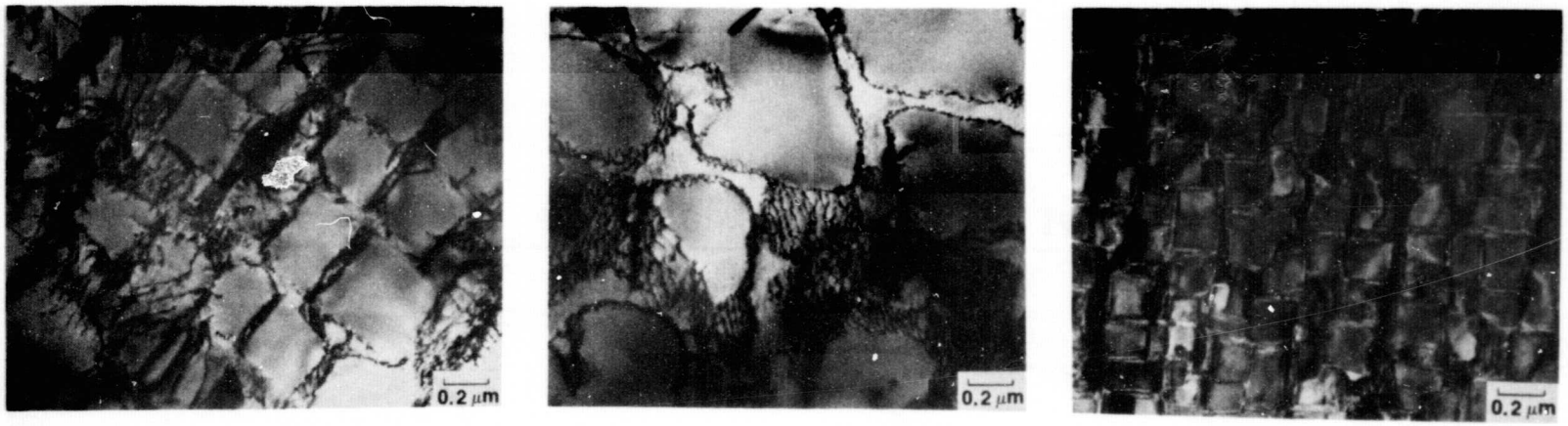

(a) (b) (c)

Figure 59. The γ-γ' microstructures obtained prior to testing by: (a) air quenching from the homogenization temperature; (b) air quenching from the homogenization temperature plus aging at 982°C for 115 hours; and (c) oil quenching from the homogenization temperature.

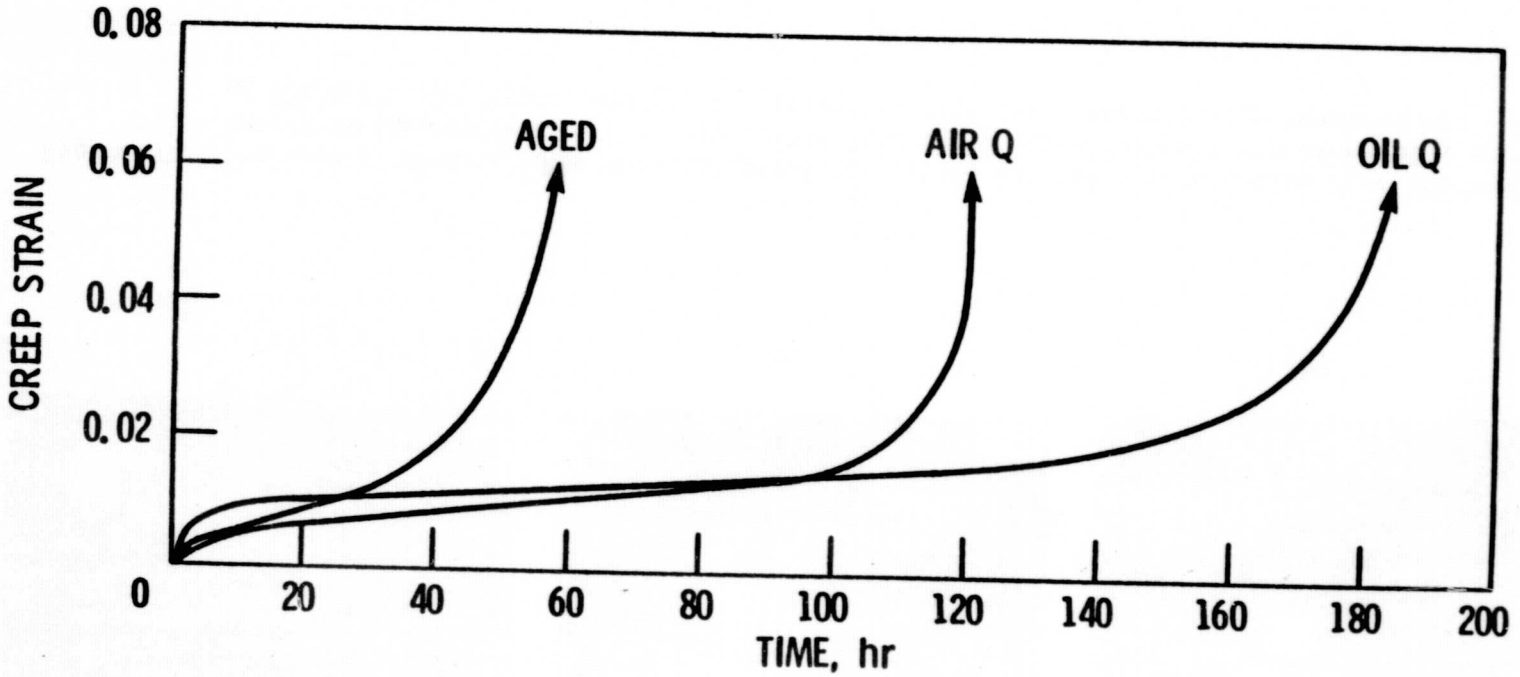

Figure 60. Creep curves at 982°C and 234 MPa are illustrated for single crystals in the aged, air quenched, and oil quenched conditions.

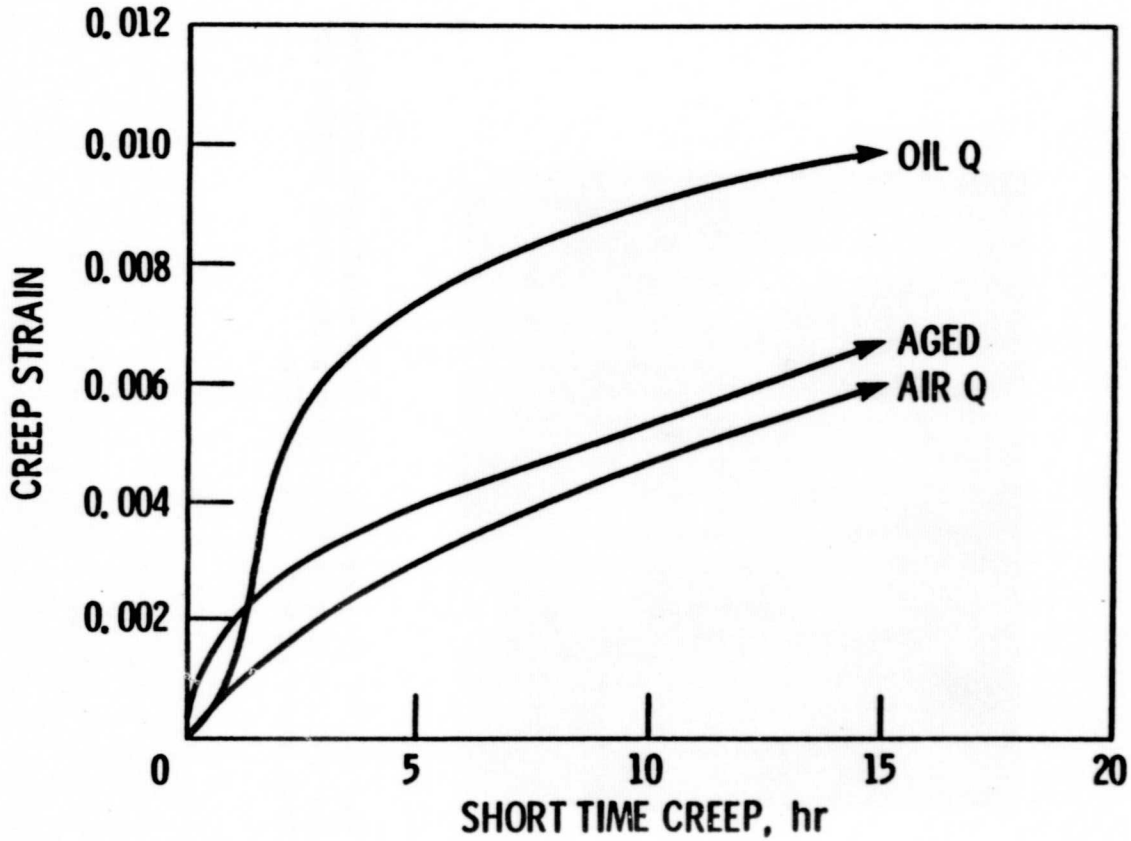

Figure 61. The short time creep curves are illustrated up to the first 15 hours of creep at 982°C and 234 MPa for the aged, air quenched, and oil quenched single crystals.

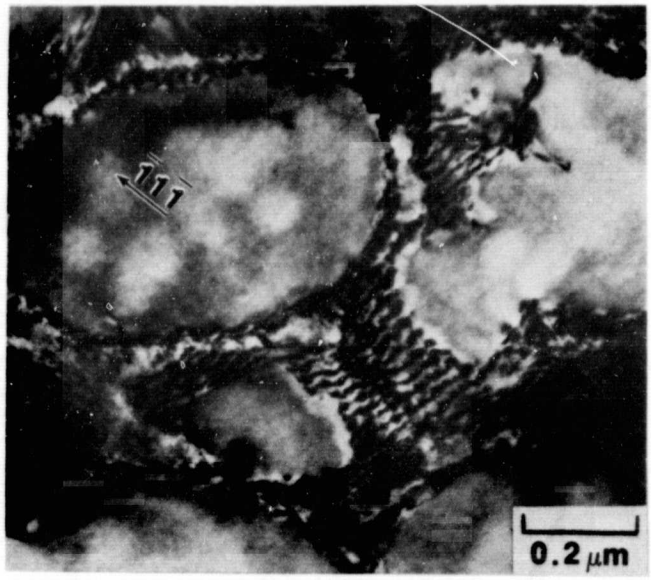

Figure 62. The misfit dislocations and γ' precipitates are shown for the air quenched specimen after creep testing for five hours at 982°C and 234 MPa.

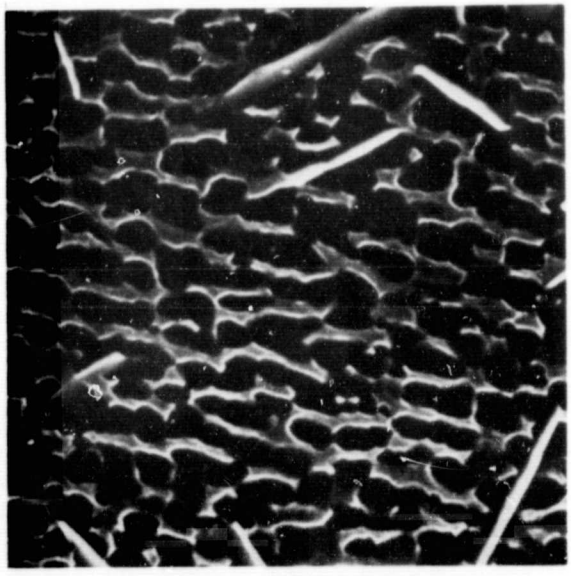

(a)

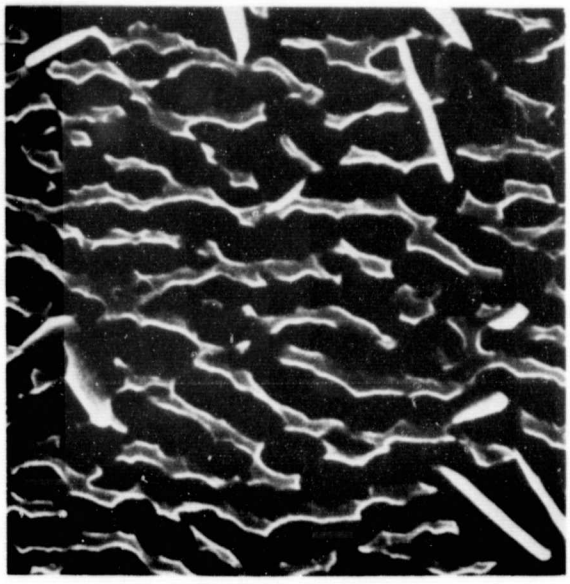

(b)

Figure 63. The development of directional coarsening of γ' is illustrated during creep at 982°C and 234 MPa in pre-aged single crystals at: (a) 15, (b) 50, and (c) 63.9 hours, in the failed condition. The stress axis is vertical in all photos.

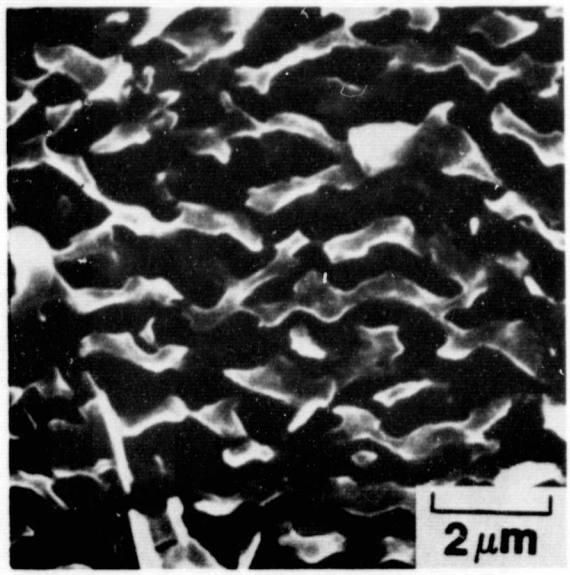

(c)

Figure 63 concluded

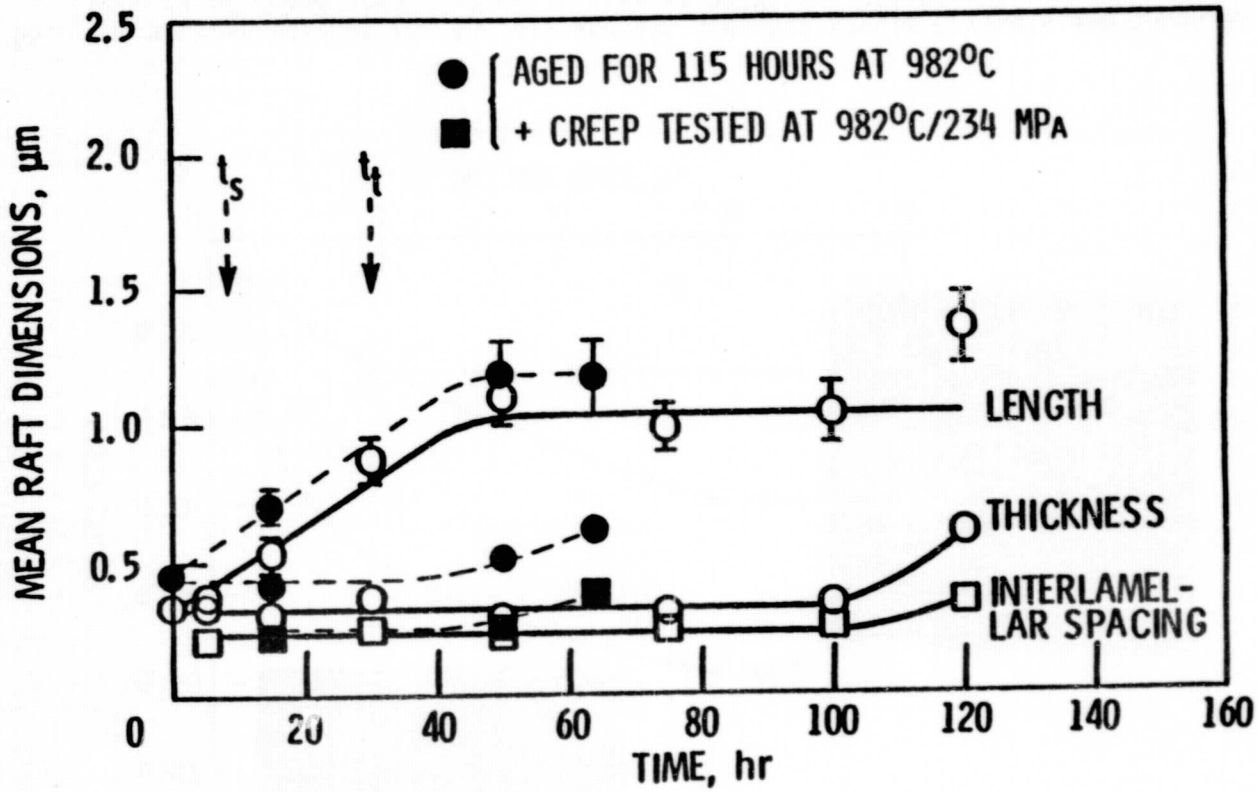

Figure 64. The mean raft dimensions are plotted as a function of time during creep at 982°C and 234 MPa for the aged single crystals. The open symbols represent the raft dimensions for the air quenched specimens, shown previously in Figure 34. The times to the onset of steady-state creep, t_s, and to the onset of tertiary creep, t_t, are illustrated for the aged specimens.

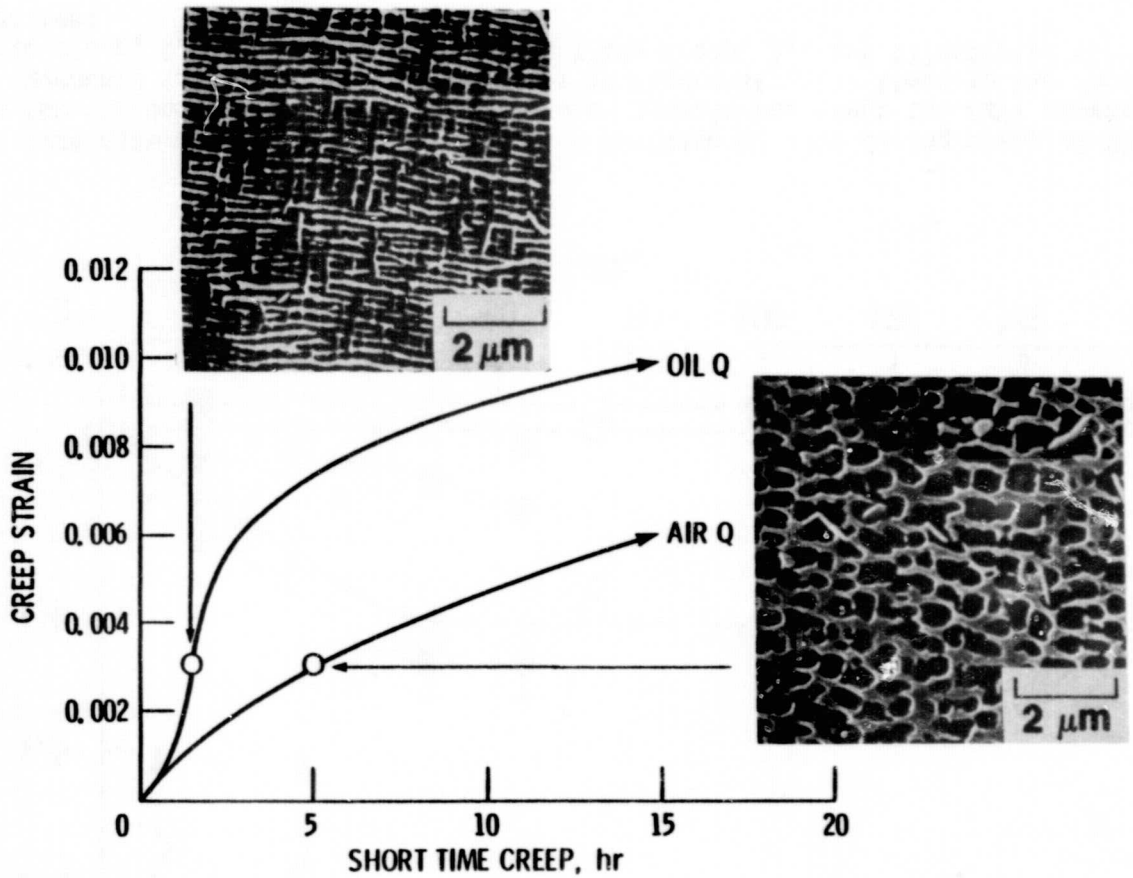

Figure 65. The microstructures for the oil and air quenched single crystals are shown at equal amounts of creep strain after testing at 982°C and 234 MPa.

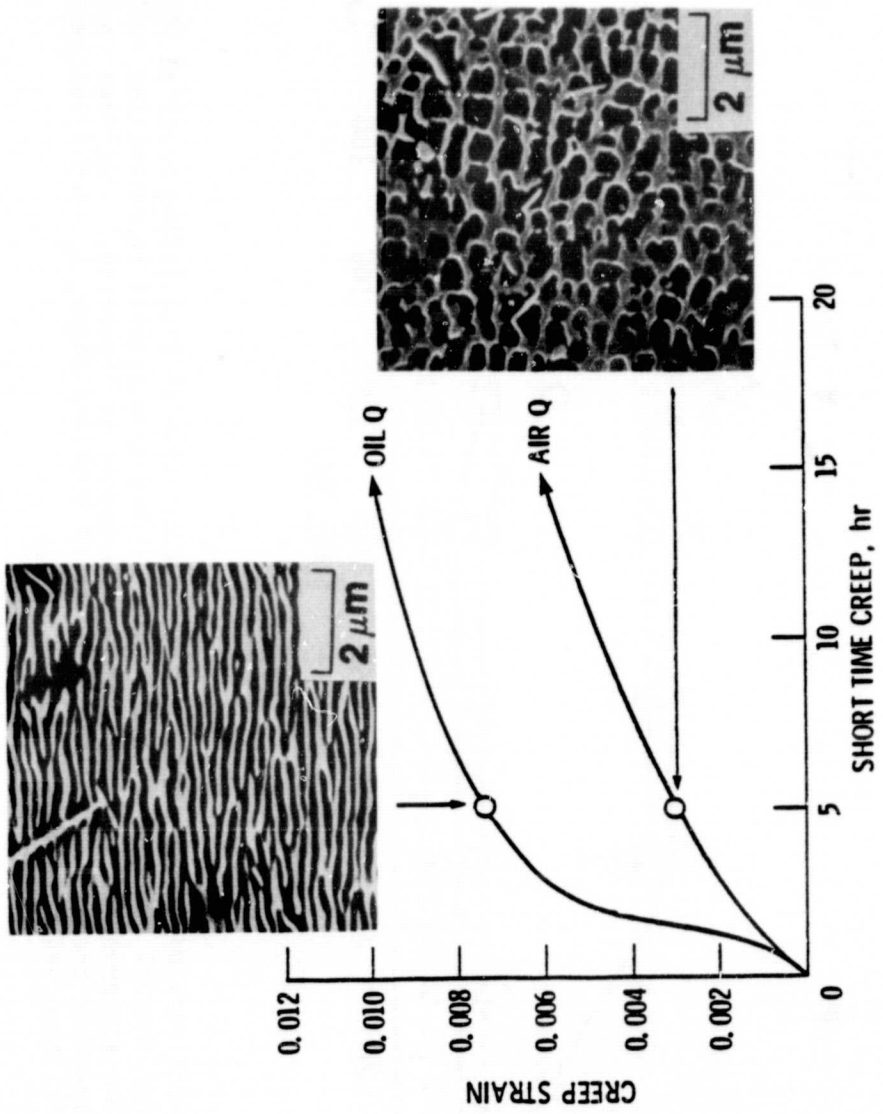

Figure 66. The microstructures for the oil and air quenched single crystals are shown after five hours of testing at 982°C and 234 MPa.

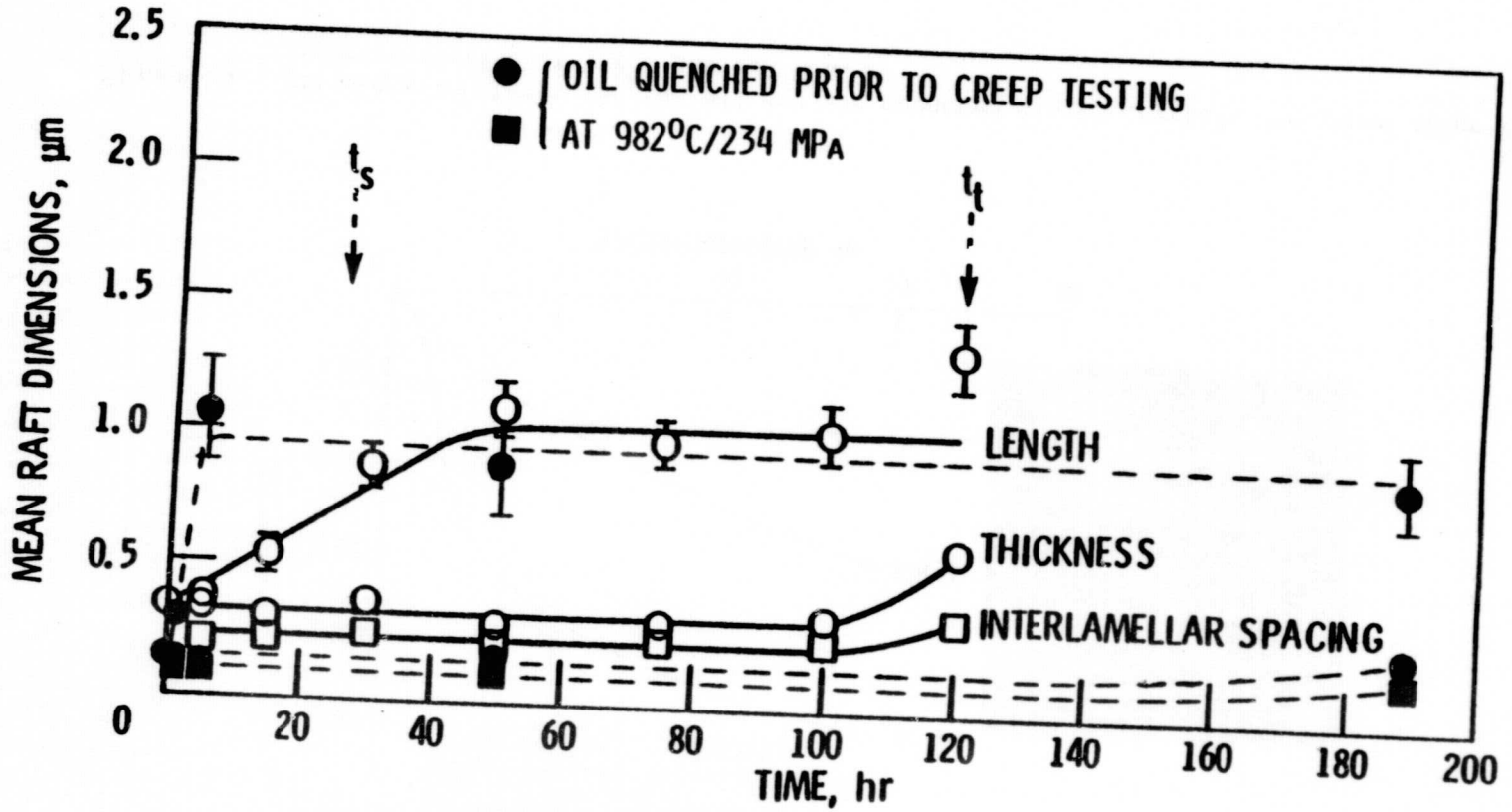

Figure 67. The mean raft dimensions are plotted as a function of time during creep at 982°C and 234 MPa for the oil quenched single crystals. The open symbols represent the raft dimensions for the air quenched specimens, shown previously in Figure 34. The times to the onset of steady-state creep, t_s, and to the onset of tertiary creep, t_t, are illustrated for the oil quenched specimens.

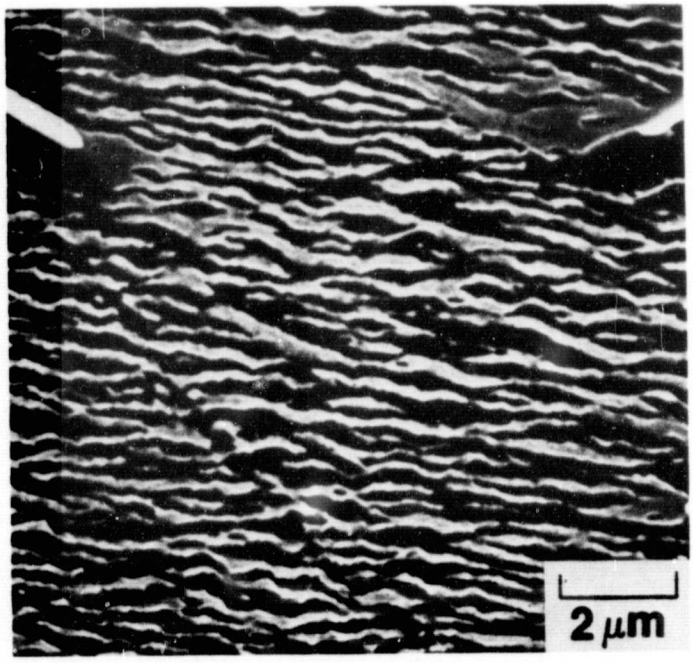

Figure 68. Finely-spaced γ-γ' lamellae are illustrated in an oil quenched specimen after 263 hours of creep testing at 1038°C and 147 MPa.

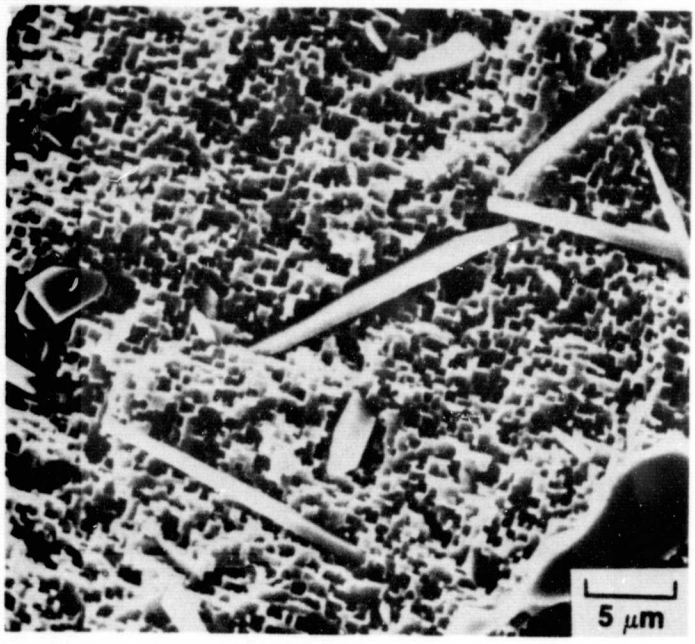

Figure 69. SEM micrograph showing the surface of a specimen which remained after deep etching.

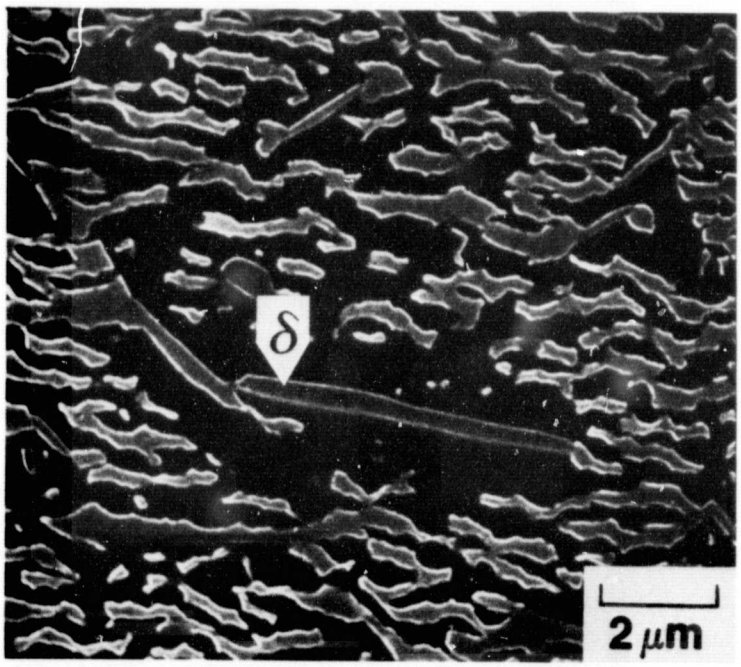

Figure 70. SEM micrograph showing the δ phase with a surrounding envelope of γ' in a failed specimen after testing at 982°C and 186 MPa.

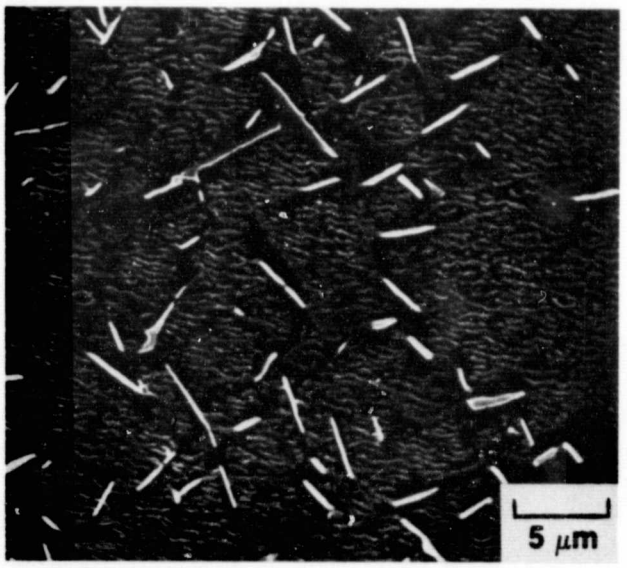

(a)

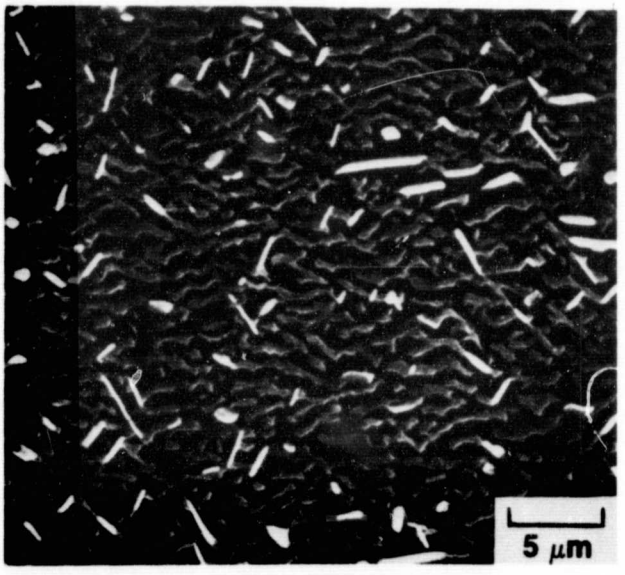

(b)

Figure 71. Discontinuities in the γ-γ' lamellar structure which were caused by δ needles with surrounding γ' envelopes in failed specimens after testing at 982°C and 234 MPa. (a) oil quenched and (b) air quenched single crystals.

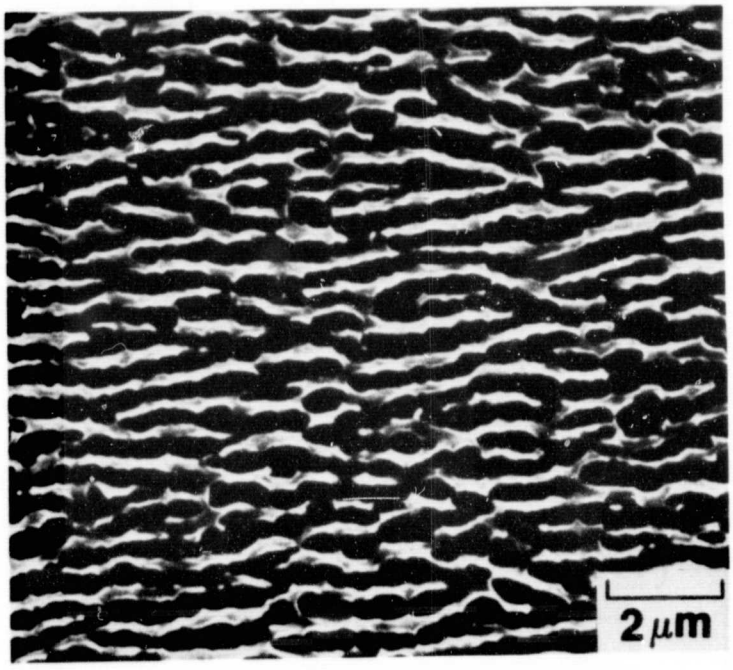

Figure 72. Perfection of the γ-γ' lamellae observed in an area which did not contain δ phase after 50 hours of testing at 1038°C and 147 MPa.

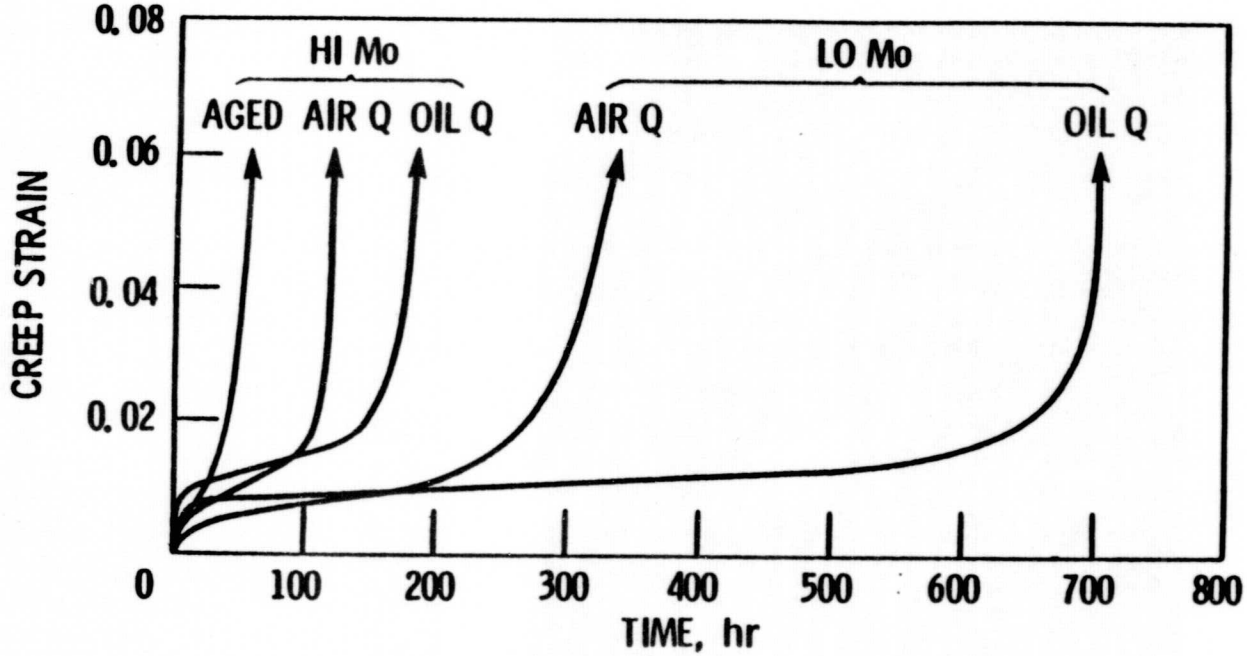

Figure 73. Creep curves at 982°C and 234 MPa are illustrated for the 14.6 and 13.9 wt. pct. Mo alloys in the aged, air quenched, and oil quenched conditions.

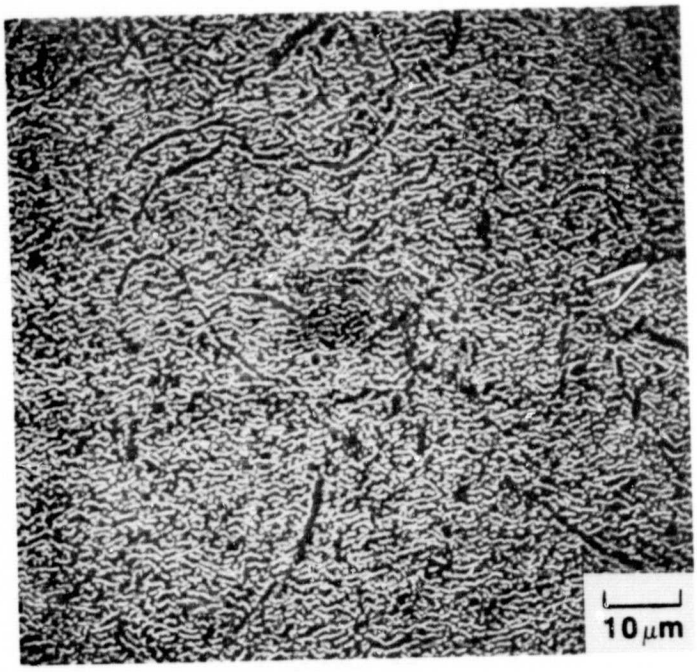

Figure 74. SEM micrograph containing the highest volume fraction of δ phase observed in the 13.9 wt. pct. Mo alloy after creep testing for 356 hours at 982°C and 234 MPa.

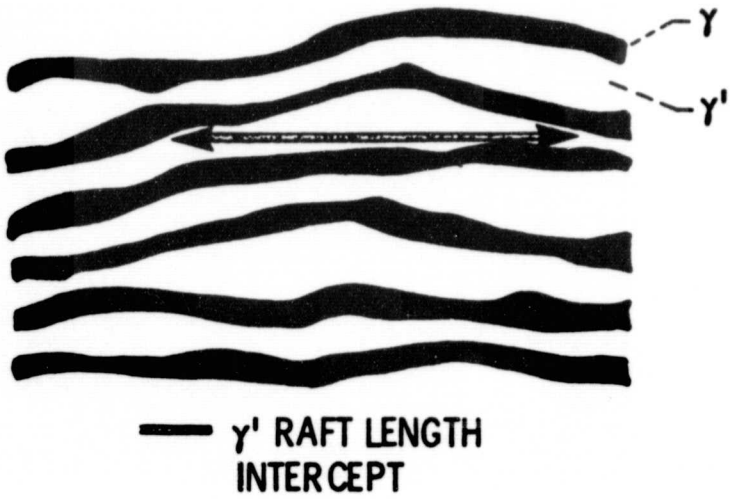

Figure 75. A limitation of the line intercept technique is illustrated schematically for the γ' raft length measurement within the plateau region.

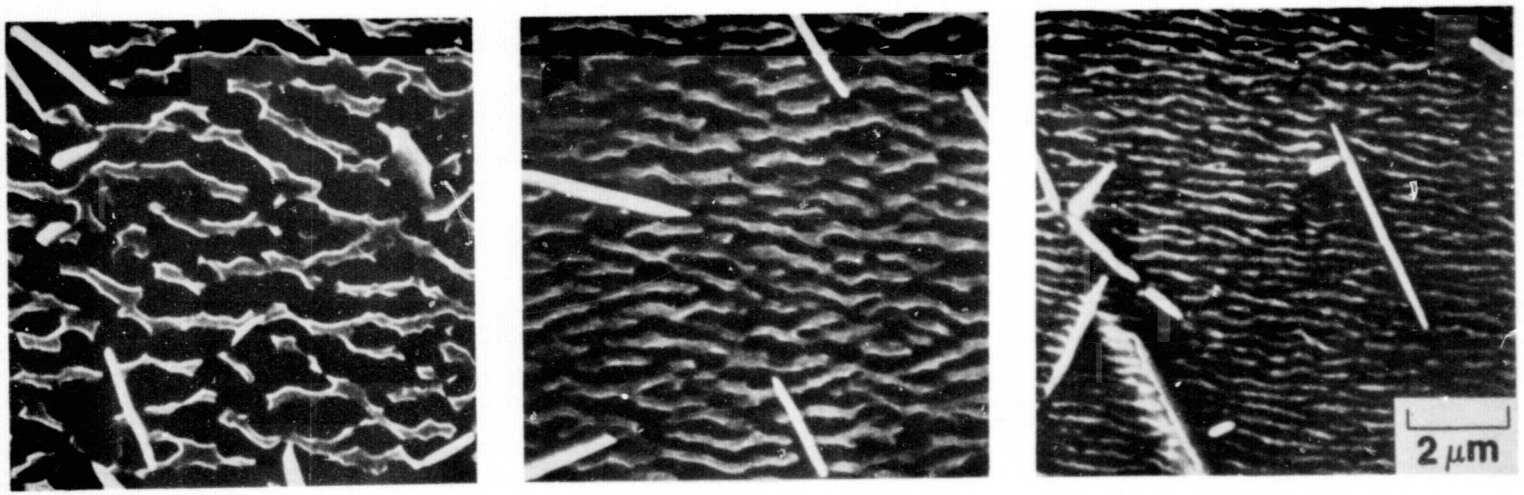

(a) (b) (c)

Figure 76. The γ-γ' lamellae are shown after 50 hours of creep testing at 982°C and 234 MPa in the (a) aged, (b) air quenched, and (c) oil quenched conditions.